Imperial College London

Department of Chemical Engineering

A thesis submitted for the degree of

Doctor of Philosophy

Convective Dissolution in Porous Media: Three-Dimensional Imaging Experiments and Numerical Simulations

---

Author:

Rebecca Liyanage

Supervisors:

Ronny Pini

John Crawshaw

Sam Krevor

December 26, 2018

I hearby declare, that this thesis is a result of my own work, other than where it has been appropriately referenced. Some of the work presented in Chapter 1, 2 and 3 has been submitted for publication

Abstract

Convective dissolution is a phenomenon induced by a buoyant instability between two fluids resulting in characteristic finger-like mixing patterns. One important example is a key trapping mechanism during CO_2 sequestration in deep saline aquifers. The Rayleigh number, Ra, which is a measure of convective vigour and the Sherwood number, Sh, which indicates the strength of mass transport are used to parameterise this process. We present a novel methodology to image convective dissolution using X-ray CT in a three-dimensional porous medium formed of glass beads with a model fluid pair MEG/water and BEG/water. 3D reconstructions allow us to visualise the spatial and temporal evolution of the plume from onset to the shutdown of convection while quantifying the macroscopic quantities such as the rate of dissolution and horizontal concentration profiles. We investigate convective dissolution with and without permeability heterogeneity over the Rayleigh range, $Ra = 2000 - 5000$, in a spherical, cuboidal and cylindrical geometry. Simple heterogeneity patterns such as single inclined layers and a series of discontinuous layers were included. It was concluded that the spatial configuration of the less permeable layers was the most important factor in either enhancing (due to flow focusing) or impeding (due to compartmentalisation of the plume) the rate of dissolution compared to the homogeneous case. However, linear trends in the Sherwood and Rayleigh numbers were consistency reported in both the homogeneous $Sh = 0.025Ra$ and heterogeneous studies $Sh = 0.0236Ra$. 2D COMSOL numerical simulations were performed to extend the Ra range explored by the experiments and allow an investigation of permeability heterogeneity configurations not possible in the laboratory. The results confirmed the experimental findings with very similar scaling observed $Sh = 0.022Ra$. The results also shed light on the plume structures responsible for flow focusing. Finally, we present suggestions for future work in CO_2-brine-rock systems.

List of Publications

R.Liyanage, J. Cen, J. Crawshaw, S. Krevor and R. Pini, "Multidimensional observations of dissolution-driven convection in simple porous media using X-ray CT scanning" in Transport in Porous Med (2018). https://doi.org/10.1007/s11242-018-1158-3

R.Liyanage, J. Crawshaw, S. Krevor and R. Pini, "Multi-dimensional Imaging of Convective Mixing in a Porous Media," in Energy Procedia, vol. 114, pp. 4981–4985, 2017. doi.org/10.1016/j.egypro.2017.03.1641

Acknowledgements

I would like to thank my supervisors Ronny Pini, John Crawshaw and Sam Krevor for their continued support over the years. Also, my former supervisor Edo Boek for initially taking me on as a PhD student and Klaus Hellgardt my academic mentor. A special thanks also to Saurabh Shah for conducting the micro CT imaging, Andrew Russell for the rheology measurements and Jiajun Cen for the supporting simulation work.

I gratefully thank and acknowledge the Department of Chemical Engineering, Imperial College London, for awarding me a departmental scholarship provided by EPSRC. Experiments were performed in the Qatar Carbonates and Carbon Storage Research Centre at Imperial College London, funded jointly by Shell, Qatar Petroleum, and the Qatar Science and Technology Park.

On a personal note, there is a long list of people without whose support this PhD would not have been possible. I would like to thank everyone who has supported me with their insights, discussions, friendship or love.

Contents

List of Figures

List of Tables

Chapter 1

Introduction

The study of convective dissolution in porous media continues to find applications in both traditional and emerging engineering problems, many of which occur in nature [1, 2]. We focus here on density-driven free convection, a mixing process which is induced and sustained by a buoyancy effect, in the absence of advective flow. In particular this research is aimed to answer questions related to subsurfurce flow and in specifically carbon storage. However, this work could be adapted to other applications such as industrial mixing or near surface saline water intrusion.

1.1 Rayleigh - Taylor Instability

The underpinning principle behind the process of convective dissolution is a Rayleigh-Taylor Instability. In the case where there is a heavier fluid atop a lighter fluid, instability in the interface will develop due to buoyancy effects of the migrating lighter fluid upwards as illustrated in Figure 1.1. The wavelength of the instability will grow exponentially over time and develop into characteristic finger projections, and thus convection will be initiated [3].

The Rayleigh number, Ra, is commonly used to parametrise the process resulting from a Rayleigh-Taylor instability and indicates the vigour of convection. It is a ratio of the buoyancy forces compared to the diffusive forces and in a porous medium is expressed as

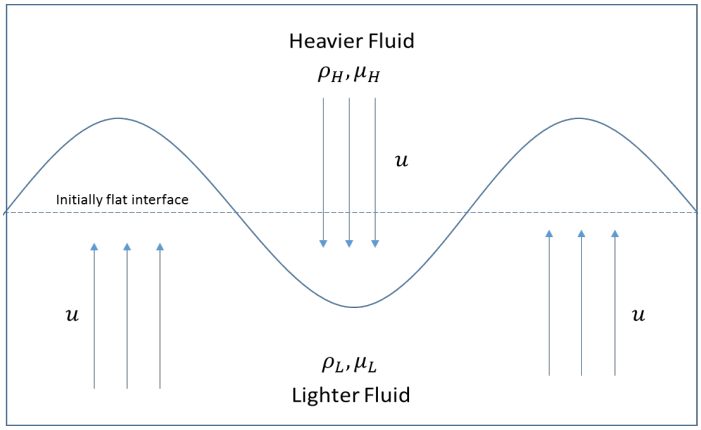

Figure 1.1: A sketch of the fluid-fluid interface between a heavier fluid and a lighter fluid where a Rayleigh-Taylor instability forms as the lighter fluid pushes up due to buoyancy and the heavier fluid moves downwards. The initially flat interface is also indicated with a dashed line.

shown in Equation 1.1

$$Ra = \frac{k\Delta\rho_{\max} H g}{\mu_2 \phi \mathscr{D}} \tag{1.1}$$

where k is the permeability of the porous media, $\Delta\rho_{max}$ is the maximum density difference between the fluids, H is the characteristic length which is usually defined as the height of the domain, g is the acceleration due to gravity, μ_2 is the viscosity of the lighter fluid, $\mathscr{D}$ is the average diffusion coefficient in the bulk solution, and ϕ is the porosity.

Depending on Ra the process will tend either to the diffusive regime at low Ra or the convective regime at high Ra. The transition between pure diffusion and convection is debatable; in the classical, analogous heat problem the critical Rayleigh number (Ra_c, below which convection will not take place) is $Ra_c = 4\pi^2$ [4, 5, 6, 7]. However, for the solute case it has been suggested there is no analytical solution and instead approximations have been made such as $Ra_c \approx 31.5$ [8] or that when $Ra_c < 55$ [9] convection does not occur. Although there are many similarities between convective driven by heat and density, solute mixing is intrinsically a transient problem.

1.2 Flow and Mixing in a Porous Medium

When dealing with a porous medium, the flow can be described by the Darcy's law as shown in Equation 1.2

$$u = -\frac{k}{\mu}(\nabla p - \rho g) \tag{1.2}$$

Darcy's law allows the calculation of the Darcy velocity, u via a comparison of the driving forces to the viscous drag. Here ∇p is the pressure gradient, ρ is the local fluid density and, g is the gravitational acceleration, μ is the viscosity and k is the permeability. Of course in a real system, the connectedness of the pore structure and size distribution are key factors that influence the permeability.

Equation 1.2 is predicated on the definition of the interstitial velocity, v, being the mean velocity of the entire pore space in a given representative volume consisting of many pores. Thus, as the Darcy velocity encapsulates the velocity over both the pore and grain, it can be written in terms of the mean velocity where $u = \phi v$ and ϕ is the porosity of the porous medium. It also assumes the porous media is completely saturated and the length scales of the flow are much larger than the representative volume chosen, otherwise this calculation will not be representative of the whole. Further details of the transport equations used to describe this process can be found in Chapter 7.

1.3 Applications in Subsurface Flow

One particular application that has increased the interest in this phenomenon is geologic carbon sequestration (GCS) [10] because of its potential impact on the dissolution rate of CO_2 into formation fluids. There are four main trapping mechanisms in CO_2 storage which have been set out in Figure 1.2 [11]; (1) structural trapping is where an impermeable 'cap-rock' is a physical barrier preventing the carbon dioxide from rising upwards, (2) capillary trapping as a result of the disconnection of the free CO_2 phase in the pore space, (3) mineral trapping is the long term trapping of CO_2 as precipitate and the finally, (4) focus of this work, solubility trapping.

In this scenario, the buoyancy effect may be due to the naturally occurring geothermal gradient in the reservoir, but also -and primarily- to varying composition of the aqueous

phases [12]. In fact, CO_2 dissolution into brine leads to a local density increase on the order of 0.1 to 1% (depending on pressure and temperature [13]), which is sufficient to create a buoyant instability that in turns induces a convective overturn in the brine; the denser CO_2-rich aqueous mixture flows downwards and pushes fresh brine up towards the CO_2-brine interface. The ability of CO_2-saturated brine to sink deeper into the aquifer reduces the likelihood of CO_2 leakage, thereby increasing long-term storage security.

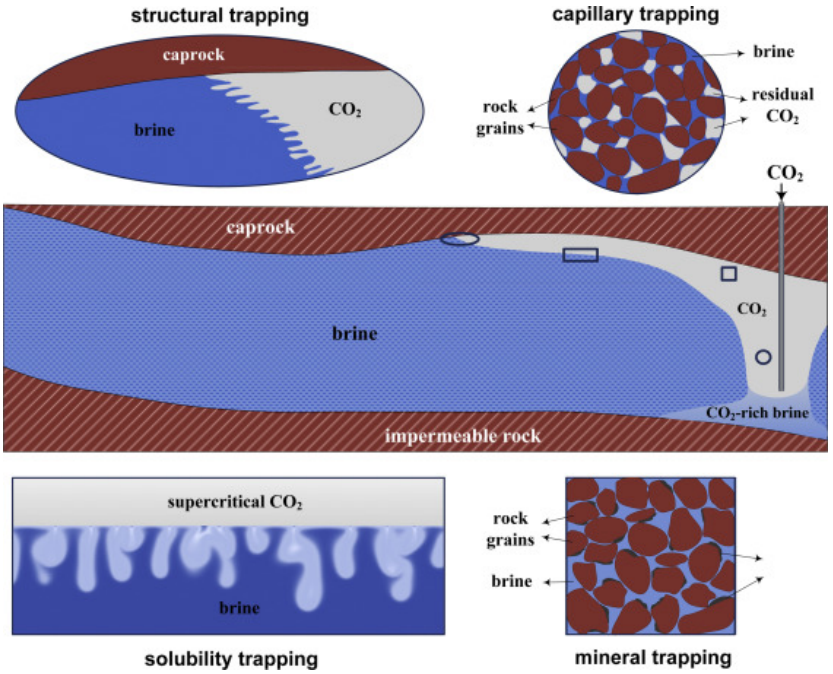

Figure 1.2: A Schematic illustration of fluid dynamics and trapping mechanisms associated with sequestration of CO_2 in saline aquifers, including structural trapping, and capillary trapping, solubility trapping, and mineral trapping adapted from a review paper [11]. Image reproduced with permission of the rights holder, Elsevier see Appendix A1.

Dissolution of CO_2 is considered a key trapping mechanism in GCS [14] and convective dissolution is expected to contribute largely to this process [15], partly because mass transfer by diffusion is very slow. Recent surveys of potential storage sites around the world suggest that the conditions are often met for convective mixing to occur (e.g., [16] using data compiled in [17]). However, estimates on its actual contribution towards storage, its spatial footprint and its time-scale are still mostly uncertain, because of the lack of direct observations at representative subsurface conditions and the intrinsic difficulty in estimating dimensions and properties in heterogeneous rock formations [16].

There has been a wealth of numerical and some experimental studies over the past 10 years aimed at understanding the fundamental physics to assess the trapping potential of

a site accurately. However, the initial condition of the CO_2 brine interface will heavily depend on the nature of the formation and the location of the injection site. In particular, the modelling of convective dissolution has been, by and large, simple 2D representations of a homogeneous, isotropic porous media where a.) the CO_2-brine interface is represented with constant concentration top boundary [18, 19, 20] or b.) a fixed volume of CO_2-brine model with a receding interface [21].

The reality, of course, is a two-phase system where the supercritical CO_2 sits atop an aqueous boundary and between the two exists a capillary transition zone where the effects of capillarity and wettability dictate the distribution of the CO_2 and brine meaning relative permeability effects are important. Additionally, there are swelling effects of the brine as mass is added in the form of CO_2 and so an upward movement of the interface. The true nature of the interface, therefore, is dramatically simplified for the ease of experimentation and simulation; however, increasingly these complexities are being taken into account [22, 23, 24].

At depth in potential geologic carbon sequestration sites, a regime of $Ra = 40 - 12000$ is the most likely to be expected [16]. A bar chart is presented in Figure 1.3 which complies 38 aquifers from around the world sorted according to the expected Rayleigh number. These include 11 major saline aquifers in the United States ($Ra \sim 40 - 4000$, 21 reservoirs in total compiled in [17]), 13 injection sites in the Alberta Basin ($Ra \sim 40 - 400$) [25]) and the Sleipner site in the North Sea ($Ra \sim 4000 - 40000$, 4 cases depending on the assumed pressure/temperature conditions [12]). While these estimates must be used with some precaution due to the intrinsic difficulty in estimating suitable mean permeabilities and dimensions in heterogeneous reservoirs, the perception is that the condition $Ra < 4000$ may be typical in many geologic reservoirs.

Another subsurface application is CO_2 enhanced oil recovery (EOR) where CO_2 is used to increase the amount of oil which can be extracted from a reservoir. The interaction between miscible CO_2-oil systems which cause a similar density instability where the CO_2 rich oil is more dense than the oil [26, 27]. However, CO_2 in oil have a higher solubility limit than CO_2-brine so the density difference can be up to 10% [28] indicating that this could be a much more prevalent phenomenon than CO_2-brine mixing. However, only recently is this becoming a topic of interest with the use of CO_2 for enhanced oil recovery. Interestingly, the CO_2-oil mixture density and viscosity profiles have both been shown to

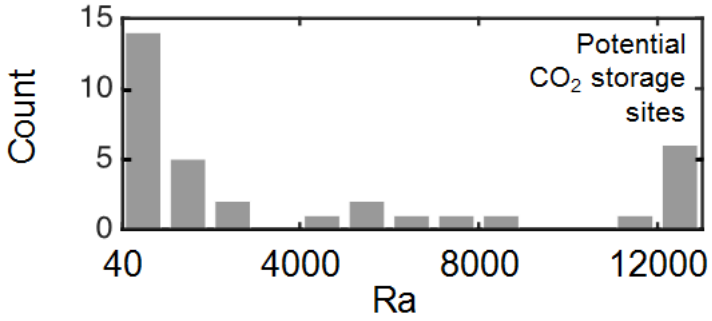

Figure 1.3: A bar chart representing 38 aquifers around the world according to the expected Rayleigh number compiled from reported data [17, 25, 12].

be non-monotonic, where, as density increases viscosity decreases [29], as will be shown in the next chapter these are the characteristics of the model fluid system used throughout this Thesis. However, much more thorough investigation is required on this topic, as the fluid properties heavily depend on the oil composition which can vary dramatically from site to site.

1.4 Convective Dissolution: Regimes and Scaling

Convective dissolution is a process whereby the dissolution of a solute results in a density driven convective overturn and this is followed by a mixing process known as convective mixing. The stages of convective dissolution have been categorised into three [25], five [21, 30, 31, 6], six [8] or even seven [9] independent regimes. However the main ideas are that convection starts, the fingers grow, and then the convection ceases. The details of which are determined by the Rayleigh number and initial conditions.

1.4.1 Onset

Instabilities in an initially flat fluid-fluid interface, occur naturally in real systems both in the field and in the laboratory due to physical imperfections in the interface. These defects may be caused by variations in porosity, permeability or other structural irregularities. When simulating this problem the system must be perturbed numerically, and it has been done via implementing small variations in permeability [32], porosity [30, 33] or concentration [7] field at the interface. Of course, there is a wide body of literature which focuses on the sensitivity of the onset time to the specifics of the perturbation and the

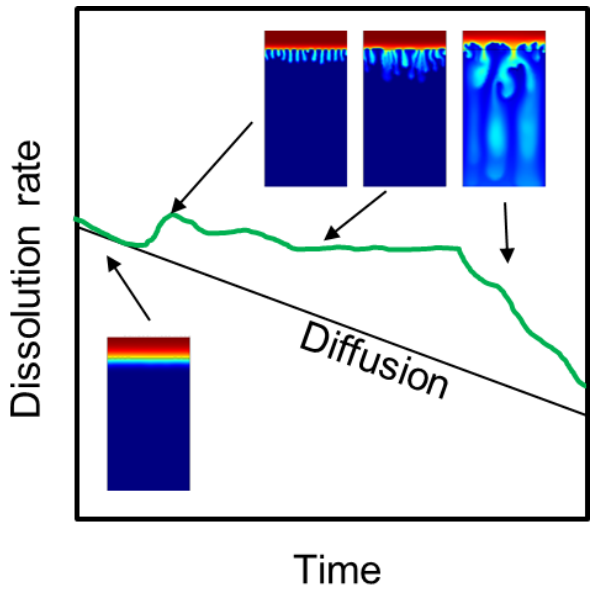

Figure 1.4: An example of the typical profile for the dissolution rate with respect to time for the convective mixing process, the data has been adapted from a recent review paper [11]. Snapshots from the simulation work presented in Chapter 7 are used to illustrate different stages of the process.

analysis methodology employed; Linear Stability Analysis with either the initial-value approach or quasi-steady state approximation are most widely favoured [11].

However, when thinking about convective mixing, the onset, can refer to either the onset of the initial instabilities in the fluid interface or the onset of convection where the process departs from a purely diffusive behaviour. In a recent review [11], the onset of convection is empirically determined by the deviation from the diffusion-only scenario which fits well with description and observations by others. Numerically, the transition between pure diffusion and convection can be described as a function of Ra where the critical time is $t_c = a_1 Ra^{-2}$ and the critical wavenumber is $k_c = b_1 Ra$; a_1 and b_1 are pre factors dependant on the initial perpetuation in the system [11]. But, in practical terms, the onset time compared to the subsequent development of the fingers has been suggested to have little effect on the eventual long-term trapping of CO_2 as the subsequent rate of convection is much more important [34].

1.4.2 Growth

After the onset of convection, there is some debate about the nature of the subsequent regimes. Some authors describe a general 'early convective' regime [18, 25] or simply refer 'fingering' [9]. Others classify the fingering patterns into different regimes such as 'flux

growth' when the process deviates from the classic diffusive time behaviour, characterised by a linear scaling with the square root of time; the 'merging regime' when the initial small fingers merge into larger dominant fingers and the 'reinitiation regime' where new fingers form at the interface [8, 35]. However, importantly, all these behaviours are reported before the plume reaches the bottom of the domain.

The convective mass flux is a tangible metric which quantifies the rate at which CO_2 (for example) dissolves into the brine. There is a characteristic shape of the flux curve which has been reported for density-driven convection and we show an example of this curve in Figure 1.4 where we use data adapted from a recent review paper [11] and 2D COMSOL simulations as illustrations of different stages of the process. Initially, the curve follows the rate predicted by diffusion. As shown in Figure 1.4 during this diffusion controlled period the rate of dissolution is consistent with a purely diffusive scenario. Using 2D simulation results as an example it can be observed that a diffusive boundary layer has accumulated between the fluids but the finger structures are not yet visible.

At the onset of convection, there is a sharp increase in the flux [8, 35, 11] due to increasing surface area of the fingers as a result of lateral dispersion. The fingers then continue to grow and merge together propagating downwards as fresh brine pushes up as visualised in Figure 1.4. Subsequently, there will be a peak in the rate of dissolution followed by, at high Ra ($> 10^3$) a clear, constant flux regime [36, 6, 5] due to the constant supply of fingers or at low Ra ($< 10^3$) the flux continues to decline [11].

The flux can be non-dimensionalised via the Sherwood number Sh, as shown in Equation 1.3 which is essentially a comparison of convective mass transport, k_m to diffusion-only transport, $\mathscr{D}$ with the appropriate length scale, H.

$$Sh = \frac{k_m H}{\mathscr{D}} \tag{1.3}$$

Thus, by evaluating Sh as a function of Ra, the trapping potential of a given site can be estimated based on the physical properties such as the permeability. However, the question then becomes 'What is the accurate Sh- Ra scaling relationship' and 'Over what range of Ra is it applicable?'

The answer to these questions is, of course, not straightforward. In the classical problem of steady-state heat transfer, the scaling proposed is linear in the high Ra range. Many

experimental studies have aimed to reproduce this scaling for the solute case and focused on the high Rayleigh number regime ($\mathcal{O}(Ra) \sim 10^4 - 10^6$) [21, 19, 31, 37, 38, 39]. Interestingly these studies have reported sub-linear scaling in the form of $Sh = c_1 Ra^n$, where c_1 ranges from 0.017 to 0.12 and the exponent is 1 where the scaling is linear and 0.7-0.9 in the sublinear cases. However, this has recently been linked to the use of analogue fluid pairs with mixture density profiles non-monotonic [34, 40]. These profiles which will be discussed throughout this thesis are the result of the solutions where the mixture density is greater than the density of either pure fluid. However, as discussed in Section 1.3 in reality it is likely that reservoirs have a low Ra and as yet there is no consensus on the proper scaling due to variations in experimental protocol and modelling approaches; this will be discussed further in Chapter 3.

1.4.3 Shutdown

Convective shutdown is characterised by the cessation of convection due either to the saturation of the domain where the recirculation of material is no longer possible or the exhaustion of the initial reservoir of CO_2. So, shutdown can be identified by a rapid decrease in the convective flux. Only one study discusses regimes after the shutdown of convection [9] where three additional regimes are observed; slumping, Taylor slumping and late diffusion. These regimes are strongly linked to the nature of the domain which in that case represented an inclined stratified trap in a 2D geometry. The unique behaviours such as accumulation of the heavier CO_2 rich brine at the bottom of the domain while fingers were still being developed leading to late time diffusive behaviours, which were not previously seen in standard rectangular geometries. Further investigation is needed, therefore, for non-ideal and 3D systems as it is clear very small changes to the initial conditions or the nature of the domain can result in radically different regimes.

1.5 Previous Experimental Work

There have been many experimental studies where density-driven convection has been investigated in the context of GCS. These efforts may be broadly divided into two categories, namely (i) studies using high-pressure blind PVT cells and (ii) those using 2D

transparent Hele-Shaw cells. The former can be operated with representative fluids (e.g., supercritical CO_2 and brine) and the rate of dissolution is typically inferred from pressure decay [41, 42, 43] and/or changes in weight [44] inside the closed reactor, or is measured directly by recording the make-up liquid volume needed to maintain a constant pressure in the system [45]. For data reconciliation, some authors have applied the diffusion equation with an effective diffusion coefficient [41, 46], while others have used more rigorous mathematical models that account for both mass- and momentum-conservation in the liquid phase (and that use the bulk molecular diffusivity) [43, 42]. Results from these studies consistently show that under the convective regime the mass-transfer rate across the CO_2/brine interface is indeed much faster than that predicted by Fickian diffusion (with an effective diffusion coefficient that is one to two orders of magnitude larger than the (bulk) molecular diffusivity, depending on initial gas pressure and salt concentration in the brine). Unfortunately, the majority of these observations still refer to the dissolution of CO_2 into the bulk brine, and experiments using porous media have just begun [45, 47]. Also, only in rare cases, the experiment enabled direct visualisation of convective patterns (through an embedded optical side-cell) [43, 44].

1.5.1 Visualisation Protocols

In an early seminal work, [48] photographs of the top free surface of a liquid-saturated $(70 \times 50 \times 8)$ cm^3 rectangular beadpack were used to infer fluid movements within the medium itself; most significantly, the authors demonstrated that cellular structures appear with length-scale $\mathcal{O}(l) \sim 10$ cm, which are not possible in two-dimensional settings, as the latter limit the growth of the plume to two orthogonal directions. These findings were later confirmed by [49], who used a similar experimental approach and extended these observations to the regime $\mathcal{O}(Ra) \sim 1000$. The first images of the convection pattern *within* a porous medium were reported only a few years later by [50, 51] using a shadowgraphic technique and by [52] using Magnetic Resonance Imaging (MRI) for both regular and disordered packings. In these experiments, observations were limited to $\mathcal{O}(Ra) \sim 100$ and to two-dimensions (horizontal flow patterns), and temperature gradients, rather than dissolution driving the mixing process. Nevertheless, by demonstrating a novel ability to image the convective process within opaque media non-invasively, these studies have provided direct evidence that the structure of the medium plays a fundamentally

important role in the determination of the flow pattern.

More recently, with the renewed intent of visualising the convective process, several authors have made use of Hele-Shaw cells with or without beads inside, with analogue fluid-pairs (e.g., methanol and ethylene glycol(MEG)-water [21], water-propylene glycol (PG) [31, 37, 53, 54], gaseous CO_2-water [19, 55] and $KMnO_4$ in water [56, 38]). However, questions have been raised about the use of colour indicators used to visualise flow [19, 55] as they were not capturing the details of the fingering patterns. Instead, the Schlieren technique was proposed, which is extremely sensitive to the refractive index and hence the densities of fluids [55]. With this technique, colour indicators are no longer required, but the drawback is that bead packings cannot be used. Instead, the porous media is represented by a narrow aperture whose width is the reciprocal of which is a proxy for permeability.

Nevertheless, overall, Hele-Shaw experiments have enabled direct access to local measures of convection (e.g., wavelength of the instability, vertical plume velocity, plume width and their statistics) [56, 57]. These experiments have been pivotal in supporting the significant effort that has been dedicated to the study of density-driven convection in porous media by means of numerical simulations (see the recent review [11] and references therein).

Evidence [58, 34, 40] now exist that results using glycol-water analogue fluid pairs may not be directly applicable to the subsurface CO_2/brine system. There are two critical differences between these analogue fluids and the CO_2 brine case i) the analogue is a fully miscible system; this compared to a situation where solubility is finite (CO_2 into brine) changes the nature of the boundary layer, and so the theory shows this can further enhance the dissolution [59]. ii) Crossover in the mixing curve can be manipulated. The methanol and ethylene glycol - water system can be tuned by changing the ratio of methanol to ethylene glycol. As will be shown in the subsequent chapters this changes the maximum density of the fluid but also the mass fraction at which the mixture becomes denser than water. In this case, there is, therefore, a second variable which governs the onset of the process and the fingering dynamics thereafter [40]. These two factors can result in the glycol-water system an overestimation of CO_2-brine if direct comparisons are made. Nevertheless, these studies have demonstrated that despite its inherent chaotic nature, the process of convective mixing can be parametrised in terms of useful macroscopic variables,

such as the Rayleigh, Ra, and Sherwood numbers, Sh (or its counterpart for heat transfer studies, the Nusselt number, Nu).

1.6 The Role of Permeability Heterogeneity

The studies discussed in the previous section are all focused on homogeneous porous media or porous media analogues (Hele-Shaw cells). However, in reality the subsurface is neither homogeneous nor isotropic. Geological formations form a variety of complex permeability patterns that range from the pore to the reservoir scale, and this permeability heterogeneity will have significant impacts on each stage of convective dissolution as the permeability is a key parameter in the theoretical scaling of onset time, dissolution flux and shut-down time.

In natural formations, sedimentary layering can cause orders of magnitude differences in the vertical and horizontal permeability and this can be conceptualised with the idea of permeability anisotropy. This idea can be readily applied to models by varying the permeability tensor in different directions.

Many early studies focus on how the onset of convection is influenced by anisotropic conditions [60, 61, 62, 15, 63] because from a practical point of view it is first critical to verify (at least theoretically) that the presence of heterogeneity does not suppress the convective process completely. The consensus is that vertical permeability is the primary determiner for changes to the onset and rate of dissolution. So as the vertical permeability is usually lower compared to the horizontal permeability, the instability will be increasingly stabilised until a purely diffusive regime is reached and convection is halted. Similarly, in some cases, the flux has been found to scale with the square inverse of the permeability ratio [60, 62]. Experimentally, it would be challenging to replicate anisotropic conditions with a bead pack, but in one study the effect of grain size distribution was investigated. In that study, it was reported that there was have little effect on the dissolution rate but only when the effects of hydrodynamic dispersion, as a result of larger grain size, are taken into account [64].

Heterogeneity can be quantified by the Dykstra-Parsons coefficient (DP) where DP = 1 - k_{16}/k_{50} where k_{16} and k_{50} are the 16th and 50th percentile of a log-normal distribution of the permeability [61]. So, when DP = 0 there is no variation, and this increases as

there permeability field becomes more heterogeneous. The behaviours of the fingers were categorised into three regimes [63]. At DP$<$ 0.2 the fingering behaviour resembles the homogeneous analogue, but the flux is higher for the heterogeneous case. The second regime is 'Channelling' for $0.2 < DP < 0.6$ (depending on the correlation length) where preferential pathways of flow were observed and a flux also slightly higher than the equivalent homogeneous case. The third regime is at high DP where there is a high degree of heterogeneity, and the flow becomes dispersive as convection is not observed. These results were replicated in later works [65, 66]. However, the DP coefficient is a rather simplistic measure of heterogeneity and takes no account of the spatial distribution thus the results would be strongly dependent on the correlation length which is not fully addressed in the literature.

Thin horizontal barrier heterogeneity is another common configuration of heterogeneity that has been presented in the literature [60, 67]. The thickness of the barrier, the spacing between the gaps and the distance between layers are all parameters which can be varied and used to calculate an effective permeability. In general, it was concluded that as the gap size or the distance between layers is increased, the dissolution flux increases as, similar to the anisotropic case, the vertical permeability is higher. Furthermore, it was found that the rate is well approximated by the equivalent homogeneous anisotropic model, indicating that the flow is determined by the bulk properties and not the specific configuration of the barriers [68]. However, the onset time is coupled to the barrier configuration and cannot be scaled with the effective permeability. Both of these assertions have also been observed in 2D [67] and 3D simulations [69] and will be discussed in Chapter 6.

The final configuration of heterogeneity is at an even larger scale where flow encounters lithological interfaces. Experimentalists have used bead or sand packs with simple heterogeneity structures to investigate the effects of large-scale heterogeneity [54, 70, 69]. In one recent study, sand packs have been used in a layered or 'patch-work effect' to imitate the effects of heterogeneity [54]. In the layered case, the results yielded more slender fingers in the layers of high permeability and a faster formation time compared to the layers with lower permeability where there was greater lateral finger spreading, and later onset of convection flowed by a progression of the fingering. These cases highlight that in very low permeability zones convection is not the dominant mixing mechanism but can lead to trapping due to immobilisation of the plume. In the chequered case, in

addition to the previous results, preferential channelling was seen in the path of higher permeability. These results can be viewed to have some similarity to the Sleipner field where the mudstone horizons act like areas of low permeability directing the plume and increasing the surface area for dissolution [53].

Throughout the current literature, there have been calls for experimental observations in non-homogeneous idealised systems. However, as yet, there are very few experimental studies on the effect of large or small scale heterogeneity on the process of convective dissolution. Nor, have there been any 3D observations of the effects of heterogeneity on convective mixing.

1.7 From 2D to 3D

For the particular problem of convective dissolution it has been argued that the theoretical linear stability analysis predicts identical wavenumbers for the 2D and 3D case [11] implying that 3D investigation was not an imperative. The assumption that parallels could be drawn between the 2D and 3D case along with the computing limitations resulting in a large body of work in 2D. These models provided a great insight into the fundamentals of the process where theoretical estimated for the onset and flux could be compared to numerics. However, these 2D models represent idealised systems with unrealistic boundary conditions such as constant concentration or infinite boundaries. Recently though, with advances in technology, there have been a handful of studies which examine convective mixing in 3D [30, 71, 72, 73]. As the reality of the subsurface can now be incorporated more fully into the models the need for 3D experimental validation has never been more great.

However, the convection process in a porous medium is inherently three-dimensional and concerns have been raised with regards to the limitations of two-dimensional experiments (or of their numerical counterparts) [49] and to the applicability of the obtained scaling laws. On the one hand, some authors have proposed that for $Ra > 2000$, a scaling relationship exists for the convective mixing process that is universal, both in two- and three-dimensions [71]. On the other hand, results from numerical simulations suggest that in three-dimensions the dissolution flux is 25-40% larger than in two-dimensions [30, 74] and the fingers grow bigger (thus leading to faster penetration) [75]. Experimental

validation of these findings is still lacking, and, as yet, we have been unable to find any reports of direct observation of convective dissolution in a real rock sample.

Because of the inherent difficulty of imaging the convective process within an opaque medium non-invasively, very limited experimental observations exist of density-driven convection in three-dimensional porous media. In recent work, X-ray CT and the MEG-brine fluid pair [76] and brine-water fluid pair [39] are used to visualise flow in a 3D cylindrical cell with an emphasis on the effect of dispersion. They report that mechanical dispersion strongly affects the finger structure, by resulting in merging of adjacent fingers and a reduction in the onset time [39] in line with numerical studies which report up to two orders of magnitude decrease in the onset times by accounting for dispersion [77]. However, these studies are conducted at length scales on the order of mm with permeabilities and Ra (5000-16,000) outside the range that is expected in the field.

So, with the increasing computer power and investment in imaging equipment for geoscientific applications, the questions of 3D convective mixing may be finally answered. This thesis aims to shed some light on these questions and fill gaps in the literature.

1.8 Layout

In this thesis we aim to address questions surrounding 3D convective mixing. First in Chapter 2 we characterise the components and then present the experimental methodology that will underpin all but one of the subsequent chapters. In all of the experiments, commercially produced boro-silica beads are used to create an optically opaque porous media requiring CT scanning to visualise the flow processes occurring due to buoyancy. In the first part of Chapter 2, the beads are characterised via the micro-CT images where the particle size distribution, i.e. average bead diameter is obtained along with the porosity. Both these parameters are vital in determining the correct Rayleigh number. We go on to characterise the fluids used in the experiments fully; the densities and viscosities of the pure fluids and the fluid mixtures are presented. We confirm the non-monotonic mixture curve and report the density difference used to calculate Ra. Next, we describe the equipment used and the novel protocol established to run and process the data from these experiments. And finally, a simple diffusion model is presented.

In Chapter 3, we present multidimensional observations of convective dissolution in simple

porous media using X-ray Computed Tomography (X-ray CT) for the MEG-brine fluid pair and then the BEG-brine fluid pair in spherical geometry. Together with the recent work by [39, 76], we provide the first non-invasive determinations of three-dimensional patterns in opaque, random porous media. Experiments are carried out in the regime $\mathcal{O}(Ra) \sim 1000$, and the mixing process is quantified using various metrics, including the rate of dissolution and effective diffusion coefficients. Observations are compared to the limiting case of a purely diffusive scenario, which further enables the investigation of a $Sh - Ra$ scaling law and its comparison with results reported in the literature using a similar fluid pair.

The work of Chapter 3 is extended in Chapter 4 to explore the effect of the system geometry. A cube and cylinder are selected as a comparison to the sphere used for the previous experiments. We supposed that the changing cross section of the bowl was affecting the flow of the fingers and the three-dimensional nature of the fingers. We hypothesised that in the bowl the fingers would grow larger and have a greater potential for lateral movement than in a system with a constant cross section. A similar analysis as presented in Chapter 3 was conducted on each of the experiments carried out in the two new geometries. The results were compared by way of the mass flux, onset times and shut down times along with 3D reconstructions at various times. It was found that indeed the geometry has an impact on the flow behaviours and specifically the macroscopic behaviours of a cube and the cylinder were always slower than the sphere. We suggest based on the evidence here that this slowdown of the fingers is due to the smaller more well-defined fingers in the cube and cylinder. If the finger speed is only a result of the density differential, then the speed of dissolution should be the same for each geometry. However, we hypothesize that in the bowl, the fingers a subjected to more lateral dispersion and so this enhances the speed of mixing. We also observe in this chapter that the macroscopic behaviour is a function of a changing or constant cross section and not on the precise geometry itself.

In Chapter 5 & 6 we return to the bowl but with the addition of simple heterogeneity and conduct a systematic review of a single layer of lower permeability in Chapter 5 and look at the influences of discontinuous heterogeneity in Chapter 6. A new metric, the Impedance, is introduced to quantify the resistivity of the packing which is varied from 0.3-7 in Chapter 5 by varying the thickness and permeability of the layer. Interestingly we did not find a clear relationship between the impedance and the rate of dissolution.

Initially we assumed that as the impedance was increased the rate of dissolution would decrease however the results suggest that the rate is dependent on how the impedance was changed (by either changing the thickness of the layer or the permeability ratio) and not only the absolute value of impedance. If the flow cannot be predicted by the global measures of impedance it suggests that the flow behaviours are highly localised, and this also calls into question the validity of other global scaling parameters such as Ra. However, this assertion is questioned in Chapter 6 where we observe that the rate of dissolution can be parametrised by Ra using averaged permeability. In Chapter 6 three cases are considered with increasingly complex patterns; first, two discontinuous layers are introduced then a patchwork of 3D layers and finally a random permeability field.

The final results chapter presents numerical simulations conducted in a 2D domain using COMSOL. In the first part of the Chapter the Ra is investigated by changing the permeability and the dissolution flux and dilution index are compared. A $Sh - Ra$ scaling law is reported which is surprisingly close to the experimental scaling shown in Chapter 3 and Chapter 6. The second part of Chapter 7 introduces permeability heterogeneity similar to that used in the experimental chapters.

This thesis concludes with a summary of the significant findings from this work and proposals for its continuation.

Chapter 2

Characterisation of Fluids and Materials and the Experimental Methodology

This Chapter provides details of the porous medium and the fluid pairs used in the experiments presented throughout this Thesis. The experimental apparatus is outlined along with the equipment used and the data processing techniques which are implemented. Finally, a simple diffusion model is presented.

2.1 Characterisation

2.1.1 Porous Medium

The porous media used in all the experiments presented in this Thesis is a random close packing of soda glass ballotini (SiLibeads®, supplied by VWR, UK). We chose to use bead pack instead of consolidated rocks mainly for reasons of practicality. We saw the bead pack as a step in between empty hele-shaw cells and a real rock system. Our aim was to visualise convective mixing in an idealised packing first at ambient conditions. Secondly, a bead pack is simple to set up and removed many of the complications of pumping liquid into a consolidated sample whist achieving a flat initial interface. Finally, the bead pack enabled precise placement of layers with well characterised permeabilities in the later experimental campaigns.

The porosity of this type of packing is $\phi \approx 0.36$ and its permeability, k, is estimated from the Kozeny-Carman equation which is based on the porosity and the particle diameter d_{p}

$$k = \frac{\phi^3 d_{\mathrm{p}}^2}{150(1-\phi)^2} \tag{2.1}$$

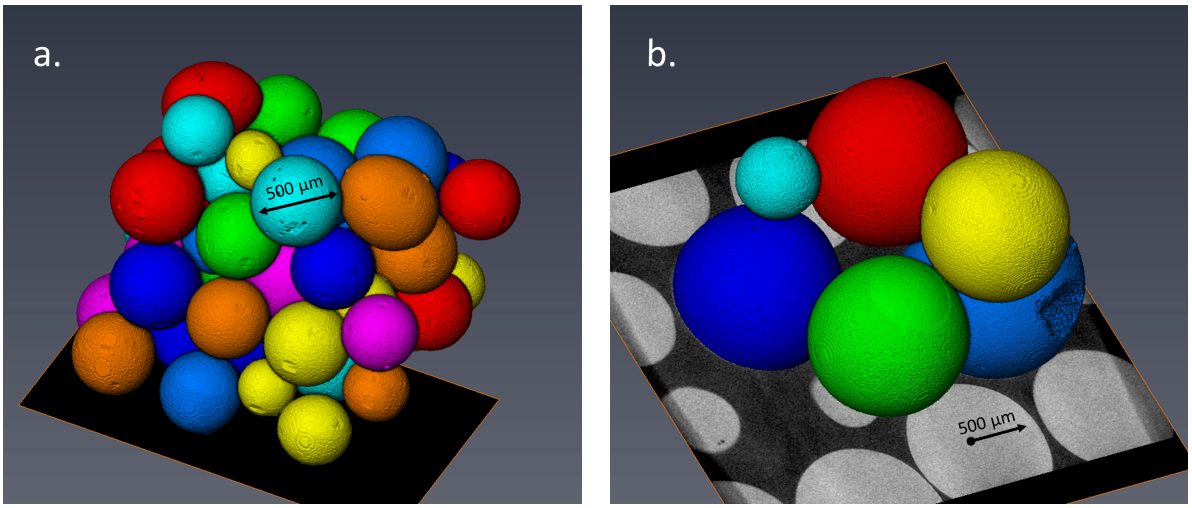

Figure 2.1: Aviso reconstructions of micro CT x-ray images of SiLibeads® with an average particle diameter of a. 522μm b.1044μm. In each image the colours denote individual beads.

Permeability is one of the parameters that is used to calculate Ra and so it is important that this be accurate. In this case, as the permeability is estimated from these two quantities, it is important to verify manufacturers specifications for both the porosity and the particle size of the beads. To that end, dry micro-CT x-ray scans were taken by Dr. Saurabh Shah with a resolution of 4μm of two of bead sizes used in the experiments presented in later chapters. Figure 2.1 shows the reconstructed micro-CT images for a. 0.5mm and b. 1mm beads, these images were prepared by Dr J.P.Crawshaw. Using Avizo, a commercially available image processing software, the averaged diameter was estimated and found to be a. 522 μm and b. 10448 μm for each of these samples. This is fairly close to the manufactures estimate of bead diameter and we can observe there is a random close packing therefore the assumptions of the Kozeny-Carman are vilified so for a. $k_{d_{\mathrm{p,a}}} = 1.9 \times 10^{-10}$ m^2 and b. $k_{d_{\mathrm{p,b}}} = 7.6 \times 10^{-10}$ m^2.

2.1.2 Fluids: Methanol and Ethylene Glycol - Brine

Convective dissolution is a process which is underpinned by a small density difference between two fluids which are lying one atop of the other. The practical applications

include carbon sequestration and CO_2 enhanced oil recovery. These processes occur deep underground at high temperatures and pressures by using analogue fluids convective dissolution can be investigated at laboratory conditions. In the literature, the two most commonly used fluid pairs which have been used to study convective dissolution are the water-Propleyne Glycol system [31, 37, 53, 54] and the MEG-water system [21, 76]. Both of these systems have an interesting and useful mixing curve as the mixture of the two fluids is more dense than either of the constituents across parts of the concentration range. Hence, the system is initially stable which lends itself to establishing a flat interface between the fluids. Here, the MEG-water system is used for the majority of the experiments which are solutions of methanol and ethylene glycol (MEG, fluid 1) and brine (fluid 2). This fluid pair has many advantages over the PG system as it allows for the density difference, $\Delta\rho_{\max}$, to be varied by changing the ratio of methanol to ethylene-glycol and thus by changing the maximum density difference a range of Ra number can be investigated. Practically it is necessary to dope fluid 1 with a high atomic weight chemical such as potassium iodine for visualisation by X-ray CT. However this is will also increase the density of that fluid so, in order to maintain the proper mixing curve, fluid 2 must also be doped with a lower weight salt, sodium chloride, which will not be visible to X-rays; this procedure was first published by Wang et al., 2016. In the case of water-PG, it is possible to dope the water with KI, but sodium chloride is not soluble in propylene glycol. Thus MEG was chosen as the surrogate fluid.

In particular, three mixtures of ethylene glycol and methanol (both anhydrous, 99.8%, Sigma-Aldrich) were prepared that differ in wt% ethylene-glycol, namely 55 wt% (MEG55), 57 wt% (MEG57) and 59 wt% (MEG59). The obtained solutions are subsequently doped with 9 wt% potassium iodide (KI, ReagentPlus®, 99%, Sigma Aldrich) to achieve high X-ray imaging contrast for the experiments. Only one brine solution is used that contains 6 wt% sodium chloride (NaCl, $>$ 99%, Sigma Aldrich) in distilled water.

The density of the pure solutions and their mixtures have been measured using an oscillating U-tube density meter (DM5000 by Anton Paar) at 20°C and 1 atm. For each measurement, approximately 3 mL of the solution was used, and the density was taken to be the average of three repeated measurements. The obtained density curves are shown in Figure 2.2 as a function of the mass fraction of MEG, w, where the experimental values (symbols) are plotted together with fitted polynomial curves (parameters provided

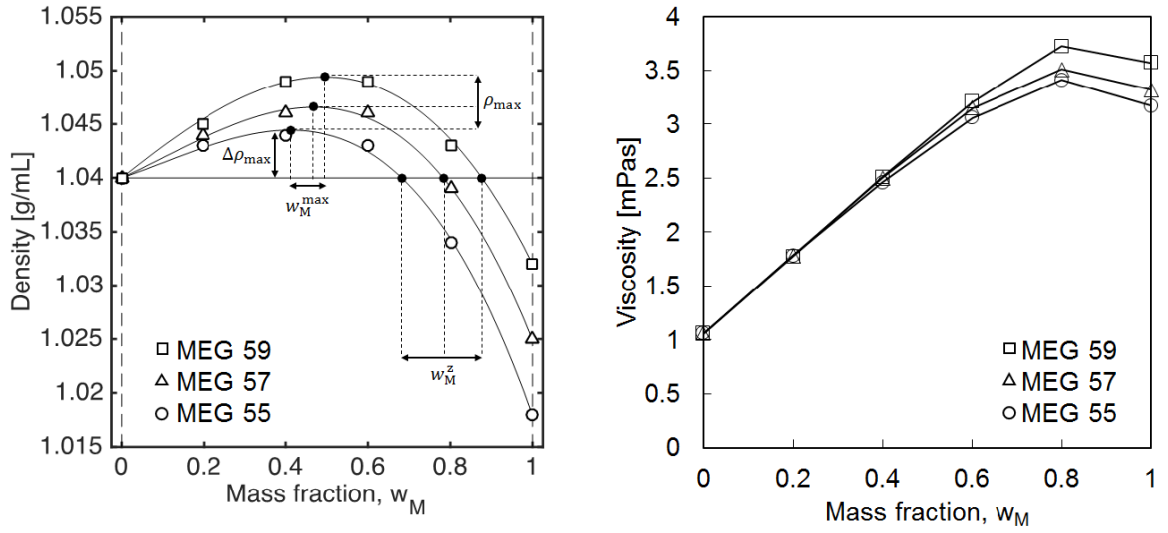

Figure 2.2: (a) Density and (b) Viscosity curves of the three solution-pairs used in this study, namely MEG55, MEG57 and MEG59 (solution 1 with mass fraction w) mixed with brine (solution 2 with mass fraction, $1-w$). In both plots, symbols are experimental results, while in (a) the curves represent fitted polynomials of the form, $\rho = a_0 + a_1 w + a_2 w^2 + a_3 w^3$. Characteristic points on (a) are the maximum density difference achieved upon mixing ($\Delta\rho_{\max}$), the corresponding weight fraction of the solution ($w^{\max}$) and the point of neutral buoyancy, w^0). The values of these parameters are given in Table 2.1.

in the Appendix A2. These curves present a characteristic non-monotonic profile with a maximum at intermediate MEG concentrations ($w = 0.4 - 0.5$) and a density larger than that of pure brine ($\rho(w) > \rho_2$), whereas at larger concentrations ($w = 0.7 - 0.9$) the solution becomes buoyant ($\rho_1 < \rho(w) < \rho_2$). Error bars are not shown in the figure because they are smaller than the symbols.

The viscosities of the pure solutions and their mixtures were rheologically characterised using a Thermo Scientific Haake Mars 60 Modular Advanced Rheometer System and Haake RheoWin software by Andrew Russell. The fluids underwent two shear rate controlled tests, both at 20C, sweeping stepwise from 200-10 s^{-1} and then back up from 10-200 s^{-1}, in increments of $10s^{-1}$. 20 data points were measured per test, with each data point being measured for 30 s, resulting in a total time of 600 s per shear rate sweep. The resulting viscosity and shear stress data were collected using the Haake Rheowin software, and due to the Newtonian behaviour of the fluids, the viscosity values were averaged to obtain an absolute value for each fluid. The obtained viscosity curves are shown in Figure 2.2b as a function of wt% MEG, w, where the experimental values (symbols) are plotted. It is observed that the viscosity of the pure MEG is $\approx 3\times$ larger than the brine. Looking more closely for each MEG ratio the curves are almost identical until a mass fraction

of MEG of 0.4 then the curves spilt according to MEG ratio where the 59 is the most viscous (as it contains the most ethylene glycol) and 55 the least viscous. Unexpectedly, at a mass fractions of MEG = 0.8, a maximum is observed. This peak is a very unusual as it indicates non-linearity in the viscosity which has so far not been reported in the literature nor has this been investigated with respect to the problem of convective mixing.

For the sake of curiosity, the viscosity of the fluids without salts was also measured. In Figure 2.3 the viscosity of MEG59 with (filled symbols) and without (empty symbols) the addition of salts is presented. The viscosity of the solutions with salts is consistently higher than without salt. Therefore, it appears that the addition of salts dampens the underlying non-linearity in the viscosity mixing curve.

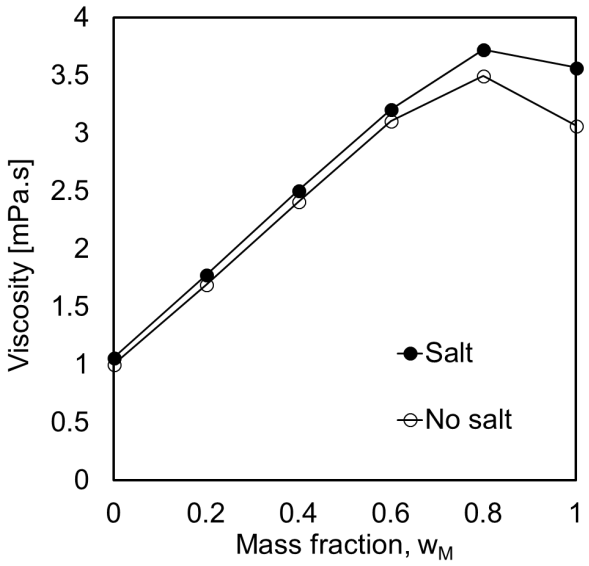

Figure 2.3: Viscosity curves of MEG59 (solution 1 with mass fraction w) mixed with brine (solution 2 with mass fraction, $1-w$) with the addition of salt (filled points) and without the addition of salts(empty points). The points represent experimental data and the lines are fitted curves for clarity.

2.1.3 Fluids: Tertiary Butanol and Ethylene Glycol - Brine

The fluid pair MEG/brine was initially chosen as it allowed for the Rayleigh number range to be investigated by changing the maximum density difference from the different MEG ratios. Another fluid-pair under investigation is tertiary butanol (other isomers of butanol are not miscible with water) and ethylene glycol with water or BEG-water. BEG is used to investigate the impact of viscosity ratio on the process of convective dissolution.

The density and the viscosity of the BEG-water was characterised by the same method

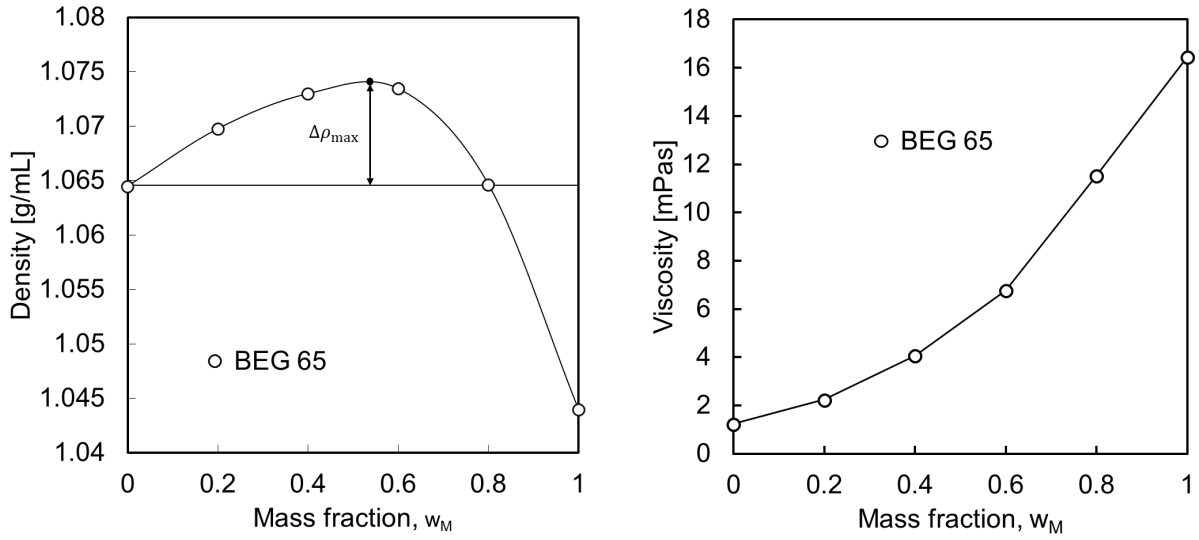

Figure 2.4: ((a) Density and (b) Viscosity curves of BEG65 (solution 1 with mass fraction w) mixed with brine (solution 2 with mass fraction, $1 - w$). In both plots, symbols are experimental results, while in (a) the curves represent fitted polynomials of the form, $\rho = a_0 + a_1 w + a_2 w^2 + a_3 w^3$. Characteristic points on (a) are the maximum density difference achieved upon mixing ($\Delta\rho_{\max}$), the corresponding weight fraction of the solution ($w^{\max}$) and the point of neutral buoyancy, w^0). The values of these parameters are given in Table 2.1.

outlined in the previous section and is presented in Figure 2.4 a&b. A very similar density curve emerges for the BEG as compared to the MEG system where the mixture is more dense than either of the constituents. The density difference observed is within a similar range to the MEG as is the crossover point. The viscosity curve, however, is completely different. Here no maximum is observed instead a smooth concave transition was measured.

Table 2.1: Characteristic metrics of the density curves that represent the three solution pairs used in this study, namely maximum density difference between the two solutions ($\Delta\rho_{\max}/\rho_2$, where $\rho_2 = 1.040$ g/mL is the initial density of the brine), weight fraction at maximum density ($w^{\max}$) and at neutral buoyancy w^0. The Rayleigh number, Ra, is calculated from Eq. 1.1 assuming $k_{d_{\mathrm{p,a}}} = 1.9 \times 10^{-10}$ m^2.

Solution	ρ_1[g/mL]	$\Delta\rho_{\max}/\rho_2$	$w^{\max}$	w^0	Ra
MEG55/brine	1.018	0.4%	0.41	0.68	2150
MEG57/brine	1.025	0.6%	0.47	0.78	3230
MEG59/brine	1.032	0.9%	0.50	0.88	4610
BEG65/brine	1.045	0.85%	0.53	0.8	3900

The key characteristic properties of the solutions are summarised in Table 2.1, together with estimates of the Rayleigh number, Ra as shown in Eq. 1.1. Where $g = 9.81$ m/s^2 is the acceleration due to gravity and $H_{\mathrm{B}} = 10$ cm. Other relevant properties include the

brine viscosity, $\mu_2 = 1.090$ mPa.s, and the average diffusion coefficient in the bulk solution, $\mathscr{D} = 1 \times 10^{-9}$ m^2/s. The latter is assumed to be independent of the solution concentration, based on observations reported in the literature for ethylene-glycol (EG)-water mixtures, where $\mathscr{D} = 1.2 - 0.75 \times 10^{-9}$ m^2/s for $w_{\mathrm{EG}} = 0 - 0.5$ [78].

2.2 Experimental Procedure and Imaging

Imaging the three-dimensional behaviour of convective dissolution is one of the novelties of this work and was only possible with the availability of a medical CT scanner. In this section, the experimental procedure developed for this purpose is outlined and the two scanners used to complete this task are discussed.

The majority of the experiments presented in this Thesis have been conducted in a 3 L acrylic plastic bowl packed with soda glass ballotini (SiLibeads®, supplied by VWR, UK). This spherical geometry was selected to reduce imaging artefacts associated with the acquisition of X-ray tomograms of objects with straight edges, such as a cylinder or cube, in the Universal systems HD-350 X-ray CT scanner. The bowl is depicted in Figure 2.5; it has dimensions 18 cm × 150 cm ($d \times H$, where $H = H_{\mathrm{T}} + H_{\mathrm{B}}$) and an opening diameter of 11 cm.

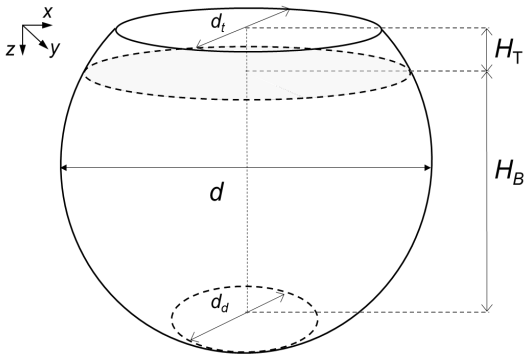

Figure 2.5: Drawing of the experimental geometry used for the convective dissolution experiments. The bowl is packed with soda glass ballotini ($d_{\mathrm{p}} \approx 0.5$ mm); the top and bottom sections of the bowl ($H_{\mathrm{B}}/H_{\mathrm{T}} \approx 5.5$) are initially saturated with MEG and brine solutions, respectively. Other dimensions are: $d = 18$ cm, $d_{\mathrm{t}} = 11$ cm and $d_{\mathrm{b}} = 8.5$ cm.

The bowl is wet-packed using solution 2 (brine) for about 90% of its volume, corresponding to height, $H_{\mathrm{B}} \approx 13$ cm, and it is placed on the bed of the scanning instrument (Universal Systems HD-350 X-ray CT scanner). A dense slurry of solution 1 (MEG) and beads are prepared separately and poured in the bowl carefully ($H_{\mathrm{B}} \approx 2$ cm), to minimise

disturbances to the interface between the two fluids. The bowl is overfilled to reduce the volume to trapped air in the MEG layer and levelled before the bowl is covered with a transparent plastic film which prevents evaporation of the MEG/BEG. Then, the first CT scan is taken. The time needed to pour the MEG slurry and to complete the first scan always took less than 2 minutes.

2.2.1 Universal Systems HD-350 X-ray CT Scanner

Prior to this work, the Universal Systems HD-350 X-ray CT scanner was used initially in the 'stop and go' mode. An alternative is the 'helical' mode in which the sample is scanned continuously as the source and detectors rotate around it. The main advantages in operating the scanner in the helical rather than the 'stop-and-go' mode are that (i) scanning time is significantly reduced (1-2 min vs 10 min) and (ii) shaking of the beadpack is minimised.

Table 2.2: The combinations of thickness, index and pitch which were investigated and the corresponding notation

Thickness $[mm]$	Pitch	Index $[mm]$	Notation
1	1	1	T1I1P1
1	1	2	T1I1P2
1	2	1	T1I2P1
1	2	2	T1I2P2
2	1	1	T2I1P1
2	1	2	T2I1P2
2	2	1	T2I2P1
2	2	2	T2I2P2

However, helical scanning requires four parameters to be set which determine how the data set is collected. These are the thickness, the index, the pitch and the scanning length. To quantify and understand the error in the measurements we performed a parameter analysis where the scanning length was kept constant and the thickness, pitch and index were varied. The bowl was filled with beads saturated with either water, MEG-KI or NaCl(aq). Table 2.2 indicates the combinations of parameters used and the notation to denote these. Then an error analysis was performed based on a method previously published [79]. This method aims to quantify the error by computing the standard deviation in the voxel

values; this is achieved by taking the difference of consecutive sets of helical scans and calculating the standard deviation for the resulting distribution of values.

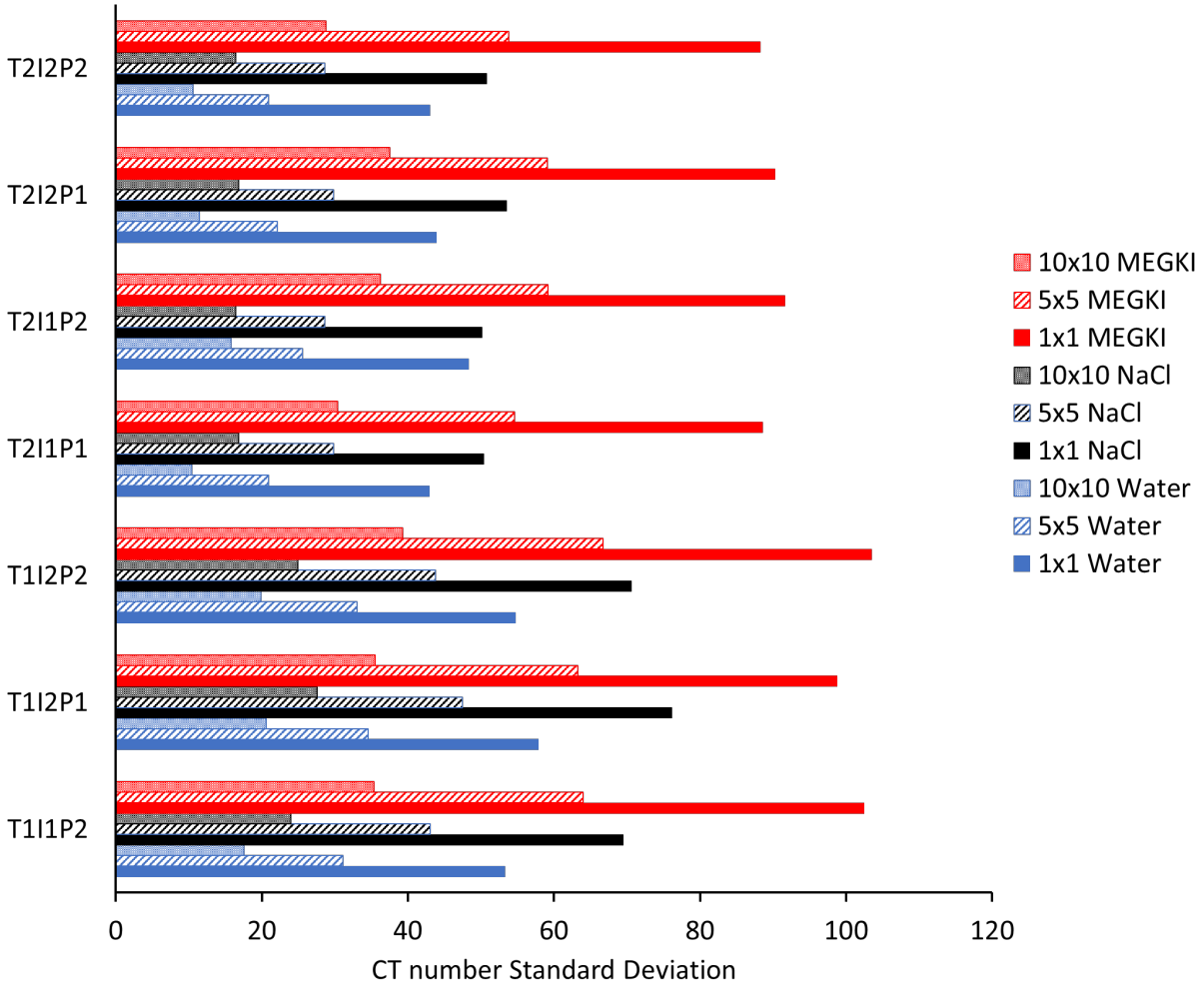

Figure 2.6: Standard deviation of the measured CT number for the various combinations of scanning parameters given a coarsening scheme for three fluids; water, 6wt% NaCl solution and 9wt% KI in MEG.

The original voxel size in the x-y plane is 0.458 × 0.458 mm, we then coarsen the images based on a 5×5 and 10×10 scheme and repeat the process. A 5×5 scheme will result in a voxel size of 2.29mm × 2.29mm, and a 10×10 scheme will give a voxel size of 4.58mm × 4.58mm. In this case, we do not coarsen voxels in the x-z or y-z plane.

The collated results are reported in Figure 2.6 and show the standard deviation for the three fluids of interest with varying parameters and coarsening schemes. It can be observed that the deviation is higher for MEG saturated bowl at around 100 HU compared to the NaCl or water which has a standard deviation of about 60 HU. The discrepancy can be explained as a consequence of higher average CT number of the MEG solution, and so the absolute number of the deviation is higher. We also observe, as expected, the most

important factor in reducing the error is coarsening the images. We look at a 5×5 and 10×10 scheme and see a systematic reduction in the error with increasing voxel size.

Also, the uncertainty decreases with increasing slice thickness; this parameter has a strong effect on measurement precision. We suggest this is because the thicker the slice, the greater the volume over which the scan is taken leading to a more accurate measurement of that volume. We choose to match the index with the thickness so that each slice is a representation of a unique volume. Similarly to avoid interpolation we set the pitch to 1 so the reconstruction is obtained where no space is left between the helices. This combination does not result in the lowest possible error but reduces the error while satisfying physical restraints. The standard deviation reported above translates into approximately 5% error in the measured values for the coarsened data and a 3.5% error of the 5×5 scheme which has been most widely used in this work.

Therefore, for the image acquisition, the following set of parameters was applied: field-of-view (24×24) cm^2; energy level of radiation 120 eV; tube current 150 mA. The scanner is operated in helical mode with the pitch set to 1, the index to 2, the number of revolutions to 70 and the total scanning length to 140 mm; this produces 71 2 mm-tick tomograms per complete scan with a voxel size in the $(x - y)$ plane of (0.4688×0.4688) mm^2. The entire bowl is scanned every $10 - 30$ minutes for up to 10 hours thus collecting a total of about 20 CT scans, each scans took 70 seconds to complete. For subsequent analysis, the latter are averaged over a 5×5 rectangular grid to produce $(2.3 \times 2.3 \times 2)$ mm^3 cubic voxels, thereby reducing the uncertainty of the CT reading to ± 48 HU (corresponding to an error of approximately 10wt.% on the measured solute concentration at the voxel level).

2.2.2 Toshiba Aquilion 64 Slice X-ray CT Scanner

New equipment became available partway through the project which resulted in faster scanning time and less noisy images. The Toshiba Aquilion 64 slice scanner is a refurbished medical scanner capable of taking 64 simultaneous slices of a given 0.5 mm with each 350 ms revolution. So, a single slice of thickness 0.5 mm is now the average of the 64 detections as opposed to 1 in the Universal Systems scanner. The imaging parameters bare some similarity between the scanners, namely, the energy level of 120 eV; tube current

150 mA, a pitch of 1. However, now the acquisition time is 15 s, and image thickness is 1 mm which results in ≈ 160 tomograms per complete scan with a voxel size in the $(x - z)$ plane of (0.47×0.47) mm[1]. The Aquilion has inbuilt reconstruction algorithms relevant to different body parts here 'Bone High Resolution' was used as the large dense nature of the experiments are best compared to imaging bone, and high resolution produced the best quality images with the least noise. Here the noise after 5×5 coarsening was applied is ± 31 HU. Also as the time resolution is vastly increased, it was now possible to image the very early time behaviour, and so in total, there are between 50-60 discrete time data sets.

2.3 Image Processing

One complete scan takes approximately one minute to complete for the Universal systems scanner and 15 s for the Toshiba so the obtained 3D reconstructions can be considered as still-frames of the mixing process at specific times.

In the derivation of the relevant operating equations in terms of CT numbers, the following assumptions apply: (i) the porosity is constant, and uniform, (ii) volume changes on mixing the two liquid solutions are negligible and (iii) the CT number varies linearly with the weight fraction of KI in solution. Assumption (i) is justified in view of the large size of the voxels ($V_{\text{vox}} \approx 11$ mm^3 corresponding to about 100 beads for the Universal Systems scanner and $V_{\text{vox}} \approx 6$ mm^3 corresponding to about 50 beads for the Toshiba and to an edge-length/bead diameter of ≈ 5, which corresponds to the REV size typically assumed for uniform bead packs [80]). Assumption (ii) applies in this study because any volume change resulting from the mixing between solutions 1 and 2 is very small when compared to the voxel size (< 0.3%rel.). Because of the small density changes associated with mixing (< 3%rel.), we can further assume that volume and mass fractions of solute are approximately equal (see also Figure 2.2b). Assumption (iii) has been verified with an independent experiment, and the results are reported in Appendix A2. Given these assumptions, the following equation is obtained where the CT number in a voxel i at given time t, $CT_i(t)$, is expressed as the linear combination of the CT numbers associated

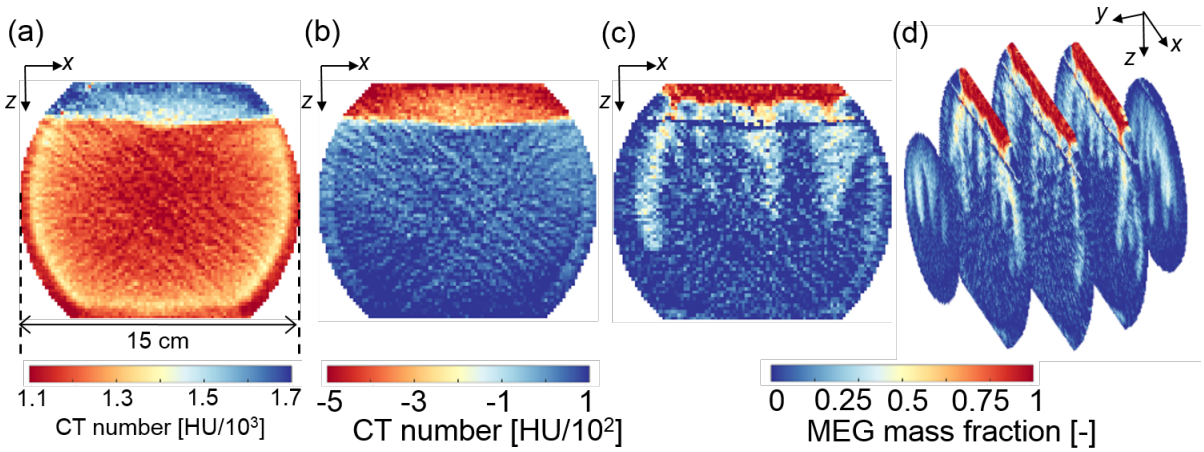

Figure 2.7: The adopted workflow for image processing. (a) The raw tomogram in terms of CT numbers (shown is the central slice of the bowl). (b) Reconstruction of the same slice obtained upon subtraction of scans acquired at different times (shown is the difference between final and initial scans); this procedure removes image noise and enables the identification of the initial interface between the two solutions. (c) Conversion of the tomogram to MEG fraction, $w_i(t)$, using Eq. 2.4. (d) Reconstruction of the entire bowl by applying the same methodology to each slice (total scanning length: 14 cm).

with the volume and mass fractions of each of its components:

$$CT_i(t) = \phi\left[w_i(t)CT_1 + (1 - w_i(t))CT_2\right] + (1 - \phi)CT_\mathrm{s} \tag{2.2}$$

where CT_1 (MEG) and CT_2 (brine) are the CT numbers of the pure liquids, while CT_s is the CT number of the glass beads. As explained in the following, the latter conveniently drops out of the equation upon subtracting scans acquired at different times, while the CT numbers of the pure fluids can be obtained from a calibration that accounts for the material balance in the system.

The workflow that has been followed for image processing is depicted in Figure 2.7, where the central slice taken with the Universal System scanner is shown as an example of general validity. The raw tomogram is presented in Figure 2.7a and evidences the presence of significant beam hardening around the periphery of the bowl. Subtraction of tomograms acquired at identical positions can effectively remove this effect, as shown in Figure 2.7b. Here, the first ($t = t_0$) and final ($t = t_\mathrm{f}$) scans have been subtracted, further enabling the identification of the original interface between the two solutions. Accordingly, the volumes occupied initially by solutions 1 (V_T, MEG) and 2 (V_B, brine) are obtained upon application of a threshold value ($CT = -190$ HU in this study) and by counting the the number of voxels N in each section, i.e. $V_i = N_i V_\mathrm{vox}$, where $i = T, B$. The corresponding total mass of solution 1 and 2 can be readily computed as $M_1 = \phi V_\mathrm{T}\rho_1$ and $M_2 = \phi V_\mathrm{B}\rho_2$.

At the end of the experiment ($t = t_{\mathrm{f}}$), solution 1 (MEG) has completely dissolved and the top section of the bowl (V_{T}) contains only solution 2 (brine, $\widehat{w}_{\mathrm{T}}(t_{\mathrm{f}}) = 0$); the corresponding value in V_{B} is obtained from the following material balance,

$$\widehat{w}_{\mathrm{B}}(t_{\mathrm{f}}) = \frac{M_1}{M_1 + M_2 - \rho_2 V_{\mathrm{T}}} \tag{2.3}$$

We note that the attainment of an inverted concentration profile (as opposed to a uniform distribution) is expected in view of the large difference between the time-scale of convective fluxes and the diffusive counterpart ($Ra > 1000$), and the short duration of our experiments ($\mathcal{O}(t) \sim 100 - 1000$ min) relative to the time scale for diffusion ($\mathcal{O}(t) \sim 10^5$ min). The mass fraction of solute (MEG) in each voxel i in the top, $w_{\mathrm{T},i}(t)$, and bottom sections of the bowl, $w_{\mathrm{B},i}(t)$, can therefore be computed as follows:

$$w_{\mathrm{B},i}(t) = \widehat{w}_{\mathrm{B}}(t_{\mathrm{f}}) \frac{CT_{\mathrm{B},i}(t) - CT_{\mathrm{B,i}}(t_0)}{\widehat{CT}_{\mathrm{B}}(t_{\mathrm{f}}) - \widehat{CT}_{\mathrm{B}}(t_0)} \tag{2.4a}$$

$$w_{\mathrm{T},i}(t) = 1 - \frac{CT_{\mathrm{T},i}(t) - CT_{\mathrm{T}}(t_0)}{\widehat{CT}_{\mathrm{T}}(t_{\mathrm{f}}) - \widehat{CT}_{\mathrm{T}}(t_0)} \tag{2.4b}$$

where $CT_{\mathrm{T},i}(t)$ and $CT_{\mathrm{B},i}(t)$ are the time-dependent CT values in each voxel i, while $\widehat{CT}_{\mathrm{B}}$ and $\widehat{CT}_{\mathrm{T}}$ represent the average of all voxel CT values in the bottom and top sections of the bowl at the initial and final time (t_0 and t_{f}, respectively). The latter are associated with the CT numbers of the pure liquid solutions and are obtained for each experiment independently, e.g., for the top section in Eq. 2.2: $\widehat{CT}_{\mathrm{T}}(t_{\mathrm{f}}) - \widehat{CT}_{\mathrm{T}}(t_0) = \phi(CT_2 - CT_1)$. Equations 2.4a and 2.4b are applied on a voxel scale (as shown in Figure 2.7c for the central slice of the bowl) and the operation is repeated for each slice in the bowl to enable the three-dimensional reconstruction of the temporal and spatial evolution of the process of convective mixing (Figure 2.7d). As an important component in the analysis that follows, the temporal evolution of the total mass of solute in each section (top, T, and bottom, B) is estimated as:

$$m_{\mathrm{B}}(t) = \rho(w_{\mathrm{B}})V_{\mathrm{B}} \tag{2.5a}$$

$$m_{\mathrm{T}}(t) = \rho(w_{\mathrm{T}})V_{\mathrm{T}} \tag{2.5b}$$

where the density of the mixture is computed from the parametrisation of the curves shown in Figure 2.2 as a function of the average mass fraction of the solute in the given section of the bowl, $w_{\mathrm{B}}(t)$ or $w_{\mathrm{T}}(t)$, which are estimated by using section-averaged $CT(t)$ numbers in Equations 2.4a and 2.4b.

2.4 Diffusion Model

2.4.1 Changing Cross-Section

The outcomes from each experiment presented in this Thesis are compared to those associated with a purely diffusive scenario, to quantify any enhancement of mixing introduced by the convective mixing process. So, the diffusion process is modelled by the numerical solution of the one-dimensional diffusion equation in a sphere, to closely represent the geometry used in the majority of the experiments. The equation can be written as:

$$A(z)\phi\frac{\partial c}{\partial t} = \frac{\partial}{\partial z}\left(\phi\mathscr{D}A(z)\frac{\partial c}{\partial z}\right) \tag{2.6}$$

where c is the concentration of MEG in the brine solution, ϕ is the porosity, $\mathscr{D}$ is the molecular diffusion coefficient, and z and t are the spatial (vertical) and temporal coordinates. The cross-sectional area can be conveniently described as a function of z, i.e. $A(z) = \pi(z+h)[d-(z+h)]$ for $-h \leq z \leq d-h$, where d is the diameter of the sphere, h is defined so that $A(z=0) = \pi {d_t}^2/4$ and z increases downwards (see Figure 2.5). Eq. 2.6 can be thus simplified further to give,

$$\frac{\partial c}{\partial t} = \mathscr{D}\left[\frac{\partial^2 c}{\partial z^2} + \frac{\partial c}{\partial z}\left(\frac{1}{z+h} - \frac{1}{d-(z+h)}\right)\right] \tag{2.7}$$

This partial differential equation is discretised in space using the finite-difference method with 500 grid points corresponding to a constant width $\Delta z \approx 0.3$ mm. To this aim, the space derivatives are approximated using the central difference operator for each internal node, and a no-flux condition is imposed at each boundary, i.e.

$$\left.\frac{\partial c}{\partial z}\right|_{z=z_\mathrm{t}} = \left.\frac{\partial c}{\partial z}\right|_{z=z_\mathrm{b}} = 0 \tag{2.8}$$

where z_t and z_b correspond to the top and bottom boundaries of the bowl (with diameter d_t and d_b, as shown in Figure 2.5). The system of 500 ordinary differential equations is solved in time using the `ode15s` solver in MATLAB with relative and absolute error tolerances set to 0.01% and 1×10^{-4} g/mL. As shown in Figure 2.5, the following initial condition applies:

$$\begin{aligned} \text{For } t &= 0 \text{ and } z_\mathrm{t} \leq z \leq H_\mathrm{T} : c = c_0 = M_1/(\phi V_\mathrm{T}) \\ \text{For } t &= 0 \text{ and } H_\mathrm{T} < z \leq z_\mathrm{b} : c = 0 \end{aligned} \tag{2.9}$$

where H_T and V_T are the thickness and volume of the initial MEG layer, and M_1 is the total mass of MEG calculated on an experiment-by-experiment. The mass of MEG in the top and bottom section of the bowl are computed as follows:

$$m_j(t) = \phi \int_{z_1}^{z_2} c(t,z) A(z) dz$$

where for $j = T$ (top), $z_1 = z_\mathrm{t}$ and $z_2 = H_\mathrm{T}$, while for $j = B$ (bottom), $z_1 = H_\mathrm{T} + \Delta z$ and $z_2 = z_\mathrm{b}$.

2.4.2 Constant Cross-Section

In Chapter 4 the experimental geometry is changed to investigate the effects on convective mixing. A cube and cylinder of similar size to the bowl are selected the exact dimensions will be discussed in later chapters. Unlike the bowl, the cross-sectional area of a cube and

the cylinder is constant over the length of the container and Eq. 2.6 can be simplified as:

$$\frac{\partial c}{\partial t} = \mathscr{D}\left(\frac{\partial^2 c}{\partial z^2}\right) \tag{2.10}$$

After which the equation is discretised as described above and the same boundary conditions applied. The mass is now calculated as follows:

$$m_j(t) = A\phi \int_{z_1}^{z_2} c(t,z)dz$$

A is now a constant and for the cylinder $A = \pi d^2/4$ where d is the diameter and A = H^2 for the cube where H is the height.

2.4.3 Results

The MEG fraction can be plotted for the case of the constant (solid) and changing (dotted) cross-section for the initial MEG layer(red) and the brine layer(blue) and plotted as a function of the as a function of the square root of time, $t^* = \sqrt{t}$ and is shown in Figure 4.2. With the additional term in the changing cross-section case the change of mass is faster than in the constant case. However, at times scales which are relevant to the experiments $0 < t^* < 25$ the curves are similar.

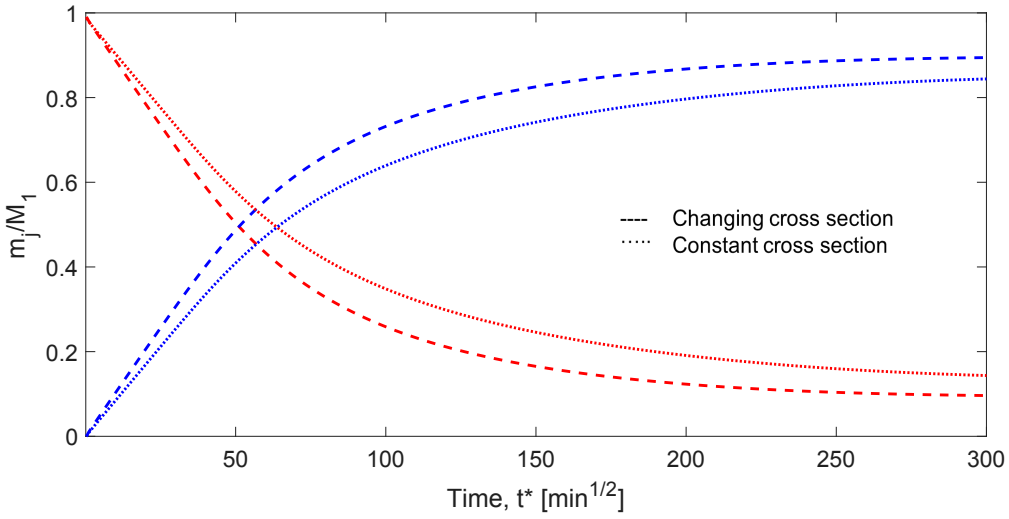

Figure 2.8: Relative mass of MEG dissolved in brine, m_j/M_1, as a function of the square root of time, $t^* = \sqrt{t}$ for purely diffusive case with a changing (dashed) and constant (dotted) cross-section.

Chapter 3

Investigating the Effect of Miscible Fluid Pairs in a Homogeneous Packing

3.1 Introduction

In this Chapter an experimental study is presented of dissolution-driven convection in a three-dimensional porous medium formed from a dense random packing of glass beads. In the first part of the Chapter measurements are made using the model fluid system MEG/water in the regime of Rayleigh numbers, $Ra = 2000 - 5000$. X-ray Computed Tomography is used to image the spatial and temporal evolution of the solute plume non-invasively. The tomograms are used to compute macroscopic quantities including the rate of dissolution and horizontally averaged concentration profiles, and enable the visualisation of the flow patterns that arise upon mixing at a spatial resolution of about 10 mm^3. The latter highlights that under this Ra regime convection becomes truly three-dimensional with the emergence of characteristic patterns that closely resemble the dynamical flow structures produced by high-resolution numerical simulations. We observe that the mixing process evolves systematically through three stages, starting from pure diffusion, followed by convection-dominated and shut-down. A modified diffusion equation is applied to model the convective process with an onset time of convection that compares favourably with literature data and an effective diffusion coefficient that is almost two

orders of magnitude larger than the molecular diffusivity of the solute.

In the second part of the Chapter, MEG is replaced with BEG (butanol and ethylene glycol) in order to investigate the influence of the viscosity of the top fluid. BEG65 has a similar density to MEG59 but the viscosity is 16 times larger, as shown in Chapter 2. It has been well documented that when a less viscous fluid invades a more viscous fluid characteristic fingers are produces depending on the viscosity ratio of the fluids. This is known as a Saffman-Taylor instability [81] and has been widely investigated in the context of oil recovery. In the opposite situation where the invading fluid is more viscous then the resident fluid the front remains stable; this is been referred to as an inverse Saffman Taylor problem [82]. In fact, very few studies have been carried out on this topic of viscous fingering combination with buoyant flow and so this is particular novelty of this thesis.

However, in the case of convective dissolution when using analogue fluid pairs the viscosity ratio maybe impacting the formation of the fingers. Demonstrated in Chapter 2 MEG is 3 times more viscous than brine. Interestingly, in CO_2 storage the CO_2 rich brine will be more viscous than brine and thus the MEG-water case is an accurate representation but in CO_2 EOR the CO_2 rich oil maybe less viscous than the resident oil whilst still being more dense. Therefore it is possible there is an interplay between viscosity fingering and buoyancy flow, this however is only speculation as there are very few studies, if any, of the impact of the viscosity on the process of convective dissolution or more importantly relative viscosities of the analogue fluids. In one paper the suspected influence of the viscosity difference and viscosity mixing is mentioned when using analogue fluids as they present with 'significant viscosity variations' [40]. However, as yet there has not been a follow up study either numerically or experimentally. Here, the aim is to shed some light and show for the first time that an inverse Saffman-Taylor situation could be dampening the formation of the fingers and causing later onset times in the BEG case as compared to the MEG.

Finally in this Chapter, the experimental observations of convective mixing are compared against their numerical counterparts of the purely diffusive scenario which enables the estimation of a non-dimensional convective mass flux in terms of the Sherwood number. We found that the relationship scales linearly to the Ra where $Sh = 0.025Ra$ for the MEG case. This is in agreement with observations from both experimental and numerical studies on solute and thermal convection over the same Ra regime.

3.2 Methanol and Ethylene Glycol

The experimental protocol outlined in Chapter 2 is repeated for experiments with the three different MEG solutions also detailed in Chapter 2 namely MEG55, MEG57 and MEG59 and for each solution two repeats have been completed. Parameters that are specific to each experiment are summarised in Table 3.1 and their estimation is explained in the following section.

Table 3.1: Summary of experiments conducted in this study. The parameters listed in the table have been estimated upon following the procedure described in Chapter 2. M_1 and M_2 are the mass of solution 1 (MEG) and 2 (brine) with estimated uncertainty, σ_{M}; V_{T} and V_{B} are the volumes of the top and bottom sections of the bowl and $\widehat{w}_{\mathrm{B}}(t_{\mathrm{f}})$ is the mass fraction of solute in the bottom section of the bowl at the end of the experiment. For each experiment, $H_{\mathrm{T}} = 2$ cm and $H_{\mathrm{B}} = 13$ cm.

Solution	M_1 [g]	M_2 [g]	σ_{M} [g]	V_{T} [mL]	V_{B} [mL]	$\widehat{w}_{\mathrm{B}}(t_{\mathrm{f}})$
MEG55/brine	88.7	792.4	4.9	242.2	2116	0.112
	97.8	788.7	5.4	267.0	2107	0.124
MEG57/brine	79.4	808.2	5.3	215.2	2159	0.098
	72.4	815.3	6.8	196.1	2178	0.089
MEG59/brine	83.3	799.1	7.9	224.1	2134	0.104
	103.9	784.0	10.2	279.6	2094	0.133

3.2.1 Extent of Dissolution and Mixing Regimes

Figure 3.1 shows the fraction of solute (MEG) dissolved in brine, m_j/M_1, as a function of the square root of time, $t^* = \sqrt{t}$, for the three MEG solutions. The bowl is separated into the volume above the initial interface denoted as'top' and the volume below the initial interface denoted as 'bottom'. For each system, the dissolved amount has been calculated for both top ($j = T$, red symbols) and bottom ($j = B$, blue symbols) sections of the bowl independently, and results are reported for two repeated experiments (empty and filled symbols). Error bars are also shown that have been estimated from the variance of the computed total mass of MEG, $M_1(t) = m_{\mathrm{B}}(t) + m_{\mathrm{T}}(t)$, and are reported as σ_{M} in Table 3.1. In each plot two sets of curves are also shown that represent (i) modified logistic functions fitted to the experimental data (solid curves, see A4) and (ii) the purely diffusive scenario (straight solid lines). The latter are the numerical solutions of the model presented in Chapter 2.

Table 3.2: Macroscopic measures of convective mixing extracted from the experiments carried out in this study. Rayleigh number (Ra), effective diffusion coefficient achieved in the convective regime ($\mathscr{D}_{\text{eff}}$), onset time of convection (t_c) and time of convective shutdown (t_s). The molecular (bulk) diffusion coefficient takes the value $\mathscr{D} = 1 \times 10^{-5}$ cm^2/s. The parameters and their uncertainties have been obtained using standard relationships for weighted linear regression [83].

Solution	Ra	$\mathscr{D}_{\text{eff}}/\mathscr{D}$	t_c [min]	t_s [min]
MEG55/brine	2150	79 ± 7	50 ± 9	363 ± 38
		67 ± 7	57 ± 13	423 ± 54
MEG57/brine	3230	78 ± 9	32 ± 9	314 ± 46
		69 ± 11	21 ± 9	300 ± 58
MEG59/brine	4610	115 ± 22	15 ± 8	190 ± 44
		105 ± 20	19 ± 9	215 ± 49

Overall, the experiments show good reproducibility and they all delineate a behaviour that is characterised by three dissolution regimes, namely (i) diffusive, (ii) convection-dominated and (iii) shut-down. These regimes are associated with a marked change in the slope of the fitted logistic function and, accordingly, in the rate of dissolution. In particular, at early times ($t^* < 1 - 5$ min$^{0.5}$) all the experiments approach the behaviour predicted by a purely diffusive scenario, where the dissolved mass grows in proportion to $\sqrt{\mathscr{D}t}$, with $\mathscr{D}$ being the bulk molecular diffusion coefficient. With the onset of convection, the rate of dissolution increases significantly; notably, a second (pseudo-)diffusive regime is observed, which is denoted in the figure by the black dashed lines with slope proportional to $\sqrt{\mathscr{D}_{\text{eff}}t}$. The effective diffusion coefficient, $\mathscr{D}_{\text{eff}}$, can be readily estimated from the squared ratio of the slopes of these two (linear) regimes (diffusive and pseudo-diffusive); the obtained values are summarised in Table 3.2. For the three systems investigated, the ratio of the effective to the molecular (bulk) diffusion coefficient, $\mathscr{D}_{\text{eff}}/\mathscr{D}$, takes an average value of 73 ± 5 (MEG55), 74 ± 7 (MEG57) and 110 ± 15 (MEG59), corresponding to an enhancement of the rate of dissolution of about two orders of magnitude.

The experimental data confirm the expected positive trend in the onset and subsequent rate of dissolution with increasing Rayleigh number. The time for the onset of the convective regime, t_c, has been estimated by identifying the point at which the experimental measurements departs from the model-predicted diffusive line. For each scenario, this point is denoted in Figure 3.1 by the black circle, which has been obtained upon extrapolation of the trend predicted by the pseudo-diffusive regime back to $m_j/M_1 = 1$; the obtained values are 54 ± 16 min (MEG55), 26 ± 13 min (MEG57) and 17 ± 12 min (MEG59),

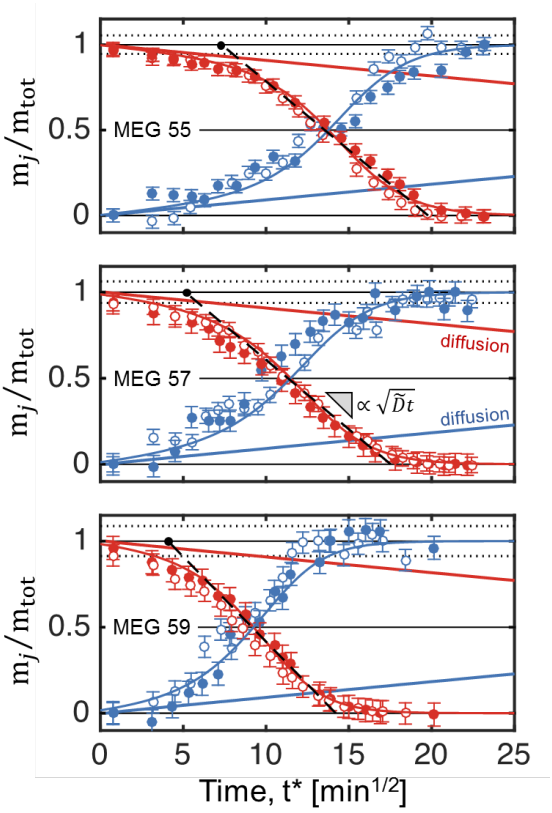

Figure 3.1: Relative mass of MEG dissolved in brine, m_j/M_1, as a function of the square root of time, $t^* = \sqrt{t}$ for experiments conducted with MEG55 (top), MEG57 (centre) and MEG59 (bottom). Two independent sets of experiments are shown for each scenario (filled and empty symbols). Colours refer to observations on the top (red) and bottom (blue) sections of the bowl. In each plot, the two sets of solid curves represent a purely diffusive scenario (straight lines, Eq. 2.7) and modified logistic functions fitted to the experimental data (equations and parameters given in Appendix). The black dashed lines are linear fits applied to the time period where the process of convective mixing attains a pseudo-diffusive regime; the corresponding parameters ($\mathscr{D}_{\text{eff}}$, t_c and t_s are summarised in Table 3.2).

and are additionally plotted in Figure 3.2 as a function of the Rayleigh number, *Ra*. It can be seen that our experimental observations compare favourably with results from numerical studies reported in the literature and summarised in [11], where it is shown that $t_c \sim \text{Ra}^{-2}$. As can be inferred from the figure, the determination of the time for the onset of convection is affected by a significant degree of uncertainty (deviations of up to one order of magnitude are seen among the trends predicted by the numerical simulations). The latter results from the presence of perturbations at the interface, which need to be imposed artificially (in numerical simulations) or are naturally introduced by packing heterogeneities (as it is the case of our experiments). As shown in Figure 3.1, the convective regime is followed by a gradual slow down of the dissolution rate that eventually approaches a value near zero. In our system, this shut-down appears, because of the

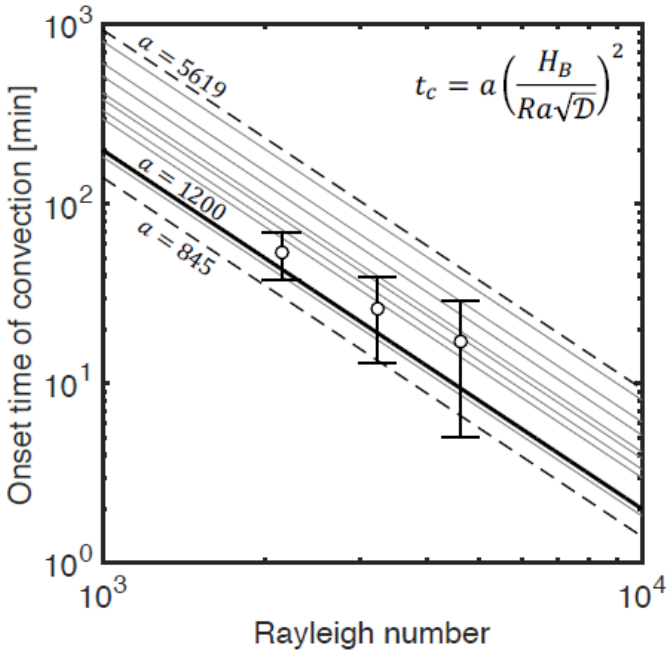

Figure 3.2: Onset-time of convection as a function of the Rayleigh number for the three scenarios investigated in this study (symbols). The lines corresponds to a correlation of the form $t_c \sim \mathrm{Ra}^{-2}$ (equation given on the plot) that has been adopted in various numerical studies summarised in [11] and that use different values of the prefactor a. Other parameters include the height of the domain, $H_B = 10$ cm and the molecular (bulk) diffusion coefficient, $\mathscr{D} = 1 \times 10^{-5}$ cm^2/s.

depletion of the MEG plume; accordingly, because of the trend in the rate of dissolution described above, the time to attain convective shutdown (t_s in Table 3.2) decreases with increasing Ra number, i.e. $t_s = 393 \pm 66$ min (MEG55), 307 ± 74 min (MEG57) and 202 ± 66 min (MEG59).

Because it involves convection, the dissolution process is affected by hydrodynamic dispersion, the extent of which depends on the pore fluid velocity, $\mathrm{v} = k\Delta\rho g/\mu_2\phi$ and is an estimate of the typical finger velocity. For the longitudinal dispersion coefficient, $\mathrm{D}_L \sim Pe$, with $Pe = \mathrm{vl}/\mathcal{D}$ being the Peclet number and $\mathrm{l} = \mathrm{dP}$ the characteristic length-scale. Transverse dispersion tends to diminish the amplitude of the concentration gradients in the system [76] and is therefore expected to slow down the dissolution process. It has also been reported the accounting for dispersion in numerical simulations can reduce the onset time of convection of up to two orders of magnitude [77]. One the one hand, there seems to be some general consensus that dispersion effects are small on both the pattern and time-scale of the density-driven dissolution process [7, 35, 84]. On the other hand, dispersion may be significant locally [31], where density differences are large ($\Delta\rho = \Delta\rho_{max}$) and where$\mathcal{O}(Pe) \sim 10$ in our system. If any hydrodynamic dispersion is present in

the experiments reported here, this is accounted for in the value of the estimated effective diffusion coefficient, D_{eff}, that lumps diffusive and dispersive processes together.

3.2.2 Horizontally Averaged Concentration Profiles

In Figure 3.3 are presented vertical profiles of the mass fraction of solute, w, at various times and for the three systems investigated, namely MEG55, MEG57 and MEG59. The profiles have been computed upon using CT numbers in Eq. 2.4 that represent the average of all voxels in each 2 mm-thick horizontal section of the bowl. To facilitate comparison among observations with different MEG solutions (and, accordingly, Ra numbers), profiles are shown in the figure for CT scans that have been acquired at similar values of the dimensionless time, $\tau = \mathscr{D}_{\text{eff}} t/H_{\text{B}}^2 \approx 0.01 - 0.6$. Results are also shown in the rightmost panel of the figure for the purely diffusive case and for which $\tau = \mathscr{D} t/H_{\text{B}}^2$. In each plot, the black solid line represents the position of the interface at the start of the experiment. The experimental results obtained for different Rayleigh numbers show a significant degree of similarity in terms of both the temporal and spatial evolution of the dissolved plume: for $\tau < 0.08$ (red profiles), the MEG/brine interface recedes gradually, while the solute plume moves downwards in the bowl, because of its larger density as compared to fresh brine; at $\tau \approx 0.1$, the pure MEG solution has almost completely dissolved and for $\tau > 0.1$ the solute plume begins accumulating at the bottom of the bowl (blue profiles). Notably, this results in the reversal of the concentration gradient along the bowl, with the mass fraction of MEG in brine now increasing with the distance from the top. At the end of the experiment ($\tau \approx 0.7$), the mass fraction of MEG increases from $w \approx 0$ at $z = 0$ cm to $w \approx 0.25$ at $z = 13$ cm. This late-time distribution of the solute differs from the corresponding profile predicted by the model that describes a purely diffusive scenario (rightmost panel), where -as expected- the solute reaches a uniform distribution along the entire length of the bowl. In other words, convection precludes a perfect dilution of the plume as it moves downwards and the resulting (stable) density gradient once convection ceases is such that diffusion remains the only mechanism to achieve complete mixing. Two additional observations arise from the comparison between the experiment and the diffusion model. First, because density is constant in the model and diffusion is ubiquitous, the MEG/brine interface doesn't show the characteristic receding behaviour observed in the experiments, where $\rho_1 < \rho(w)$. In this context, despite being fully miscible with

brine, the lower density of MEG acts towards stabilising the interface, while maintaining a much steeper concentration gradient across it. Second, prior to the cessation of convection the behaviour of the solute plume underneath the interface is indeed similar to the one observed in the diffusion model, thus supporting the findings discussed above on the establishment of a pseudo-diffusive regime in the experiments.

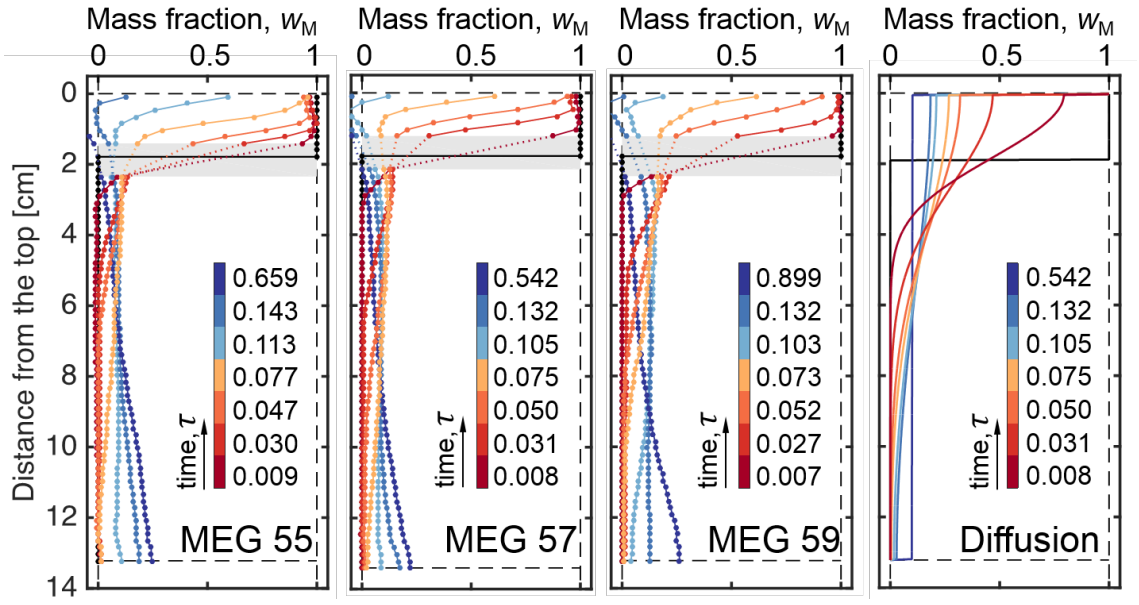

Figure 3.3: Horizontally-averaged profiles of the MEG mass fraction, w, as a function of the distance from the top of the bowl, z. Results are shown for experiments carried out with the three MEG solutions (from left to right: MEG55, MEG57 and MEG59), while the rightmost panel shows predictions from a model describing the purely diffusive scenario described in Chapter 2. For each scenario, profiles are shown at different values of the dimensionless time, $\tau = \mathscr{D}_{\text{eff}} t / H_{\text{B}}^2$ ($\mathscr{D}_{\text{eff}} = \mathscr{D}$ for pure diffusion), while the black solid line denotes the initial position of the interface. The grey-shaded area in the plots with experimental observations represents a region where image noise precludes a reliable estimate of the MEG mass fraction.

3.2.3 Three-Dimensional Imaging and Convective Patterns

Figure 3.4 shows three-dimensional reconstructions of the bowl at various times for the experiments with MEG55 (top row), MEG57 (middle row) and MEG59 (bottom row). The solute mass fraction, w, has been calculated using Eq. 2.4 and the dimensionless time, τ, is again chosen to facilitate the analysis and comparison of experiments conducted at different Rayleigh numbers ($\tau \approx 0.008 - 0.17$). In particular, the following regimes are identified from the 3D images: at early times ($\tau < 0.01$, first column), a large number of small-scale finger projections ($\mathcal{O}(l) \sim 1$ cm) are seen just underneath the MEG/brine

interface; upon further dissolution ($0.01 < \tau < 0.1$, columns 2-4), the MEG layer continues to retract and the fingers continue to grow until they reach the bottom of the bowl ($\mathcal{O}(l) \sim 10$ cm). Closer inspection of the images is evidence that the mass fraction of MEG vary considerably among the different finger projections reaching values as high as $w = 0.6 - 0.7$ in the centre of some of the fingers. By the time the MEG layer has completely dissolved ($\tau > 0.15$, last column), the plume has reached the bottom of the bowl, where the solute accumulates. At this stage of the dissolution process, although a concentration gradient is still present, the associated density gradient is such that the system is stable and and further mixing can be achieved only by diffusion (see also one-dimensional profiles shown in Figure 3.3). We note that the regimes just described are observed in each experiment conducted in this study and their dynamics are very similar when the dimensionless time τ is considered. Accordingly, the 3D maps shown in Figure 3.4 evidence a striking similarity in terms of the number of fingers and of their propagation length. These observations provide further support to the existence of a pseudo-diffusive regime throughout a large portion of the dissolution process with a characteristic time-scale $\tau = \mathscr{D}t/H_{\mathrm{B}}^2$. . In agreement with previous studies on density-driven convection (e.g., [7]), we also observe that the number of fingers increases with Ra.

To discuss more in detail the temporal evolution of the characteristic spatial patterns that are formed throughout the dissolution process, Figure 3.5 show 2D horizontal cross-sections of the bowl at three vertical positions, namely $z = 2.4$ cm, $z = 7.1$ cm and $z = 11.8$ cm for the experiment conducted with MEG59 (in each row, time progresses from left to right). At early times and just underneath the interface ($z = 2.4$ cm, top row), a myriad of small protrusions are formed across the entire interface, most of which are still disconnected. With increasing time, the MEG concentration within the protrusions increases and bridges are formed, thus creating a structure that is largely connected. A similar behaviour is observed at a larger distance from the interface ($z = 7.1$ cm, middle row), although the numbers of fingers (at early times) and connected structures (at later times) is now significantly reduced. This decrease is due to the merging of fingers as they migrate downwards and create a coarser maze structure, where bridges of high solute concentration ($w \approx 0.2 - 0.4$) are separated by regions of near-zero concentration. Again, these structures are strikingly similar to those reported in one of the earliest investigations of convective mixing in three-dimensions using MRI [52]. The appearance

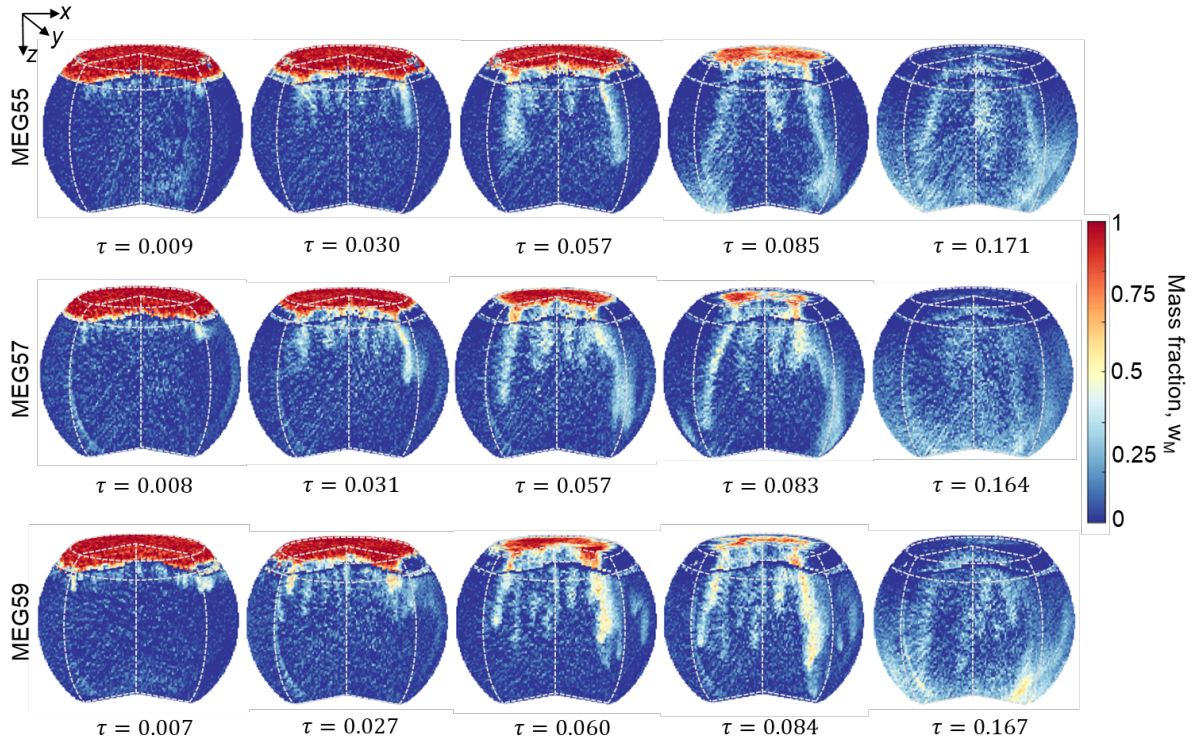

Figure 3.4: Three-dimensional reconstructions of the convective mixing process within the bowl, as obtained from X-ray CT scans. Images are shown in terms of solute (MEG) mass fraction, $w_i(t)$, for three systems, namely MEG55 (top row), MEG57 (middle row) and MEG59 (bottom row), as a function of the dimensionless time, $\tau = \mathscr{D}t/H_B^2$. Voxel dimensions are: $(2.3 \times 2.3 \times 2)$ mm^3.

at "early" times ($t^* \approx 11.5\ min^{1/2}$) of islands of high concentration near the bottom of the bowl ($z = 11.8$ cm, bottom row) is evidence that the columnar fingers can migrate downwards rather independently; notably, the cross-sectional area of these islands is considerably larger than their counterparts that originate higher up in the bowl due to the action of transverse dispersion during convection. This is also supported by the characteristic gradual discolouring of the islands that reflects the presence of an outward gradient in solute concentration. The overall increase in concentration across the entire cross-section at later times is due to the accumulation of solute on the bottom of the bowl and the cessation of the convective process. It is worth pointing out that the emergence of the multidimensional structures just described is inherently not possible in 2D systems (e.g., Hele-Shaw cells) and demonstrates the three-dimensional nature of the convective dissolution process. Because of the size of the system considered ($V \approx 2500$ cm^3) and the high resolution of the images ($V_{vox} \approx 0.010$ cm^3), the observations presented here are thus first of its kind and demonstrate the ability of X-ray CT to provide quantitative information on the temporal and spatial evolution of the solute plume during density

driven convection in opaque porous media.

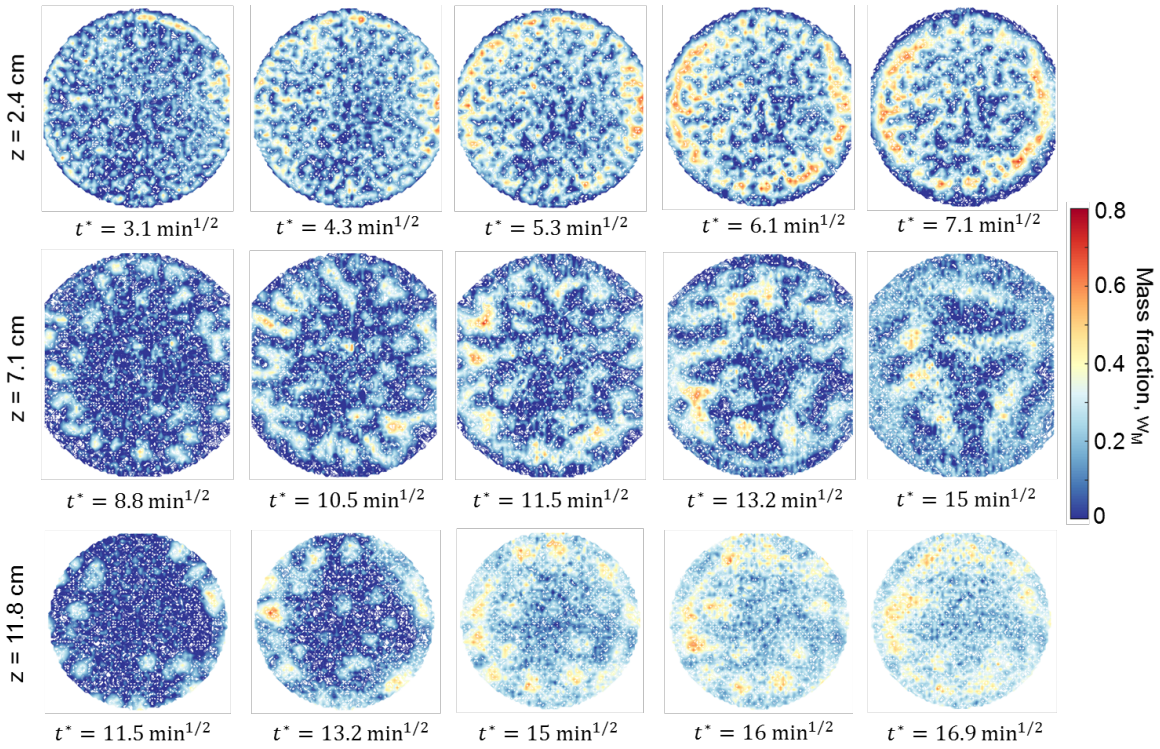

Figure 3.5: Two-dimensional horizontal flow patterns of convective mixing within the bow for the experiment with MEG59. The horizontal cross-sections represent three distinct positions within the bowl, namely $z = 2.4$ cm (top row), $z = 7.1$ cm (middle row) and $z = 11.8$ cm (bottom row). In each row, time, $t^* = \sqrt{t}$, increases from left to right. Voxel dimensions are $(2.3 \times 2.3 \times 2)$ mm^3 and the images are presented as contour lines of constant MEG mass fraction, $w_i(t)$.

3.2.4 Rate of Convective Dissolution and Mass Flux

The rate of dissolution is intuitively a key measure to quantify the enhancement of mixing (or lack thereof) produced by the convective process that originates from density instabilities in the system. Of particular interest is its comparison against the rate of dissolution that results from the action of diffusion and that relies solely on the presence of concentration gradients in the same system. This comparison is shown in Figure 3.6, where the dissolution rate observed in the experiments conducted with the three MEG solutions is plotted as a function of time together with the rate predicted by the diffusion model described in Chapter 2. With reference to the results presented in Section 3.2.1 (Figure 3.1), the dissolution rate is defined as,

$$r = -\frac{M_{\mathrm{R}}}{M_1}\frac{dm_{\mathrm{T}}}{dt} \tag{3.1}$$

where m_T and M_1 are the current and initial mass of MEG in the top section of the bowl, while $M_R = 100$ g is a reference mass used to re-establish dimensions and to enable comparison between the experiments where a different amount of MEG was used (see Table 3.1). The three solid curves obtained for the MEG solutions have been obtained by differentiating the logistic functions fitted to the experimental data. To account for the uncertainty of the experimental observations, 300 additional realisations of the fitting-differentiation exercise have been carried out by randomly varying the experimental data within the error bars shown in Figure 3.1; these additional curves are also shown in the figure and create the colour-shaded regions around the mean curve of each system. It can be seen that all curves initially follow the trend predicted by the diffusion model (black solid line) and that they gradually diverge from it as time increases. In particular, the dissolution rate increases and reaches a maximum before falling off rapidly at late times. We acknowledge that this behaviour may not be ascribed solely to the effect of varying Ra, because of the effects introduced by the characteristic shape of the $\rho(w)$ curve of the three fluid pairs [40]. Nevertheless, the observed trend closely reflects the attainment of the three regimes discussed in Section 3.2.1, namely diffusive, convection-dominated (or pseudo-diffusive, with onset-time t_c shown by the crosses) and shut-down. As expected, with increasing Rayleigh number the experimental curves depart sooner from the diffusive regime and they also reach a larger (and earlier) maximum dissolution rate, r_{max}. For the three MEG systems, the obtained estimates are $r_{max} = 0.37 \pm 0.06$ g/min (MEG55, at 186 min), $r_{max} = 0.43 \pm 0.06$ g/min (MEG57 at 124 min) and $r_{max} = 0.61 \pm 0.11$ g/min (MEG59 at 74 min). Interestingly, in all scenarios the time to reach maximum dissolution rates is about four times larger than the time required for the onset of convection, i.e. $t(r_{max}) \approx 4t_c$. The black circles in Figure 3.6 represent the rates of dissolution achieved by diffusion at equivalent (absolute) time and take values $r_{\mathscr{D}} = 0.033$ g/min (MEG55), $r_{\mathscr{D}} = 0.040$ g/min (MEG57) and $r_{\mathscr{D}} = 0.052$ g/min (MEG59), respectively. We note that these dissolution rates are approximately one order of magnitude smaller than the corresponding values achieved in the presence of convection.

We also note that by using a fixed boundary (i.e. the original interface) in our calculations the amount of MEG dissolved over time is underestimated. Accordingly, one could refer to a rate of MEG removal, rather than dissolution. This rate of removal combines two contributions: the rate of change in mass of buoyant solution (which is, effectively, the rate

of dissolution) and the rate of change in the mass of non-buoyant solution ($w < w_0$). In our experiments, the latter is expected to be significantly smaller than the former, because, while some dissolved MEG does accumulate (temporarily) above the initial interface, a given amount also leaves the volume by convection. This last process is quite fast and effectively minimizes the accumulation of solute above the interface. Accordingly, in our experiments the rate of MEG removal approaches the rate of dissolution. The latter is estimated with an uncertainty in the order of 15-20 %, which we consider to be larger than any error introduced by using a fixed boundary in the calculations.

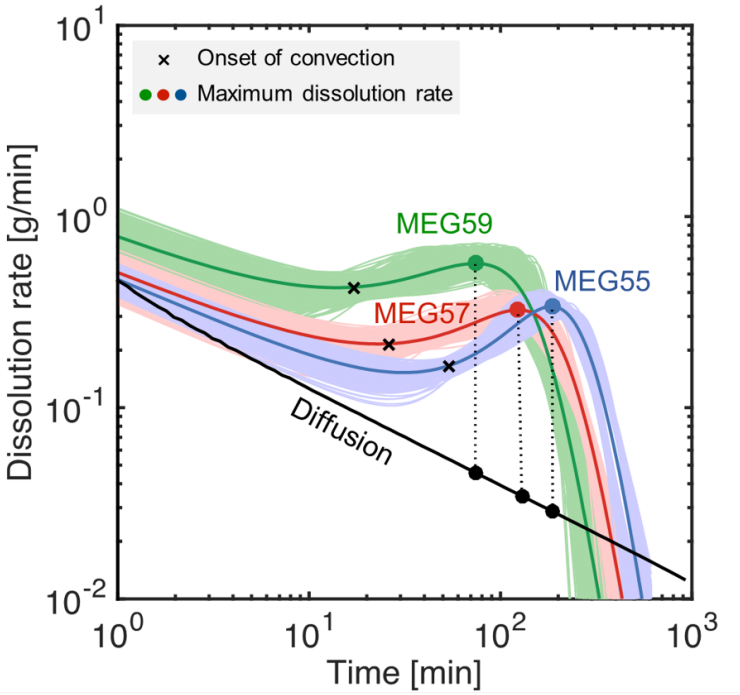

Figure 3.6: Rate of dissolution as a function of time for the experiments conducted with MEG55 (blue), MEG57 (red) and MEG(59) (green). The solid coloured lines are obtained upon differentiating the modified logistic function fitted to the experimental data (Figure 3.1), while the solid black line is the numerical solution of the purely diffusive scenario. For each MEG scenario, the colour-shaded region represents the ensemble of numerical realisations (300) conducted to account for the uncertainty of the raw experimental data. The cross symbols are the rate of dissolution at the time of the onset of convection (estimated from Figure 3.1), while the circles represent the time at which the maximum rate of dissolution is attained.

The Sherwood number, *Sh*, represents a non-dimensional measure of the convective mass flux and can be estimated from the ratio of the maximum convective dissolution rate computed above to the corresponding value in the presence of diffusion alone, while

accounting for the appropriate length scales, i.e.

$$Sh = \frac{l_{\mathrm{H}}}{l_{\mathscr{D}}} \frac{(dm_{\mathrm{T}}/dt)_H}{(dm_{\mathrm{T}}/dt)_{\mathscr{D}}} \tag{3.2}$$

where $l_{\mathrm{H}} = 10$ cm $\approx H_{\mathrm{B}}$ is the characteristic length scale of convective mixing, while $l_{\mathscr{D}}$ is the corresponding value associated with the diffusive process. In this study, the latter has been chosen to be the thickness of the diffusive boundary layer at the given time (threshold set to 5% deviation from the baseline) and take the value $l_{\mathscr{D}} \approx 1 - 2$ cm depending on the system considered. The corresponding estimates of the Sherwood number are therefore $Sh = 57 \pm 10$ (MEG55), $Sh = 66 \pm 9$ (MEG57) and $Sh = 96 \pm 17$ (MEG59). As discussed below, these estimates are in close agreement with the corresponding values obtained from the ratio of the effective-to-molecular diffusion coefficients presented in Table 3.2.

We also note that we do not observe in Figure 3.6 a clear regime of constant dissolution rate, in agreement with other experimental observations [56]. The reasons for this are twofold; first, results from numerical simulations [8] suggest that for the range of Rayleigh number considered in this study ($\mathrm{Ra} = 2150 - 4610$) the constant-flux regime is expected to be relatively short. Secondly, the chosen boundary condition in our experiments (constant volume of solute as opposed to a constant concentration of solute adopted in most numerical studies) is such that the limited amount of MEG solution precludes the attainment of a regime with constant dissolution rate prior to the depletion of the MEG layer. In this context, we note that both initial conditions and Ra will play an important role in controlling the dissolution process and the degree of mixing that can be achieved.

3.3 Butanol and Ethylene Glycol

Next we replace methanol with tertiary butanol to investigate the effects of changing the viscosity ratio between the top and bottom fluids. In this case all other parameters such as the permeability and height of the brine are kept the same and the same experimental procedure is followed as outlined previously. Only one BEG ratio (BEG65) is investigated in the following section and can be most closely compared to the MEG59. The density difference is comparable and the cross over point into the unstable regime is also similar, the details of the mixing behaviour can be found in the previous Chapter. As for the

analysis, as before the geometry is split into two parts which represents the domain above and below the initial interface and further analysis performed in order to determine key macroscopic properties.

3.3.1 Extent of Dissolution and Mixing Regimes

Two repeated experiments were performed with the BEG-water system. As before the mass and volumes in the two sections was computed and is presented in Table 3.3 along with the variance of the mass and the final mass fraction of BEG in the system.

Table 3.3: Summary of experiments conducted in this study. The parameters listed in the table have been estimated upon following the procedure described in Chapter 2. M_1 and M_2 are the mass of solution 1 (BEG) and 2 (brine) with estimated uncertainty, σ_{M}; V_{T} and V_{B} are the volumes of the top and bottom sections of the bowl and $\widehat{w}_{\mathrm{B}}(t_{\mathrm{f}})$ is the mass fraction of solute in the bottom section of the bowl at the end of the experiment. For each experiment, $H_{\mathrm{T}} = 2$ cm and $H_{\mathrm{B}} = 13$ cm.

Solution	M_1 [g]	M_2 [g]	σ_{M} [g]	V_{T} [mL]	V_{B} [mL]	$\widehat{w}_{\mathrm{B}}(t_{\mathrm{f}})$
BEG65 - 1	87.2	733.5	7.9	232.7	2109	0.113
BEG65 - 2	101.39	811.61	10.2	269.8	2118	0.125

The mass and volume of each sub-domain show some variance but these values are still within the range seen previously in the MEG experiments.

The BEG fraction dissolved in brine, m_j/M_1, as a function of the square root of time, $t^* = \sqrt{t}$ for each of the sub domains, top ($j = T$, red symbols) and bottom ($j = B$, blue symbols) is computed and plotted in Figure 3.7 along with the MEG59 case for comparison. Here, MEG59 is chosen for the comparison fluid as it the maximum density difference is the closest match to the BEG system and from Table 3.4 the Ra is almost equivalent. Again the modified logistics function is fitted and the diffusion curve is plotted. There is a very good agreement between the two BEG experiments, they present with a similar trend as the MEG that is characterised by diffusive, convection and shut-down. However these regimes are noticeably slower for the BEG system and much more comparable to the MEG55 system. As before it is possible to extract key parameters from this curve such as the effective diffusion coefficient the onset of convection and the shut-down time; these values are summarised in Table 3.4, here is included the averaged data for each of the MEG experiments for ease of comparison.

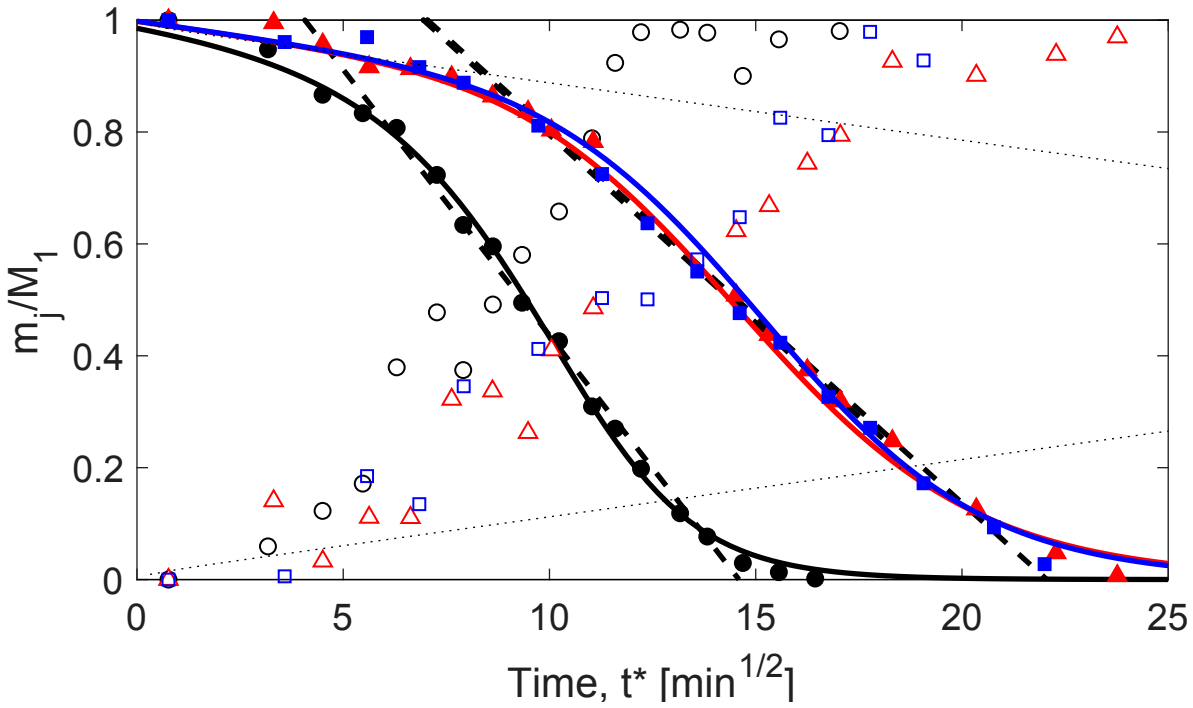

Figure 3.7: Relative mass of BEG dissolved in brine, m_j/M_1, as a function of the square root of time, $t^* = \sqrt{t}$ for experiments conducted with BEG65-1 (blue), BEG65-2 (red) and MEG59 (black). Filled and empty symbols refer to observations on the top (filled) and bottom (empty) sections of the bowl. In each plot, the two sets of solid curves represent a purely diffusive scenario (straight lines, Eq. 2.7) and modified logistic functions fitted to the experimental data (equations and parameters given in Appendix). The black dashed lines are linear fits applied to the time period where the process of convective mixing attains a pseudo-diffusive regime; the corresponding parameters ($\mathscr{D}_{\text{eff}}$, t_c and t_s are summarised in Table 3.2).

The onset time for the BEG65 is 49±10min which is much closer to the MEG55 (54±11min) and than the MEG59 (17±8min). However, the BEG65 does not follow the behaviour of the MEG55 at later times, the shut down time for BEG65(482±51min) is almost 100 min slower than the MEG55(393±46min) and 200 min slower than the MEG59(202±47min). Interestingly, if we look at the ratio between the onset and shut down times of the MEG59 and BEG65 case we observe the onset time for $t_c(BEG65) = 2.88t_c(MEG59)$ and the shutdown time for $t_s(BEG65) = 2.4t_s(MEG59)$. This indicates that viscosity ratio is systematically delaying convection but not the rate of convection. It can be observed that the $\mathscr{D}_{\text{eff}}/\mathscr{D}$ for the BEG65 which is an average of 78±14 fits the positive Ra - $\mathscr{D}_{\text{eff}}/\mathscr{D}$ trend. However further explanation is require to understand the trends in the onset and shutdown times which appear not no longer be a function of Ra.

Traditionally, the most important factor should be the density difference of the system, however in this model fluid system there are other factors which are influencing the process such as the cross over point between the stable and unstable regime i.e. the mass fraction

Table 3.4: Macroscopic measures of convective mixing extracted from the experiments carried out in this study. Rayleigh number (Ra), effective diffusion coefficient achieved in the convective regime ($\mathscr{D}_{\text{eff}}$), onset time of convection (t_{c}) and time of convective shut down (t_{s}). The molecular (bulk) diffusion coefficient takes the value $\mathscr{D} = 1 \times 10^{-5}$ cm^2/s. The parameters and their uncertainties have been obtained using standard relationships for weighted linear regression [83].

Solution	Ra	$\mathscr{D}_{\text{eff}}/\mathscr{D}$	t_{c} [min]	t_{s} [min]
BEG65 - 1	3900	79 ± 11	50 ± 8	487 ± 44
BEG65 - 2	3900	78 ± 16	48 ± 12	477 ± 58
MEG55/brine	2150	73 ± 7	54 ± 11	393 ± 46
MEG57/brine	3230	73 ± 10	26 ± 9	307 ± 52
MEG59/brine	4610	110 ± 21	17 ± 8	202 ± 47

at which the fluid mixture becomes more dense than the brine layer. This is important as it will determine how long it takes for a sufficiently dense boundary layer to accumulate and the subsequent maximal difference to provide the driving force which should set the rate of dissolution. In this case the cross over point is similar for the MEG59 and the BEG65 and so is the maximal density difference, therefore, it should follow that this process would present with similar behaviours. As this is not the case, this results suggest there is another factor which is slowing down the process and increasing the onset time. One potential reason for this is the substantially larger viscosity difference between the BEG and NaCl(aq) compared to the MEG and NaCl which is 16 times larger as compared to 3 times. As previously mentioned when a more viscous fluid invades a less viscous fluid the front is inherently stable. In Figure 3.8 is shown the horizontal reconstructions of the BEG experiment at various locations in the bowl similar to Figure 3.5 for the MEG case. Interestingly, there are significant differences between the structures that form in the two cases. It is immediately obvious that the fingers in the BEG case are much less well defined as there are no patches of high concentration nor, in fact, isolated islands which would indicate independent finger growth. From the early times $t^* = 5.6min^{1/2}$ the fingers have merged into large connected structures. One explanation is that as the fingers begin to form the stabilisation of the viscosity ratio causes fewer larger fingers to form that can merge earlier. Moving down the bowl at z = 7.1 cm a ring structure has formed and dominates throughout the course of the experiment. Unfortunately, at z = 11.8 cm there are many image artefacts as a result of beam hardening at the edges of the bowl and so the tips of the fingers can not be identified at the outside edge of the geometry. The artefacts create artificially large fingers where the concentration gradients are not sharp.

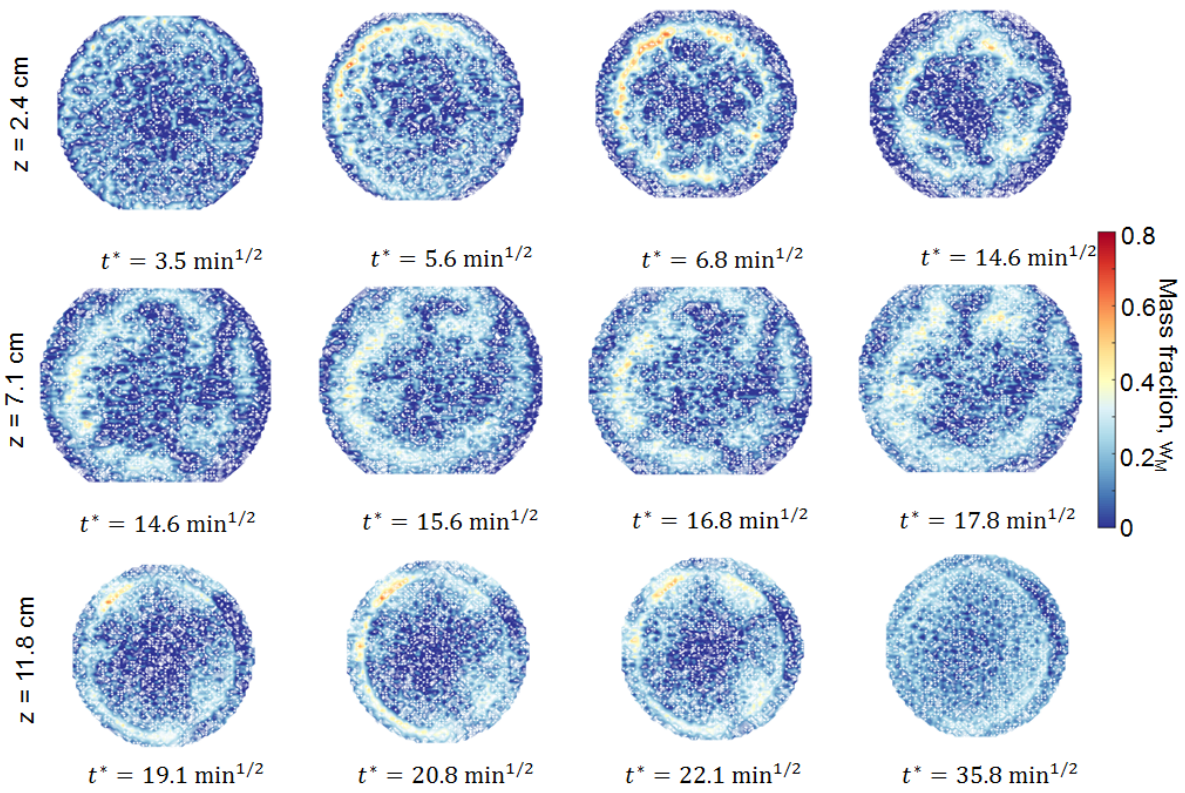

Figure 3.8: Two-dimensional horizontal flow patterns of convective mixing within the bow for the experiment with BEG65. The horizontal cross-sections represent three distinct positions within the bowl, namely $z = 2.4$ cm (top row), $z = 7.1$ cm (middle row) and $z = 11.8$ cm (bottom row). In each row, time, $t^* = \sqrt{t}$, increases from left to right. Voxel dimensions are $(2.3 \times 2.3 \times 2)$ mm^3 and the images are presented as contour lines of constant BEG mass fraction, $w_i(t)$.

In general the fingers and are moving slower in the BEG65 case compared to the MEG59, thus there is more time for lateral mixing and this would explain why the fingers are less well defined. However, these reconstructions also indicate that the early time connected behaviour dictates the later structures which are significantly different between the MEG and the BEG and can be attributed to the viscosity contrast between the fluids.

3.3.2 Rate of Convective Dissolution

The rate of convective dissolution has been calculated in the same manner as described in Section 3.2.1 and plotted in Figure 3.7 as a function of time and is compared to the purely diffusive case for the BEG65 case and the MEG59 fluid system. It can be noted here that there is excellent agreement between the the curves for the two BEG65 experiments. As observed before, the curves initially follow the trend predicted by the diffusion model until it reaches a maximum $r_{\max} = 0.29 \pm 0.06$ g/min (BEG65-1, at

190 min), $r_{\max} = 0.30 \pm 0.07$ g/min (BEG65-2 at 180 min) before rapidly decreasing at late times. However, interestingly the time for the maximum flux remains four times the time required for onset which is the same as reported for the MEG system. This suggests that it is only the onset of the process which is affected by the viscosity stabilisation and not the speed of the resulting convection.

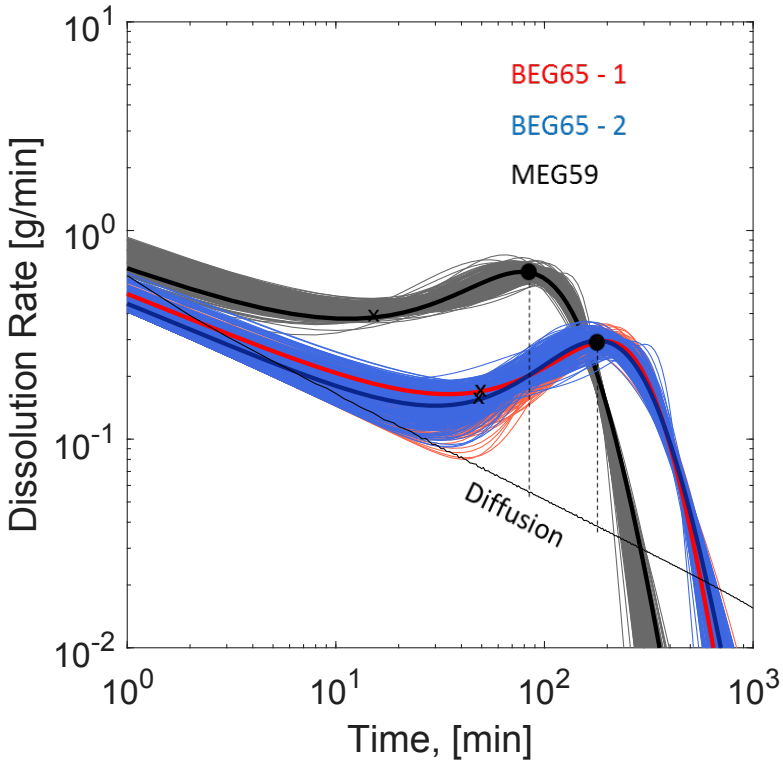

Figure 3.9: Rate of dissolution as a function of time for the experiments conducted with BEG65-1 (blue), BEG65-2 (red) and MEG(59) (black). The solid coloured lines are obtained upon differentiating the modified logistic function fitted to the experimental data (Figure 3.1), while the solid black line is the numerical solution of the purely diffusive scenario. For each MEG scenario, the colour-shaded region represents the ensemble of numerical realisations (300) conducted to account for the uncertainty of the raw experimental data. The cross symbols are the rate of dissolution at the time of the onset of convection (estimated from Figure 3.1), while the circles represent the time at which the maximum rate of dissolution is attained.

Similarly, the Sherwood number allows for a quantitative comparison the maximum flux and for the BEG system this is $Sh = 78 \pm 17$ and $Sh = 77 \pm 18$ respectively. These values are slightly lower than the MEG59 case but the Rayleigh number also slightly lower so both MEG and BEG experiments fit well into the positive trend between $Sh - Ra$ as observed in Figure 3.10. From this a relationship between Ra and Sh can be extracted where $Sh = 0.021Ra$. This relationship between Sherwood and Rayleigh will be discussed further in the following section.

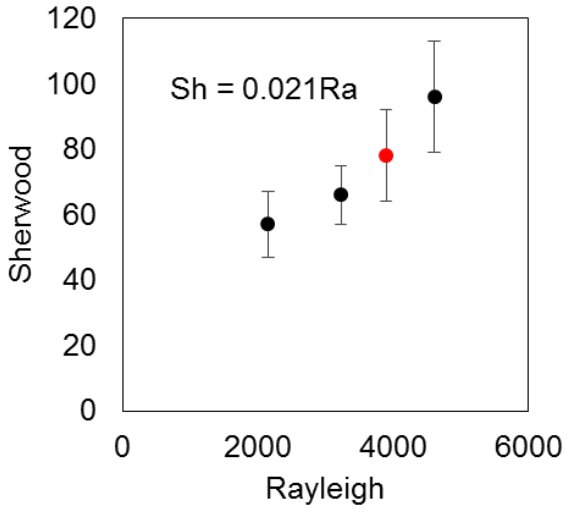

Figure 3.10: Sherwood number, *Sh* as a function of the Rayleigh number, *Ra*. Results from MEG study are reported (black symbols) and the BEG study (red symbol) along with the equation for a linear trend.

3.4 Impact on Geological Carbon Storage

Observations of density-driven convection are often represented in the form of *Sh* vs. *Ra* plots aimed at identifying scaling laws that can be used to relate laboratory observations to field settings. The use of these dimensionless numbers is also needed as a means to compare observations from laboratory studies using different fluid pairs and geometries (e.g., 2D vs. 3D).

In the final section of this Chapter the results are collated from the MEG experiments only and compared to the reported scaling from the literature. Although from the previous figure it appears that the BEG experiments fit along with the MEG scaling in this case, as there is only 1 data point a more thorough study would be needed to validate this claim. Therefore this point is omitted for the next comparison.

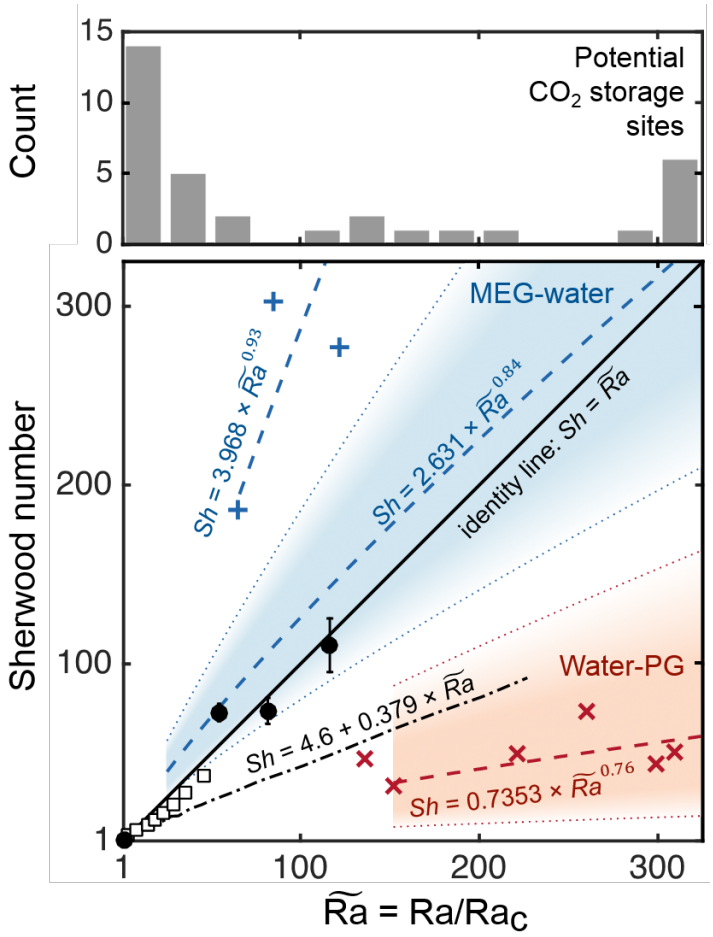

Figure 3.11: Convective mass flux plotted in terms of Sherwood number, Sh as a function of the Rayleigh number, Ra. Results from this study are reported as two sets of data that differ in the way Sh was calculated, namely as the ratio of effective-to-molecular diffusion coefficients (black filled circles, Table 3.2) or as the scaled ratio of the maximum dissolution rates (empty symbols, Eq. 3.2). Data from the literature include measurements using the MEG/brine system on 3D packings (+) [76] and with water/PG in a Hele-Shaw cell (x) [31, 37]. $Sh - Ra$ correlations reported in those studies are plotted as dashed lines (equations given in the figure) and the colour-shaded regions represent the uncertainties in the given parameters [21, 31]. Observations from thermal convection in three-dimensional porous media are also plotted and include results from both experiments (squares, [49]) and numerical simulations (dash-dot line, [74]). The bar chart represents the sorting of 38 aquifers around the world according to the expected Rayleigh number.

In Figure 3.11, we attempt this comparison by presenting the results from this study (circles) together with a selection of data and correlations found in the literature (details given in the figure caption). In the figure, the Rayleigh number has been normalised by its critical value, Ra_c, defined as the Ra value for which Sh (or Nu in heat transfer studies) departs from the value 1 [85]. It has been shown by numerous experimental studies that for convective flow to occur in a porous medium, $Ra > Ra_c = 4\pi^2 \approx 40$ [86]. We also

purposely focus here on the range $\widetilde{Ra} = Ra/Ra_c = 1 - 300$ ($Ra = 40 - 12000$), as this is the regime that is more likely to be expected at depth in potential geologic carbon sequestration sites [16], should the process of convective dissolution occur. We provide further support to this last observation with the bar chart also shown in Figure 3.11 where data from 38 aquifers around the world are sorted according to the expected Rayleigh number. These include 11 major saline aquifers in the United States ($\widetilde{Ra} \sim 1 - 100$, 21 reservoirs in total compiled in [17]), 13 injection sites in the Alberta Basin ($\widetilde{Ra} \sim 1 - 10$) [25]) and the Sleipner site in the North Sea ($\widetilde{Ra} \sim 100 - 1000$, 4 cases depending on the assumed pressure/temperature conditions [12]). While these estimates must be used with some precaution due to the intrinsic difficulty in estimating suitable mean permeabilities and dimensions in heterogeneous reservoirs, the perception is that the condition $\widetilde{Ra} < 100$ ($Ra < 4000$) may be typical in geologic reservoirs.

The data plotted in Figure 3.11 reveal two aspects. First, the available data set is still quite scarce, particularly for $\mathcal{O}(Ra) \sim 1000$. A significant body of literature exist on observations at low Ra values (Ra < 1000, corresponding to $\widetilde{Ra} < 25$ in Figure 3.11), including early studies on thermal convection in porous media (see a collection of more than 100 data points in [20]) and more recent ones on dissolution-driven convection [56, 54]. Others have focused on the high Rayleigh number regime ($\mathcal{O}(Ra) \sim 10^4 - 10^6$) [21, 19, 31, 37, 38, 39] and their observations fall outside the bounds of Figure 3.11. Second, there is a significant degree of scatter among the reported results, which may be due to the use of 2D vs. 3D geometries, as well as of different model fluids. As discussed in the following, both aspects contribute to additional uncertainty on the fundamental behaviour of the dissolution flux and its dependence on the system parameters, such as the Rayleigh number.

The experiments carried out in the present study (circles) are well within the range expected in potential CO_2 storage sites lie near the identity line, suggesting that in this regime the dissolution flux increases linearly with Ra as $Sh = \alpha Ra$ with $\alpha \approx 1$. However, they disagree considerably with results reported on a supposedly similar experimental system, i.e. MEG/brine in a packed bed imaged by X-ray CT, for which a significantly larger dissolution has been reported ($\alpha \approx 4$, blue crosses in the figure) [76]. We attribute this differences to the distinct shape of the density-concentration curve, in particular with the position of the maximum and cross-over points ($w^{\max}$ and w^0 in Figure 2.2),

which in [76] are shifted towards larger MEG concentration values ($w^{\max} \approx 0.6$ and $w^0 > 0.9$). This further implies that the range of concentration values over which the MEG solution is no longer buoyant is wider and mixing rate is thus enhanced. This pattern has been quantitatively demonstrated by means of numerical simulations [40]. It may not be surprising therefore that experimental data acquired on a different model fluid pair [31, 37], namely propylene glycol (PG) and water (red crosses in the figure), lie on the opposite corner of the diagram and suggest that the dissolution flux is significantly smaller (3-4 times when compared to our data at $\widetilde{Ra} = 115$). In fact, for PG-water mixture the maximum and cross-over points of the density curve are shifted towards much *lower* values ($w^{\max} \approx 0.25$ and $w^0 \approx 0.5$) when compared to the systems above [87] and the mixing rate is thus expected to be significantly smaller [58]. For the PG-water system the $Sh - Ra$ correlation was also found to be nonlinear ($Sh \sim Ra^{0.76}$, red dashed-line) with parameters affected by a relatively large uncertainty (as represented by the red shaded region in the figure). Interestingly, our results seem to follow more closely the correlation found in another study that used the MEG/brine system with similar density curves [21], although also in this case the scaling of the flux was found to be nonlinear ($Sh \sim Ra^{0.84}$, blue dashed-line) and the uncertainty on the obtained parameters is admittedly large (represented by the blue shaded region in the figure).

As anticipated above, one of the key observations from the results obtained in study is the attainment of a linear $Sh \sim Ra$ scaling. Interestingly, this behaviour has been observed in studies on thermal convection in porous media, including observations from experiments [20] and numerical simulations in both two- [88] and three-dimensions [74]. The latter are shown in the plot with the dash-dotted line and predict a flux that is approximately three times smaller than the values observed in this study ($\alpha = 0.379$).

We note that there is a linear scaling specific to Rayleigh numbers that are relatively small ($Ra_c < Ra < \mathcal{O}(Ra) \sim 10^3$). In this regime of Ra the linear relationship between Ra and Sh is based on the assertion that the flux is not dependant on the height of the domain and only a function of the thin diffusive boundary [21, 36]. However, advective mixing becomes the dominant control for $Ra > \mathcal{O}(Ra) \sim 10^4$ [58, 8, 38] where Sh is expected to become independent. Most significantly, our data seem to extend the results from one of the (very) few experimental studies reported in the literature where density-driven convection was investigated in a three-dimensional porous medium (grey-shaded square

symbols) [49]. More observations within this important regime of Rayleigh numbers are needed to corroborate these findings, because at this stage we cannot exclude a priori that our data are affected by the characteristic density behaviour of aqueous MEG solutions [40]. Nevertheless, the conclusion can be drawn that in the regime $1 < \widetilde{Ra} < 100$ ($40 < Ra < 4000$) and irrespectively of the chosen model fluid (pair), the dissolution flux increases linearly with Ra reaching values that are $40 - 100$ times larger than predictions based on diffusion alone. In the context of geological CO_2 storage, this could result in a reduction of the time scale for dissolution from $\sim 80,000$ years down to $\sim 1,500$ years in a 50 m-thick permeable aquifer.

3.5 Summary

We have presented an experimental study on dissolution-driven convection imaged by X-ray CT in a uniform porous medium with MEG-water and BEG-water as model fluid pair. We obtain very good experimental reproducibility in terms of macroscopic measures of mixing, such as onset time of convection, maximum dissolution rate and averaged concentration profiles. Together with the recent work by [39, 76], we provide the first non-invasive determinations of three-dimensional patterns in opaque, random porous media in the regime $\mathcal{O}(Ra) \sim 1000$. The tomograms reveal the emergence and evolution of characteristic concentration structures, which are imaged at a resolution of 10 mm^3 from the onset of convection until its shut-down. The experimental observations are compared to the limiting numerical case of a purely diffusive scenario and are well described by a relationship of the form $Sh = 0.025Ra$ for $Ra < 5000$.

In agreement with previous findings, the comparison with results from other experimental studies are evidence that the extrapolation of observations on analogue model fluids to the CO_2/brine system should be done with caution, due to effects introduced by the characteristic shape of the density-concentration curve. Another important factor which has been previously neglected is the viscosity ratio between the fluids. Here, the BEG system has a significantly larger ratio than the MEG system and produces unique mixing patterns which heavily influence the integral parameters that we look to extract from these experiments such as the onset, shutdown times and the dissolution rate. This, of course, represents an extreme situation that is unlikely to be reproduced in the field, but,

it highlights, again, the need for caution when using analogue fluids to scale up these processes. In addition, we contend that similar risks are posed by the use of simplified two-dimensional systems to mimic a porous medium and to model a process that is inherently three-dimensional. We also observe that there is a lack of direct experimental observations in the regime $\mathcal{O}(Ra) \sim 100 - 1000$, where subsurface processes are very likely to operate. We demonstrate that X-ray CT allows for precise imaging of solute concentrations at a resolution of about $(2 \times 2 \times 2)$ mm^3, thus providing highly-resolved spatial and temporal information on the fundamental behaviour of the convective process. This novel ability is key towards providing more realistic estimates on the extent of dissolution-driven convection in natural environments, because their inherent heterogeneity is likely to play a fundamentally important role in the determination of the convective flow pattern. This will be explored in the following Chapters.

Chapter 4

Investigating the Effect of Different Experimental Geometries

4.1 Introduction and Geometry selection

The majority of the work presented in this thesis was carried out in a spherical geometry. This specific geometry was chosen because it reduced the noise and artefacts in the x-ray tomograms from the Universal Systems HD-350 X-ray CT scanner but part-way through this project the equipment was upgraded. The new Toshiba 64 slice scanner increased the speed and precision of the data collection, and it became possible to investigate the effect of different geometries; namely a cubic and cylindrical vessel. Also, it should be noted that the time resolution was significantly increased and 3 times the number of data points were collected.

A cube and a cylinder were chosen as alternative experimentally geometries because these had been previously used in three-dimensional work have been carried out experimentally in a cylinder [76, 42] and numerically in a cube [71, 30]. The cube is an obvious choice because it represents an extension of the idealises rectangular geometry use in so many of the numerical and experimental studies which used, Hele-Shaw cells, see Chapter 2. The cylinder has also been used previously with PVT studies and in the micro-CT but these were both for practical reasons relating the nature of the technique. Also, a cylinder is almost half-way between the bowl and the cube, the polar coordinates are maintained, but the cross-sectional area is constant.

It has been suggested that the bowl enhances mixing process due to the changing cross section but as yet there is no systematic study of the impact of the geometry on convective dissolution. So, we aim to tackle this problem and understand the sensitivity of to the domain shape. Suitable vessels of comparable size to the original bowl experiment were sourced, the cube has dimensions of $(15 \times 15 \times 15)$ cm^3 and the cylinder has a diameter and height of 15cm. A sketch of the three geometries can be seen in Figure 4.1.

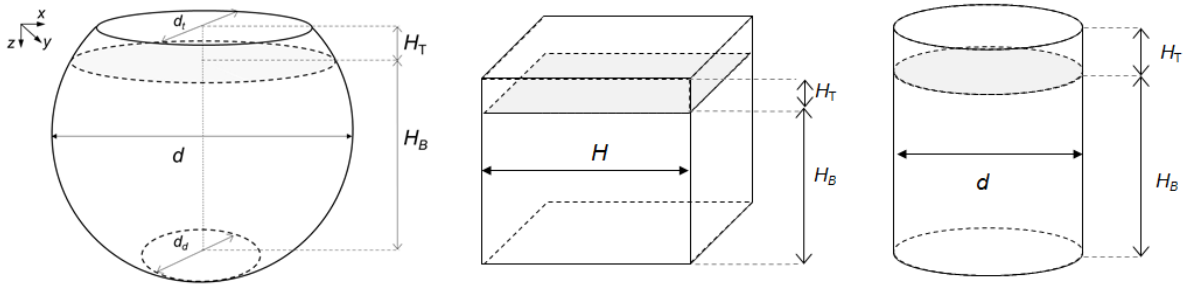

Figure 4.1: Drawing of the three geometries. The bowl (left), cube (middle) and cylinder (right). In the bowl the dimensions are: $d = 18$ cm, $d_\mathrm{t} = 11$ cm and $d_\mathrm{b} = 8.5$ cm, in the cube $H_\mathrm{B} + H_\mathrm{T} = 15$ cm and in the cylinder $d = 14$ cm with a height of 15cm.

4.2 Methodology

The same methodology was adopted from Chapter 2. But, to isolate the effects of the geometry, the experiments were designed so that they would all have the same Rayleigh number, $Ra = 4610$. All the experiments were conducted using the MEG59KI/brine fluid pair with the same height of brine $H_\mathrm{B} \approx 10$ cm) and the same bead size ($d_\mathrm{P} = 0.5$ cm) were used.

The particular mass and volumes of the MEG-KI and brine used in each experiment are detailed in Table 4.1; including the estimated uncertainty in the mass, σ_M and the final mass fraction of MEG $\widehat{w}_\mathrm{B}(t_\mathrm{f})$. The calculations for these can be found in Chapter 2.

As mentioned, the aim was to use similar values for the height of the brine to produce experiments with the same Ra. Unfortunately, due to experimental error too much MEG was put into the top layer in the cylinder experiment. In Table 4.1 we see that there is about 50g more MEG for the cube and the cylinder as compared to the bowl. For the cube because the volume of the bottom section is also larger than the bowl the final mass fraction is similar to the bowl. But, the cylinder has a bottom volume 300ml smaller than

Table 4.1: Summary of experiments presented in this Chapter. The parameters listed in the table have been estimated upon following the procedure described in Chapter 2. M_1 and M_2 are the mass of solution 1 (MEG) and 2 (brine) with estimated uncertainty, σ_{M}; V_{T} and V_{B} are the volumes of the top and bottom sections and $\widehat{w}_{\mathrm{B}}(t_{\mathrm{f}})$ is the mass fraction of solute in the bottom section at the end of the experiment.

Solution	M_1 [g]	M_2 [g]	σ_{M} [g]	V_{T} [mL]	V_{B} [mL]	$\widehat{w}_{\mathrm{B}}(t_{\mathrm{f}})$
Bowl	103.9	784.0	10.2	279.6	2094	0.133
Cylinder	161.2	651.4	2.9	434.1	1742	0.247
Cube	157.9	845.4	1.9	424.9	2258	0.187

the bowl, so the final mass fraction is almost twice as large. Unfortunately, however, only one experiment was performed in the cylinder. However, with this knowledge in mind, we continue with the analysis and include the cylinder results but focusing on the bowl and cube.

4.3 Macroscopic Properties

Following the procedure outlined in Chapter 2 and described in Chapter 3, Figure 4.2 was prepared which shows the fraction of solute (MEG) dissolved in brine, m_j/M_1, as a function of the square root of time, $t^* = \sqrt{t}$, for the three geometrical cases. For each system, the dissolved amount has been calculated for both top ($j = T$, circle symbols) and bottom ($j = B$, star symbols) sections independently. For simplicity the error bars have been removed but the variance of the computed total mass of MEG, $M_1(t) = m_{\mathrm{B}}(t) + m_{\mathrm{T}}(t)$, are reported as σ_{M} [g] in Table 4.1. Due to the upgraded scanning equipment, the error in the measurements is less than half that of the previous scanner. In Figure 4.2 are presented the modified logistic functions that have been fitted to the experimental data (solid curves) together with predictions based on a purely diffusive scenario (straight dotted lines).

Similar to the observations in the bowl, the behaviour for the cube and the cylinder follows a pattern that can be characterised by three dissolution regimes, namely (i) diffusive, (ii) convection-dominated and (iii) shut-down. At early times ($t^* < 1 - 5$ min$^{0.5}$) all the three geometries present behaviour predicted by a purely diffusive scenario, where the dissolved mass grows proportionally to $\sqrt{\mathscr{D}t}$, with $\mathscr{D}$ being the bulk molecular diffusion coefficient. The reason for this is that at these early times the phenomena is dependent only on the

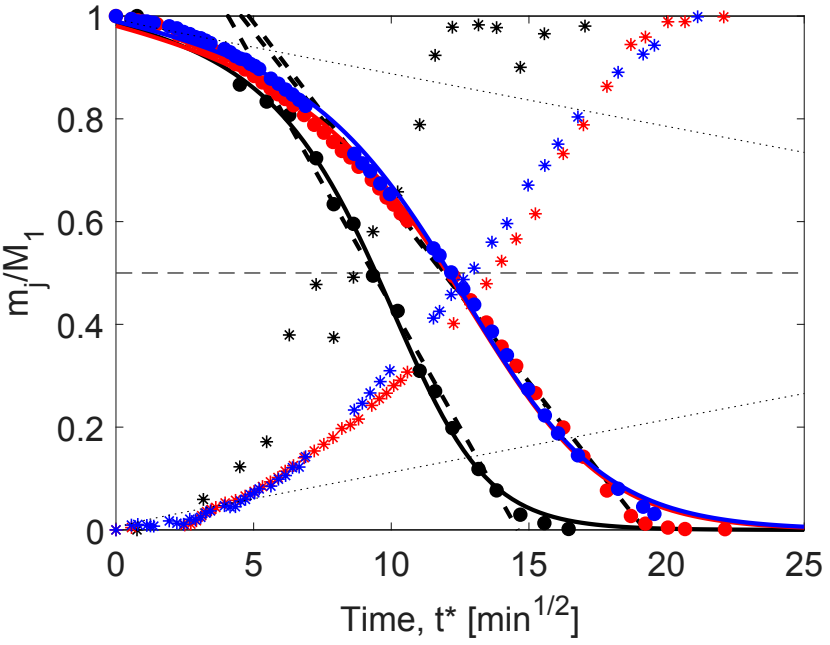

Figure 4.2: Relative mass of MEG dissolved in brine, m_j/M_1, as a function of the square root of time, $t^* = \sqrt{t}$ for experiments conducted in the bowl (black), cube (red) and cylinder (blue). The symbols refer to observations on the top (circles) and bottom (stars) sections. For each geometry, the dotted curves represent a purely diffusive scenario (straight lines, Eq. 2.7) and the solid colour coded lines are the modified logistic functions fitted to the experimental data (equations and parameters given in Appendix). The black dashed lines are linear fits applied to the time period where the process of convective mixing attains a pseudo-diffusive regime; the corresponding parameters ($\mathscr{D}_{\text{eff}}$, t_{c} and t_{s} are summarised in Table 4.2).

fluid properties and the permeability which in all cases has been kept constant. The fluid dependency is confirmed by the estimation of the onset time of convection which is presented in table Table 4.2 the obtained values are 19 ± 9 min (bowl), 20 ± 4 min (cube) and 23 ± 2 min (cylinder). Despite a difference in late time behaviour, the onset times are comparable.

At later times (after the onset of convection) the rate of dissolution diverges between the geometries during the second 'convection-dominated' regime. Yet, the second (pseudo-) diffusive regime is still observed, which is denoted in the figure by the black dashed lines with slopes proportional to $\sqrt{\mathscr{D}_{\text{eff}} t}$. The effective diffusion coefficient is calculated for the different geometries and is summarised in Table 4.2. As before these are presented as the ratio of the effective to the molecular (bulk) diffusion coefficient, $\mathscr{D}_{\text{eff}}/\mathscr{D}$. It can be observed that the coefficient for the cube and the cylinder is half that for the bowl, indicating the mixing in the bowl is happening twice as fast. The convective regime is followed by shut-down which occurs at a similar time for the cube at 365 ± 30 min and the cylinder at 362 ± 13 min but is approximately 150 min slower than the shutdown time

Table 4.2: Macroscopic measures of convective mixing for the bowl, cube and cylinder. The effective diffusion coefficient achieved in the convective regime ($\mathscr{D}_{\text{eff}}$), onset time of convection (t_{c}) and time of convective shutdown (t_{s}). The molecular (bulk) diffusion coefficient takes the value $\mathscr{D} = 1 \times 10^{-5}$ cm^2/s. The parameters and their uncertainties have been obtained using standard relationships for weighted linear regression [83].

Geometry	$\mathscr{D}_{\text{eff}}/\mathscr{D}$	t_{c} [min]	t_{s} [min]
Bowl	105 ± 20	19 ± 9	215 ± 49
Cube	46 ± 2	20 ± 4	369 ± 30
Cylinder	49 ± 3	23 ± 2	362 ± 13

in the bowl.

Figure 4.3 shows three-dimensional reconstructions of the bowl, cube and cylinder at the various dimensionless times, τ, which is used again to make comparisons between these experiments. From the reconstructions, the problem of too much MEG in the cylinder (as described in Section 4.2) is observed as the MEG layer is thicker in the cylinder as compared to the cube or the bowl.

The same regimes are observed in the cube and the cylinder as seen in the bowl; small finger projections underneath the interface giving way to fewer larger fingers growing ($0.01 < \tau < 0.1$, columns 2-4) until they reach the bottom of the domain. Investigating further, we observe differences between finger structures which are indicative of each geometry. In the bowl, the fingers at ($0.01 < \tau < 0.1$, columns 2-4) branch outwards from the initial interface allowing for merging and coalescing of the plumes. In the case of the cube, however, the opposite occurs. The fingers uniformly form across the initial interface and the propagate directly downwards with little contact with neighbouring fingers. In the case of the cylinder, the fingers are less well defined indicating more lateral mixing but still propagate downwards.

In the bowl, shutdown is caused by the depletion of the MEG plume, and we assume for that at the final time the initial MEG layer is filled with fresh brine. This assumption may not be true in the cylinder as at $\tau > 0.086$ there is still MEG in the top layer. At the final time an artificially sharp interface is observed when $\tau > 0.1$ in Figure 4.3. The assumption of fresh brine in the top at the final time but the constraint of the high mass fraction in the bottom causes this unphysical condition in order to conserve mass. However, the τ scaling provides a reasonable visual match between the cube and the bowl geometries which furthers the idea that the pseudo diffusive regime is a characteristic property of the

convective dissolution and a suitable scaling parameter and not a consequence of the bowl geometry.

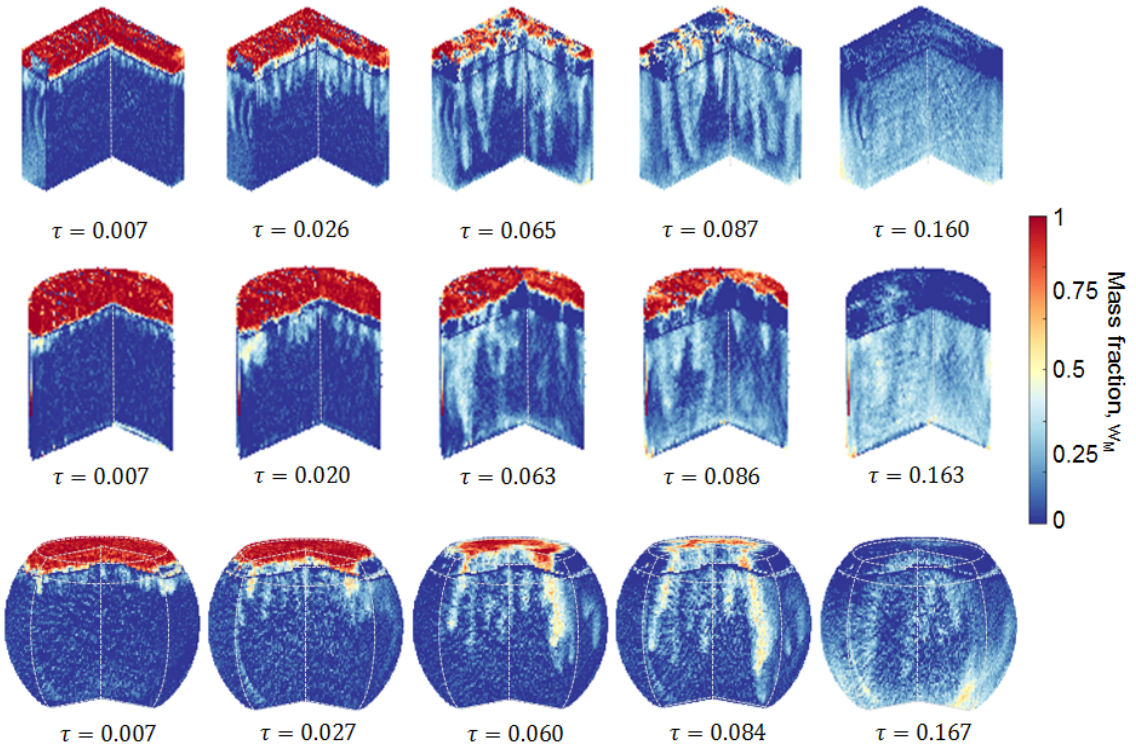

Figure 4.3: Three-dimensional reconstructions of the convective mixing process within the cubel(top row), cylinder(middle row) and bowl(bottom row), as obtained from X-ray CT scans. Images are shown in terms of solute (MEG) mass fraction, $w_i(t)$ as a function of the dimensionless time, $\tau = \mathscr{D}t/H_B^2$. Voxel dimensions are: $(2.3 \times 2.3 \times 2)$ mm^3 for the bowl and $(2.3 \times 2.3 \times 1)$ mm^3 for the cylinder and cube.

4.4 Pattern Formation and Evolution

Figure 4.4 shows 2D horizontal cross-sections of the cylinder and the cube at $z = 2.5$ cm, below the initial interface and Figure 4.5 shows the geometries again but at $z = 9$ cm below the initial interface. In Figure 4.4 and Figure 4.5 similar times are have selected for the sake of comparison.

Starting with Figure 4.4 for both the cube, initially ($t^* < 10$ min) the fingers form very uniformly over the entire cross-section. Individual fingers merge together to form large networks of MEG/brine and patches of fresh brine (10 min$< t^* <$ 20 min). With increasing time, the MEG concentration within the protrusions increases and bridges are formed, thus creating a structure that is largely connected. At late times ($t^* >$ 22 min) the cross-section is saturated with a mixture of MEG/brine however in the cube the average

mass fraction is lower and so appears more blue whereas the cylinder is brighter with patches of high concentration fluid persisting. Previously we noted a strong similarity between the bowl experimental observations and those reported in an earlier numerical study, where these connected structures have been described as a maze [71]. However, in light of the new results in the cube this statement, referring to the bowl, must be revisited as the comparisons between the simulation and our experiments are extremely similar; especially as the literature reports in a cube geometry with a system with $Ra = 6400$ which is very close to that the Ra of the cube.

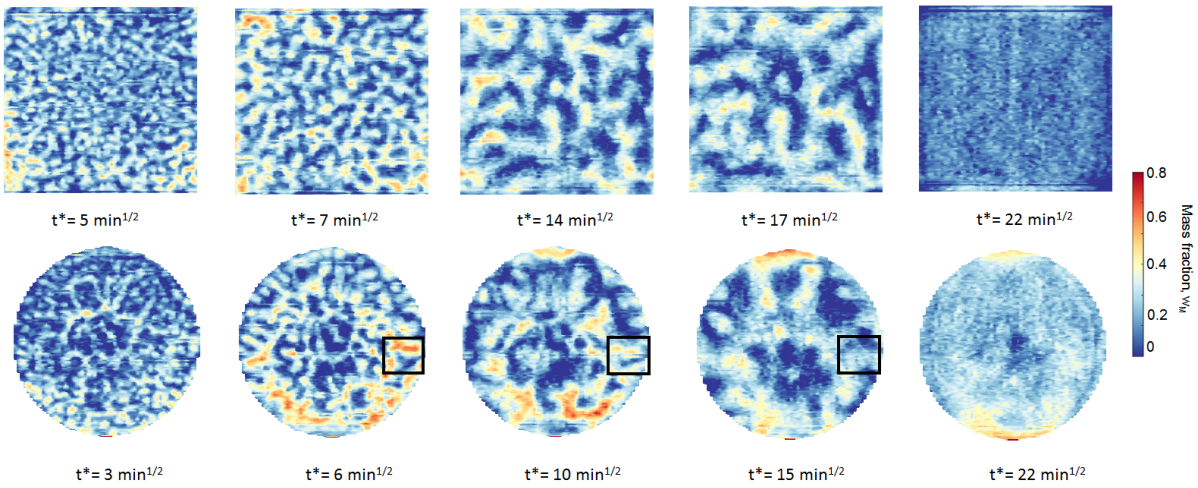

Figure 4.4: Two-dimensional horizontal flow patterns of convective mixing within cube (top row) and cylinder (bottom row) at $z = 2.5$ cm at a given time, $t^* = \sqrt{t}$. Voxel dimensions are $(2.3 \times 2.3 \times 1)$ mm^3 and the images are presented as contour lines of constant MEG mass fraction, $w_i(t)$.

A similar pattern emerges in the cylinder with many small protrusions are formed across the entire interface, most of which are initially disconnected. With increasing time, the MEG concentration within the protrusions increases and bridges are formed. A structure that is largely connected is created with the highest concentration of MEG forming patches at the outer edge of the cross-section. In the cylinder, the 'maze' structure forms much earlier, and the ring structure develops at late times where fresh brine is pushed up through the middle, and the higher concentrations of MEG are present on the outside edge of the cross-section. It is not apparent if the structures observed in the cylinder area result of the geometry or a result of an improper initial interface. Interestingly the structures observed in the cylinder are not dissimilar to the patterns observed in the literature [76] where patches of higher concentration form near the edge as opposed to the middle. However, further work is needed to verify this observation.

As time goes on the higher concentration patches within the ring merge and the internal concentration gradients dilute. This pattern can be readily observed in Figure 4.4 by comparing the region highlighted by the black boxes. At $t^* = 6$ min the concentration at the centre of the finger is w_i 0.6 and this region slowly dilutes and spreads as convection and dispersion processes occur. An extension to this work could be to quantify the effect of dispersion using a similar method outlined in the literature [76]. This characteristic gradual discolouring of the islands can be observed in all geometries.

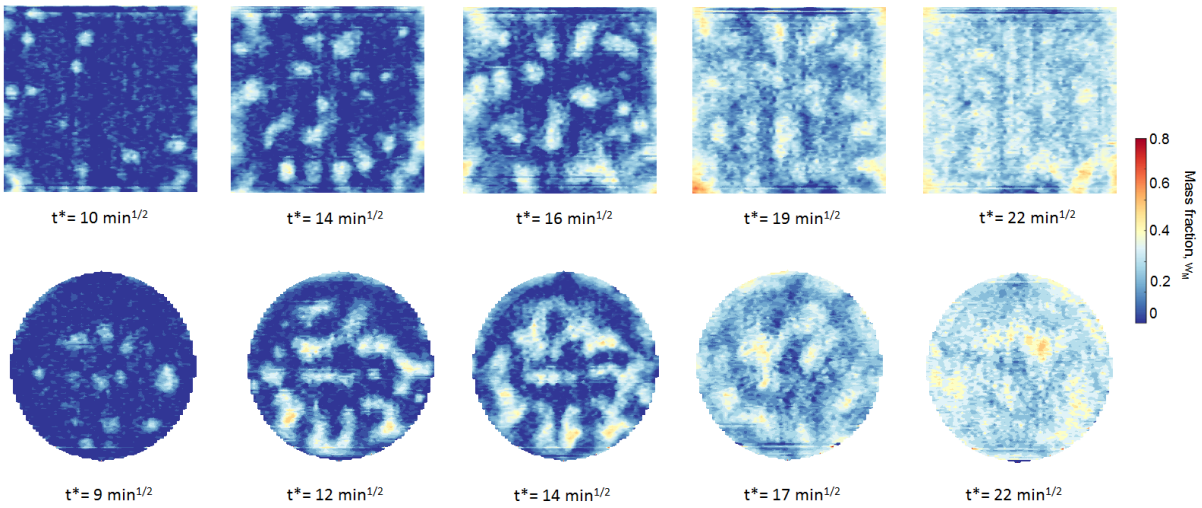

Figure 4.5: Two-dimensional horizontal flow patterns of convective mixing within cube(top row) and cylinder(bottom row) at $z = 9$ cm at a given time, $t^* = \sqrt{t}$. Voxel dimensions are $(2.3 \times 2.3 \times 1)$ mm^3 and the images are presented in terms of MEG mass fraction, $w_i(t)$. Black box highlighting dilution of a single finger over time in the cylinder.

In Figure 4.5 a cross-section has been taken lower down the cube and cylinder at $z = 9$ cm below the initial interface. At $t^* = 10$ min the tips of the fingers reach the plain, in the cube, this breakthrough is spatially random, but in the cylinder, the fingers first appear in the centre of the cross-section. A trait common to all geometries is the appearance of islands of high concentration near the bottom indicating that the columnar fingers can migrate downwards independently. At the final times for all geometries ($t^* > 20$ min) the finger structure has been smeared by dispersion, and the concentration is relatively uniform with a few patches of higher concentration.

4.4.1 Number and Size of the Fingers

Now, we quantify the differences in the pattern formation and evolution. First, the images are simply binarised to measure the number of fingers and the mean area which they

occupy. A simple thresholding technique is applied where MEG fraction $w_i(t) < 0.15$ is assigned to brine(blue) and $w_i(t) > 0.15$ to MEG(red). After binarisation, MATLAB 'counts' the number of distinct connected regions and the area is determined by the number of pixels within each connected region.

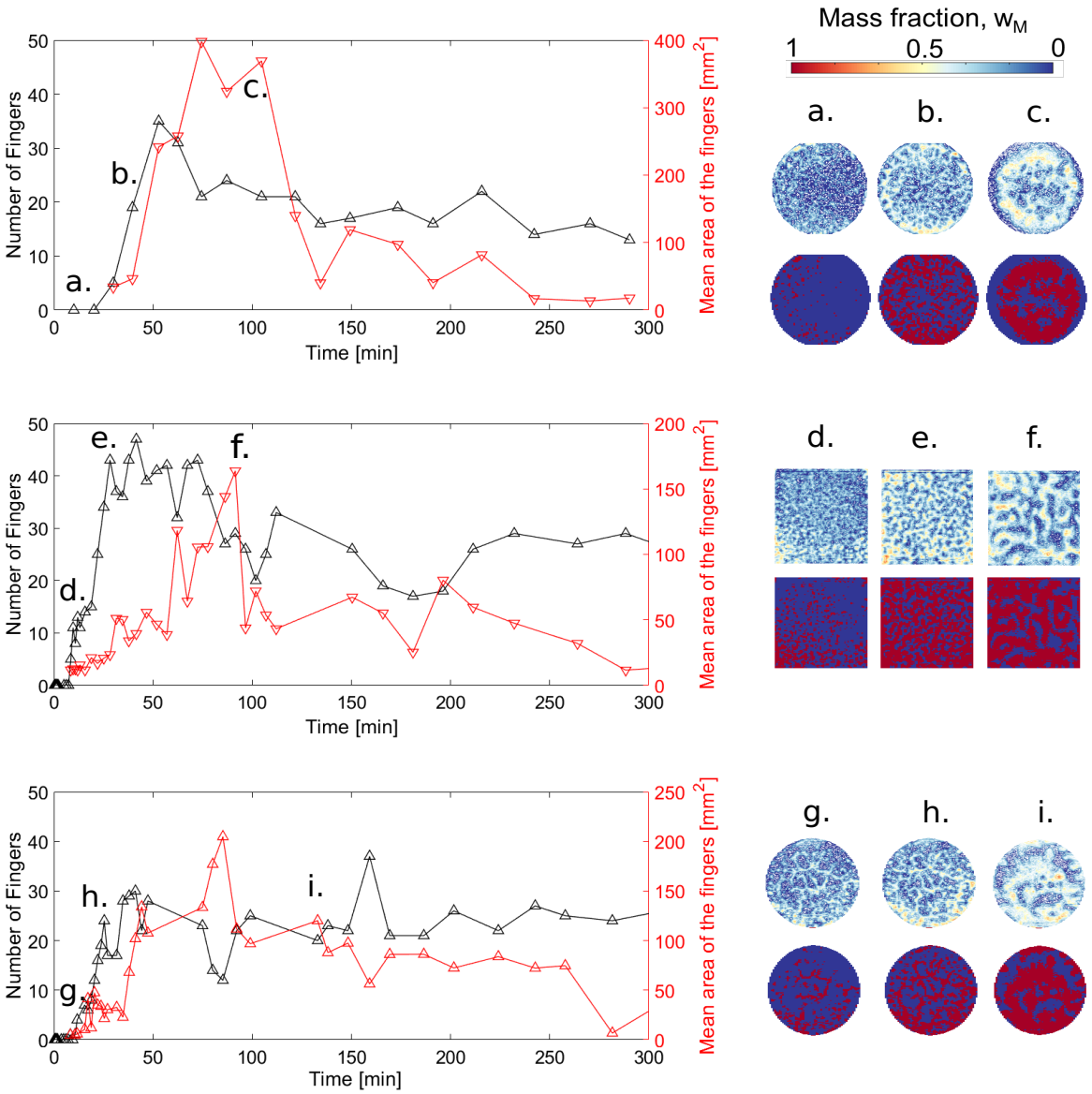

Figure 4.6: Percentage occupied by MEG in a cross section just below the interface as a function of time in the bowl(left) cube(middle) and cylinder(right). The red stars correspond to the binarised reconstructions in. An example of the binarisation of the two-dimensional horizontal flow patterns of convective mixing before(top) and after(bottom) a thresh hold of $w_i(t) > 0.25 = 1$ and $w_i(t) < 0.25 = 0$ has been implemented in the cube at $z = 2.5$ cm at given times, $t^* = \sqrt{t}$.

Figure 4.6 shows each of the geometries bowl (top), cube (middle) and cylinder (bottom), the number of fingers (black) and the mean area of the fingers (red) are plotted on the same graph. For each of the geometries are three examples of the original reconstructions

of a cross section taken at $z = 2.5$ cm below the interface and corresponding binarised image. Each pair of original and binarised images is label a-i so, and they are indicated on the adjacent plots.

At early times (t < 100min) the number of fingers grows rapidly and peaks at 45 fingers in the bowl and 55 fingers in the cube, after which there is a general decrease in the number of fingers. In the cylinder, only 30 fingers are counted in the early time, and this number remains constant over the times shown. The mean area of the fingers is also gradually increases during early times and peaks at $\approx$ 100min for all three geometries but the area itself is twice as large in the bowl where the average finger size is 400mm^2 compared to 200mm^2 in the cylinder and 150mm^2 in the cube. So as observed in the reconstruction, e. there are many more, smaller fingers in the cube compared to the bowl, b. where the fingers are fewer and larger. But, the coarsening dynamics of the fingers are best observed, in the cube geometry where between reconstruction e. and f. the transition between many small fingers and few larger fingers is shown. In e. there are 45 fingers with a mean area of 50mm^2 as compared to f. where there are now 30 fingers with a mean size of 160mm^2.

Quantifying the pattern formation and the finger evolution in a 3D porous medium is one of the novel elements of this work. For the first time, these structures can be observed and mapped over time. These experiments highlight the 3D nature of convective mixing as these patterns could not form in a 2D system.

4.4.2 Spatial Correlation and Semi-variance

Next, we compute a correlation length which is a measure of order in a system.

$$2\gamma = \frac{1}{N}\sum[w_i(h) - w_i(u+h)]^2 \tag{4.1}$$

In this case, it is used to describe how the concentration field is related to different positions within a single cross-section. We use an empirical semivariogram according to Equation 4.1 [89] where the average of the square of the difference between N pairs of the mass fraction of MEG, $w_i(u)$ at location, u, compared to the u + h. Where h, is the voxel 'lag' distance in the x or y-direction.

Practically, the mass fraction of each voxel is compared stepwise to the voxel adjacent

and then the voxel adjacent to that for a distance half the size of the image. This process is repeated for each row of voxels, and this is considered the x-direction and the same is done for each column of voxels which is the y-direction.

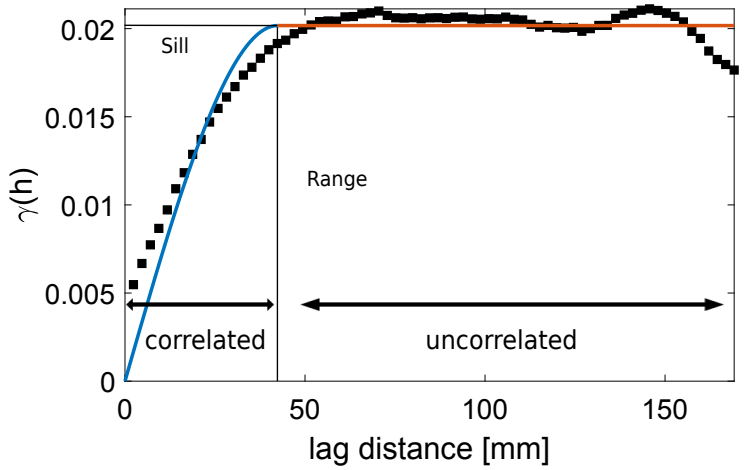

Figure 4.7: Example of a variograms of a 2D horizontal cross section of the cylinder at $t^* = 3$ $min^{1/2}$ in the x-direction with a spherical model fit, indicating the correlated and uncorrelated length, the range and the sill.

The resulting γ is plotted as a function of distance, and a spherical a model is fitted. A spherical model is a common model used to fit variogram data and is used here to fit the data. The defining characteristics of this model are the sill and the range which define the distance at which the data becomes uncorrelated (the range) and the variance associated with that transition (the sill). In Figure 4.7 the semivariance of a cross-section from the cylinder experiment at $t^* = 3$ $min^{1/2}$. In this graph, the data is displayed with black points, and the fitted model is a blue line where the data is correlated and an orange line for the uncorrelated region. The variability increases until a plateau is reached (the sill) where the data is no longer correlated. The range is indicated with a vertical black line and indicates the data has a maximum correlation length of 45mm with a variance of 0.02.

Figure 4.7 is only one example at a single time for one geometry so in Figure 4.8 we show the variograms at three times for each geometry; bowl (left), cube (middle) and cylinder (right) in the x-direction (circles) and the y-direction(squares).

At early times(red curves) the correlation length is comparable in the x and y-direction and is on the order of a cm. For the bowl and the cube, the trend exhibits a cyclical pattern which is attributed to the small uniformly distributed fingers. Although these

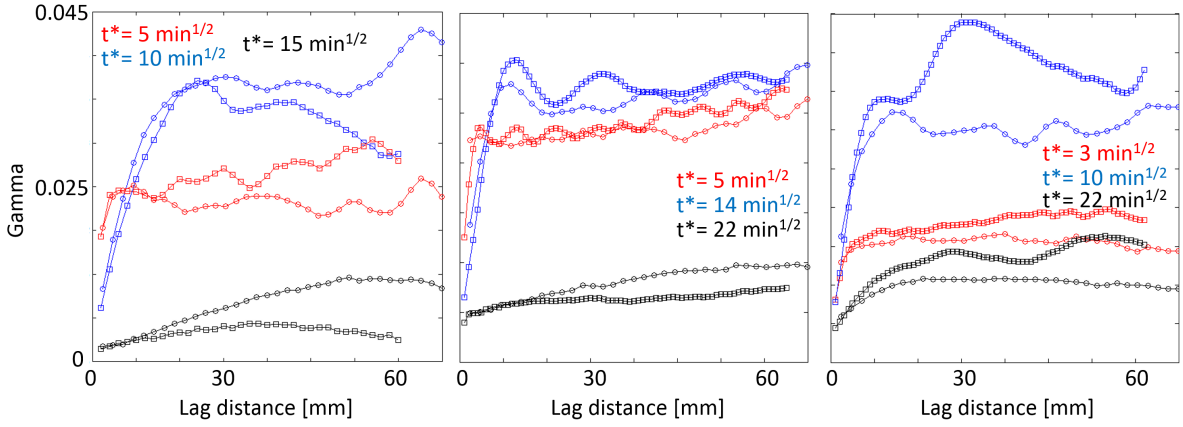

Figure 4.8: Variograms of 2D horizontal cross section of the bowl(left) cube(middle) and cylinder(right) in the x-direction (circles) and the y-direction(squares) at three times during the experiments are indicated in red, blue and black.

are visualised in the cylinder, this is not captured in the variogram. Here, the sill is reached more quickly than for the bowl or cube. Also, the y-direction sill is slightly lower indicating some anisotropy in the concentration field. At intermediary times (blue curves) there is much more variation in the trends. Only the cube shows agreement between the sill level in the x and y-direction. Again there is some oscillation in the curves indicating an underlying periodicity in the concentrations, but the frequency is much lower. This oscillation is in-line with the larger and fewer fingers characteristic of the middle time behaviour. As observed in the 2D horizontal slices, the cylinder and bowl present with similar patterns which are also observed in the trends in the variograms. The presence of a second sill in the cylinder y-direction variogram suggests there is 'zonal anisotropy' which somewhat describes the patches of high and low concentration shown in the reconstructions. The same is true in the bowl but to a lesser degree as the x and y-direction curves do deviate but not as dramatically as in the cylinder. At late times (black curves) for all the geometries, the sill is quickly reached as the concentration field is relatively uniform.

To quantify the differences observed in Figure 4.8 the model is applied to a single cross-section for each time and the range and sill extracted; this procedure is then repeated for each geometry. In Figure 4.9 the sill value (left) and the range (right) is plotted as a function of the square root of time, $t^* \text{min}^{1/2}$ for the bowl (black), cube (red) and cylinder (blue). The trend in both the sill and the range exhibit similarities between the geometries. Initially, the sill increases with time as finger the structures grow, and the concentration

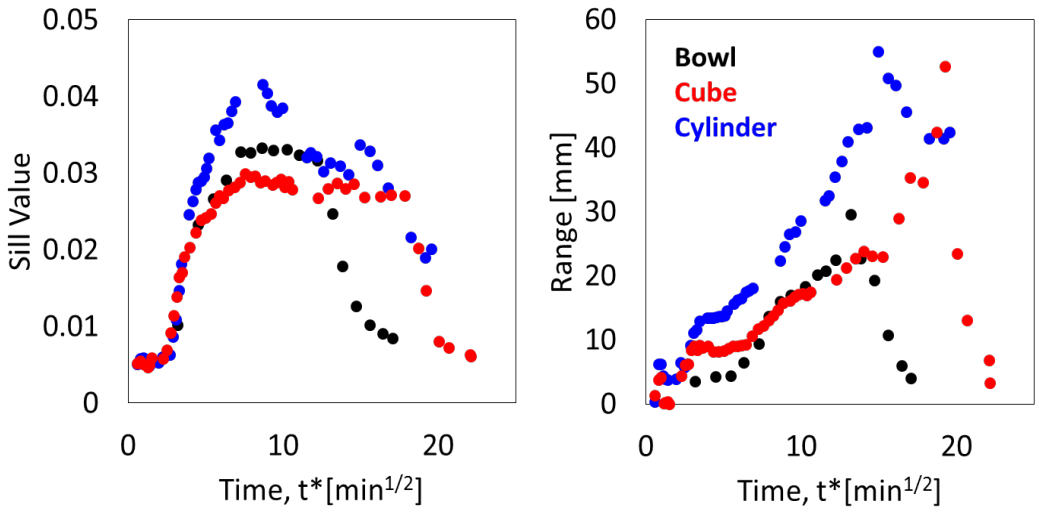

Figure 4.9: The sill (left) and range (right) as a function of the square root of time, extracted from the variogram fit of the data for a horizontal cross section from the bowl (black), cube (red) and cylinder (blue).

variance grows. A constant period is observed in the sill values for the cube and the bowl at times which correspond to the linear region of the MEG fraction plots (see Figure 4.2) at $t^* = 5 - 15\text{min}^{1/2}$ for the bowl and $t^* = 5 - 20\text{min}^{1/2}$ for the cube. The sill value then decreases back to the initial value. In the cylinder the sill values are higher than in the bowl or the cube, this indicates there is a larger range of concentrations, which can be observed in the reconstructions where there are more patches of high and low concentration.

It can be observed that the range or correlation length increases over time in each of the geometries. The range increases faster in the cylinder as compared to the bowl and the cube where the range increases at a similar rate this results in a maximum of 29.6mm ($t^* = 13.8\text{min}^{1/2}$) in the bowl, 55.0mm ($t^* = 14.9\text{min}^{1/2}$) in the cylinder and 52.6 mm ($t^* = 13.8\text{min}^{1/2}$) in the cube. After which, the range decreases rapidly for all cases. Interestingly, the decrease in the sill value and the range coincide with timings of the shutdown of convection (see Table 4.2) as the mixture homogenises.

Now we look more closely at the cube and bowl, where we observed similar trends in the sill and the range. There is a similar maximum variance in the bowl and cube which indicates the variation in concentration fields are comparable despite the different finger patterns which are observed in the geometries. And, as the variance is constant as the range increases, it indicates that the fingers are growing larger, but the concentration of the fingers is not changing. The rate of increase in the range is the same for the bowl

and the cube until $t^* = 13.8\text{min}^{1/2}$ where convection shuts down in the bowl. But, for the cube the correlation length continues to increase at the same rate, peaking at 52.6mm at $t^* = 19.2\text{min}^{1/2}$.

In Figure 4.6 the number of fingers were calculated along with the mean area or size of the finger. In each case, at later times ($t^* > 10\text{min}^{1/2}$) the number of fingers remains constant but the average size decreases, together with an increasing correlation length these results indicate lateral dilution of the fingers. The number of fingers stays the same, but the size decreases because the outer, diluted surface is no longer counted as 'MEG' when the threshold is applied. However, the correlation length continues to increase because the fingers are smearing together and the distance between two related points is becoming larger. However, once the sill value begins to reduce, which occurs $\approx$ 20min prior, the range also rapidly decreases.

These results show that the evolution of the patterns was prematurely disrupted in the bowl due to the earlier shutdown time. But, in the cube, we observe the full range of coarsening dynamics predicted in the literature [71]. It would be interesting as an extension to properly match these the results in the cube to the simulation.

4.5 Discussion

Ra gives an upper bound for the strength of the buoyant forces compared to diffusive forces for a given system as Ra uses the maximum density difference possible for a fluid pair. In practice, the density differences of the fluids are dynamic and dictated by a unique mixing curve. To understand how this curve controls or effects *Ra* the instantaneous Rayleigh number, (Ra_I) is calculated.

$$Ra_{inst} = \frac{k(\rho_{\text{top}} - \rho_{\text{bottom}})H_{\text{B}}g}{\mu_2\phi\mathscr{D}} \tag{4.2}$$

The average mass fraction is taken for the top and bottom sections independently and using the density curve presented in Chapter 2 for the appropriate MEG ratio to compute the density, ρ_{top} and ρ_{bottom} respectively. It is important to note that there is a degree of numerical mixing which also occurs as a result of this calculation for example at the onset, only a layer smaller than either domain will have become buoyant. Thus, the estimate

here is therefore not an upper bound. The calculations are for the entire of each layer and this may not represent the physics perfectly, however it is an interesting analysis of the relative driving force of the process. Figure 4.10(left) shows the density profiles of the top section(circle symbols) and the bottom section (star symbols) for the bowl(black), cube(red) and cylinder(blue). In each case, MEG59 has been used, so the maximum density of the top layer is consistent between the geometries.

Initially for all cases Ra_I is negative as MEG59(ρ_{top}) is less dense than the brine(ρ_{bottom}). As mixing occurs, the density profiles cross and at that point, $Ra_I = 0$. A peak is then observed before Ra_I becomes negative again. Interestingly, the time of crossover is similar to the onset time calculated from the deviation of the linear region and the diffusion curve, which is logical as the only once the top layer becomes heavier than the bottom can convection start. In a similar fashion the time for shut down coincidences with the second crossover of the density curves and where is $Ra_I < 0$. Both these times, however, are slightly over and under the estimated times from Figure 4.2. The comparison can be seen in Table 4.3. The linear fit method under predicts and overpredicts the onset time and shut down time respectively as it takes the time of intersection between 1 and 0 instead of where the linear region starts and stops. Also Ra_I compares the behaviour between the top and bottom sections whereas the linear fit method relies on only the top curve.

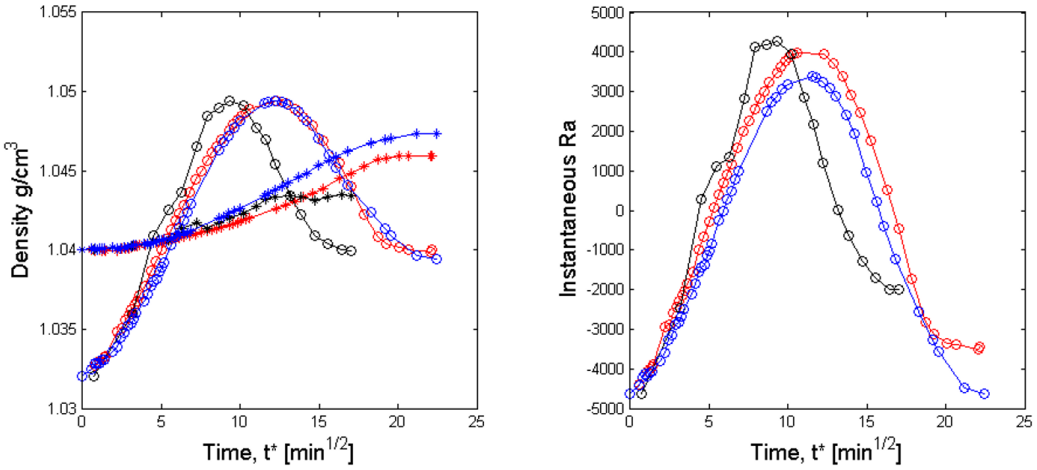

Figure 4.10: Left: Average density for the top (circles) and the bottom (stars) section of the bowl (black), cube (red) and cylinder (blue) as a function of time. The density is calculated from the measured density curves presented in Chapter 2 using the average mass fraction of the sub domain. Right: instantaneous Rayleigh number as a function of time in the bowl (black), cube (red) and cylinder (blue). Ra_I is calculated from equation 4.2 where ρ_{top} and ρ_{bottom} are taken from the left hand plot.

The interaction between the two sub-domains is important here as it affects the relative

strength of the Rayleigh number. Considering that the peak density in the top section is always constant, it could be argued that the peak in Ra_I should also always be constant. Here, it is shown that this is not always true. In the cylinder, due to an initially thicker MEG layer, the density of the bottom continues to rise as the MEG layer mass fractions fall. This, counter-intuitively, results in a lower Ra_{Imax} for the cylinder where $Ra_{Imax} = 3390$ compared to the cube where $Ra_{Imax} = 3984$. Further work is needed into understanding how the thickness of the initial MEG layer affects the flow and ultimately the mixing potential.

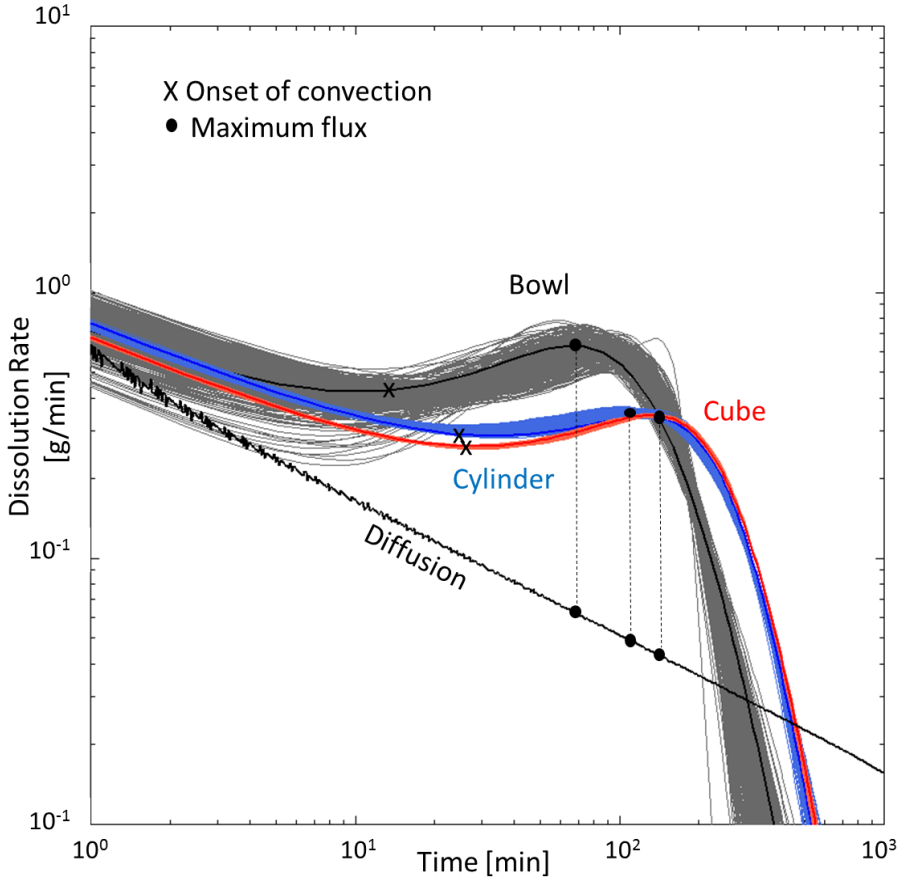

Figure 4.11: Rate of dissolution as a function of time for the bowl (black), cube (red) and cylinder(blue). Obtained from differentiating the modified logistic function fitted to the experimental data (Figure 4.2). The solid black line is the numerical solution of the purely diffusive scenario. The cross symbols are the rate of dissolution at the time of the onset of convection (estimated from Figure 4.2), while the circles represent the time at which the maximum rate of dissolution is attained.

The dissolution rate as defined in Chapter 3. is calculated and shown for the different geometries in Figure 4.11. Previously, to account for the uncertainty of the experimental observations, 300 additional realisations of the fitting-differentiation were averaged and plotted. With the improvements in the equipment and the reduction in the variations, when the same procedure was applied the agreement between the realisations for the

Table 4.3: Comparison of Ra_{Imax} for each of the geometries and the corresponding time. The estimation of the onset time of convection (t_c) and time of convective shutdown (t_s) using the linear fit method and where $\mathrm{Ra}_I > 0$. Also time of maximum flux as estimated from Figure 4.11.

Geometry	Ra_{Imax}	$t(Ra_\mathrm{max})$ [min]	$t(r_\mathrm{max})$ [min]	t_c [min]	t_Rac [min]	t_s [min]	t_Ras [min]
Bowl	4262	87	73.6	17 ± 8	20	202 ± 46	173
Cube	3984	150	140.7	23 ± 2	28	362 ± 13	264
Cylinder	3390	133	123.4	24 ± 2	37	378 ± 18	242

cylinder (blue) and the cube (red) was much greater than for the bowl (black) as shown in Figure 4.11.

The trend in the dissolution rate is similar to that presented in Chapter 3. Initially, the rate follows closely the trend predicted by the diffusion model before diverging to a maximum (indicated with a black circle Figure 4.11) and then quickly falling off. And, these trends can be correlated to the regimes of pure diffusion, convection-dominated and the shutdown of convection. As expected the cube and the cylinder follow similar trends with a small difference in the time of the maximum dissolution rate; the cylinder, peaking at 124 min with a maximum rate of dissolution of 0.37g/min and the cube at 140 min with a rate of 0.34g/min. Now, when we compare the time for the onset of convection, t_c and the time of the maximum rate, $t(r_\mathrm{max})$ is observed for all the cube that $t(r_\mathrm{max}) \approx 6t_\mathrm{c}$ and for the cylinder, $t(r_\mathrm{max}) \approx 5t_\mathrm{c}$. It should also be noted that Ra_{Imax} peaks correspond well with the peak in the flux as noted in Table 4.3.

Throughout this Chapter, the MEG fraction curves, the reconstructions and dissolution rate have all indicated that convective mixing in the bowl is progressing systematically faster than the cylinder or the cube. When the Sherwood number is calculated using the maximum rate and the corresponding diffusive flux it is observed that for the cylinder $Sh = 80 \pm 2$ and $Sh = 79 \pm 3$ for the cube. Interestingly, values for the Sh which are lower than the bowl case where $Sh = 96 \pm 17$ but still within the range of the error. Therefore this suggests that despite the apparent differences in the macroscopic properties, ultimately the effective enhancement due to convection is not strongly dependant on the geometry.

4.6 Summary

The main application of this work is carbon storage, and within any geological formation, a range of geometries will arise. This work highlights the importance of understanding how heterogeneity and the formation shape impacts the flow and ultimately the amount of dissolved CO_2. The bowl was originally chosen to overcome practical difficulties in scanning large dense objects and so was used for much of the work presented in this thesis. During the conclusion of this project a newer, better scanner became available, and it became apparent it was possible to investigate a range of geometries.

Macroscopically, it appears the cylinder and the cube are in agreement which would indicate that either; the changing cross section in the bowl is further enhancing convection or the effects of the boundaries in the cube and cylinder are impeding the convective process. But, by analysing the pattern formation, it is clear that each geometry gives rise to different internal finger structure. It was possible to observe the coarsening dynamics in the cube and the bowl where initially many small fingers formed which merged and created larger and fewer fingers. The spatial correlation of the fingers was also investigated, and it was found that the correlation length of the patterns increases linearly with time until the shutdown of convection. This is the first time pattern formation has been observed in an opaque porous medium which has a striking similarity to published simulation results [71].

The final conclusion of this work was that ultimately the Sh is not dependent on the geometry as for all three cases it was surprisingly close, despite the observed difference in finger structure and the dissolution rate.

Chapter 5

Effect of Permeability Heterogeneity: Single Angled Layer of Lower Permeability

5.1 Introduction

In this Chapter, the effect of adding a single layer of lower permeability in an otherwise homogeneous packing on the process of convective dissolution is investigated. The aim was to produce a quantitative and systematic experimental study on this topic. This is of particular importance in the field where sedimentation frequently produces a series of horizontal layers with significantly different permeabilities to the host rock. One such example is the Sleipner oil field where seismic studies reveal the presents of mudstone layers, precisely of the nature described [90, 91]. The specific combination of thickness and permeability ratio can be quantified by the so-called 'Impedance' (Ω) which represents the resistance to flow in the system due to the presence of a barrier layer. Impedance is defined by the ratio of the height or thickness of the impermeable layer, h_L and the height of the entire bottom domain H_B divided by the ratio of the layer permeability,k_L and the bulk permeability,k as shown in Equation 5.1

$$\Omega = \frac{h_L/H_B}{k_L/k} \tag{5.1}$$

This concept was applied to a simulation study on the analogue problem of convective heat transfer [74] where it was reported that between $\Omega = 0.1$ and $\Omega = 10$ a peak in the Nusselt number is observed. The Nusselt number is the Sherwood number equivalent for heat transfer which compares the heat transfer rate to the diffusive rate. Thus, given all else being equal, a peak in the Nusselt number is a result of an increase in the thermal flux. In the literature this was partially explained through the concept of flow focusing, wherein, the breakthrough of the plume through the impermeable layer is at a few, well-spaced locations so it is 'focused' or more 'ordered' [74]. The mechanism by which this increases the flux is described in the literature as a result of larger and faster moving velocity fields underneath the low permeability field. Therefore this work aims to determine if an increase in the solute flux is observed experimentally and whether or not this shows any links to flow focusing.

5.2 Experimental Apparatus

A very simple form of permeability heterogeneity is a single layer of differing permeability compared to the bulk. Here, a lower permeability layer is selected, and the complexity is taken one step further by introducing a 5° angle. This incline was implemented to more accurately represent reservoir configurations as in reality strata are rarely absolutely horizontal and also for curiosity as previously there have been no imaging studies specifically looking at a single angled layer in three dimensions. However, in one previous work, a two-dimensional system with an inclined lithological interface of 10-15° was evaluated [54] and the effects on the plume was mapped over time. The results of that study indicated an increase in lateral spreading and a decrease in the vertical propagation of the fingers at the interface. This work will expand on that idea by examining only a single layer instead of a lithological interface and by varying the thickness of the layer and by comparing a range of permeability ratios between the layer and the bulk.

Hence, a range of permeability ratios was selected in order to examine a suitable range of Impedance. In Table 5.1 the thickness and permeabilities of the layers and bulk are presented along with the corresponding Impedance and Ra. For all cases, the height of the entire bottom domain, H_B, is 12 cm and the top domain is approx 3 cm. For experiments 1-3 two repeats (a and b) were performed so in total there are 10 datasets. The specific

Table 5.1: Parameters of the thickness of the layer, h_L, and the permeabilities of the layer, k_L and the bulk k with the corresponding Impedance, Ω, and Ra for each experiment.

Exp No	Ω	h_L [cm]	k_L $[m^2]$	k $[m^2]$	Ra
1a,b	5.33	4	4.75×10^{-11}	7.6×10^{-10}	2452
2a,b	1.33	1	4.75×10^{-11}	7.6×10^{-10}	4359
3a,b	0.33	1	1.54×10^{-10}	7.6×10^{-10}	7847
4	0.33	1	4.75×10^{-11}	1.9×10^{-10}	2943
5	0.67	2	4.75×10^{-11}	1.9×10^{-10}	2452
6	2.08	1	7.59×10^{-12}	1.9×10^{-10}	1226
7	4.17	2	7.59×10^{-12}	1.9×10^{-10}	736

experiments can be separated into two parts based on the bulk permeability k. Experiments 1-3 were performed with a larger background permeability ($k = 7.6 \times 10^{-10}\ m^2$) than experiments 4-7 ($k = 1.9 \times 10^{-10}\ m^2$). As before, we define V_T as the volume of the initial voxels containing MEG and V_B as the voxels below the initial interface containing brine, these will be referred to as 'top' and 'bottom' sections.

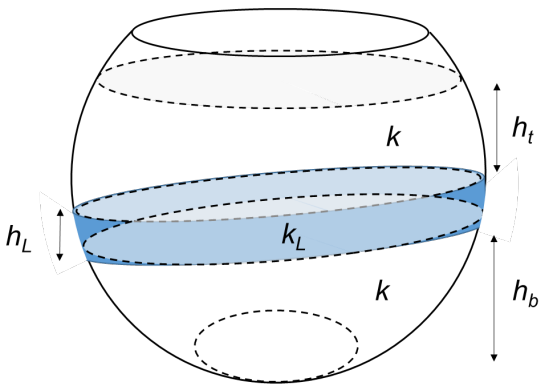

Figure 5.1: Drawing of the experimental geometry with the addition of a single angled layer of lower permeability. The layer has a thickness, $h_L = 1$, 2 or 4cm and permeability, k_L the height of the region above the layer, $h_t = 4$cm with permeability, k and the height of the bottom, h_b varies in accordance to the thickness of the layer also with permeability, k. The bowl is packed with soda glass ballotini of differing sizes resulting in different permeabilities of the regions as specified in Table 5.1.

The thickness of the layer, h_L is set to either 1, 2 or 4cm using a bead that provides a lower permeability,k_L, than the background permeability. k. Figure 5.1 is a sketch of this system where h_t is the height of the region above the layer and is constant throughout all the experiments. So, when the thickness of the layer has increased the height of the

region below the layer, h_b decreases.

$$k_{avg} = \frac{H_B}{h_t/k + h_L/k_L + h_b/k} \tag{5.2}$$

Ra for these cases will be calculated using the harmonic-averaged permeability according to Equation 5.2

A similar procedure was used to prepare and run the experiments as outlined in Chapter 2. However, to create the angled layer, the bowl was packed on a wedge with a 5° angle. Initially, the bowl was wet packed with the background beads in a 6 wt% NaCl solution to a height of h_b. By process of gentle shaking and tapping an even angled surface of beads was created. On to which the small beads were carefully distributed to build up a layer of height h_L. Once an even layer of small beads is established the final layer of background beads is packed up to a height of h_t. At this point, the bowl is taken off the wedge, and the wet packing continues until a horizontal interface is produced. The MEG-KI slurry was prepared as before, and the experiment is started in line with the methodology set out in Chapter 2.

5.3 Macroscopic Properties: Experiments 1-3

First we consider experiments 1-3, the common theme of which is the background permeability of $7.6 \times 10^{-10}\ m^2$ and in each case two repeats were undertaken. Table 5.2 lists the parameters for each experiment along with the error in the measurement for each experiment. Exp1, which has the highest Ω is the only experiment performed with the old scanner, and so the error is inherently greater, and there are fewer data points. The average estimated uncertainty for the mass in experiment 1 is 9.95 g compared to exp 2 and 3 where the average is 1.95 g and 2.7 g respectively. Here, it should also be noted that experiment 2 and 3 were run using MEG57 whereas all other experiments were performed with MEG59. The density curves and associated density differences are outlined in Chapter 2.

Next, using the same method as outlined in Chapter 3 the MEG fraction is calculated and plotted in Figure 5.2 for the top (red) and bottom (blue) section as a function of the square root of time for exp 1 (triangles), exp 2 (squares) and exp 3 (circles) and results

Table 5.2: Summary of experiments reported in this Chapter. The parameters listed in the table have been estimated upon following the procedure described in Chapter 2. M_1 and M_2 are the mass of solution 1 (MEG) and 2 (brine) with estimated uncertainty, σ_{M}; V_{T} and V_{B} are the volumes of the top and bottom sections of the bowl and $\widehat{w}_{\mathrm{B}}(t_{\mathrm{f}})$ is the mass fraction of solute in the bottom section of the bowl at the end of the experiment. For each experiment, $H_{\mathrm{T}} = 3$ cm and $H_{\mathrm{B}} = 12$ cm.

	MEG	M_1 [g]	M_2 [g]	σ_{M} [g]	V_{T} [mL]	V_{B} [mL]	$\widehat{w}_{\mathrm{B}}(t_{\mathrm{f}})$	$\mathscr{D}_{\mathrm{eff}}/\mathscr{D}$
Exp 1a	59	139.1	716.1	11.3	374.2	1912	0.194	36
Exp 1b	59	153.3	701.7	8.7	412.6	1874	0.218	37
Exp 2a	57	98.6	942.9	1.5	267.3	2518	0.105	228
Exp 2b	57	87.6	979.1	2.4	237.4	2615	0.099	222
Exp 3a	57	142.1	814.8	3.8	385.2	2176	0.174	168
Exp 3b	57	98.3	943.2	1.6	266.5	3519	0.104	158
Exp 4	59	131.1	823.8	2.8	352.7	2200	0.159	91
Exp 5	59	134.6	823.4	2.8	362.2	2199	0.163	123
Exp 6	59	127.9	830.1	1.4	344.3	2217	0.154	103
Exp 7	59	129.2	828.8	1.8	347.8	2213	0.156	95

are reported for two repeated experiments (empty and filled symbols). Also on this plot is the modified logistic fit (the parameters of these can be found in Appendix A4) for each experiment. In general, and as seen previously, there is a good reproducibility between the repeats but the trend deviates from the sigmoid curves presented in previous Chapters for exp 1 and 2.

Looking more closely, at very early times, $t^* < 2\ min^{0.5}$ all experiments converge towards to the diffusive limit. The average onset times are estimated as 0.93 ± 4.4 min for exp 1, 2.5 ± 1.1 min for exp2 and 2.9 ± 1.5 min for exp 3 which indicates that the onset in exp 1 is 2.9× faster than exp 2 or 3. This trend is somewhat consistent with the homogeneous experiments presented in Chapter 3 where the onset was 1.5× faster between the MEG59 and MEG57, and here MEG59 is used in exp 1 and MEG57 used in exp 2 and 3. However, future work may include investigating onsets times in more detail as the inherent error in the measurements and insufficient time resolution allows for only rough estimates of onset time for exp 1.

The slope in the linear region of the trend was previously an indicator of a secondary (-pseudo) diffusive process related to finger growth, here we can use this metric to quantify the relative speed of the dissolution. At intermediary times $3 < t^* < 8\ min^{0.5}$ there is a crossover between the curves. Exp1 which had the quickest onset time is now the slowest, where average $\mathscr{D}_{\mathrm{eff}}/\mathscr{D} = 36.5$ which is 5 times slower than exp 2 ($\mathscr{D}_{\mathrm{eff}}/\mathscr{D} = 225$) which is

progressing the fastest.

The trends presented here suggests that the dissolved amount and the Impedance are not linearly correlated but that the rate of growth of the fingers appears to oscillate as Impedance increases. Only at later times, $t^* > 8min^{0.5}$ do the trends in the curves establish themselves according to the Impedance. Shut down in experiment 3 which has an Impedance of 0.33 quickly reduces the MEG fraction close to 0 while a long tailing persists for exp 1 and exp 2.

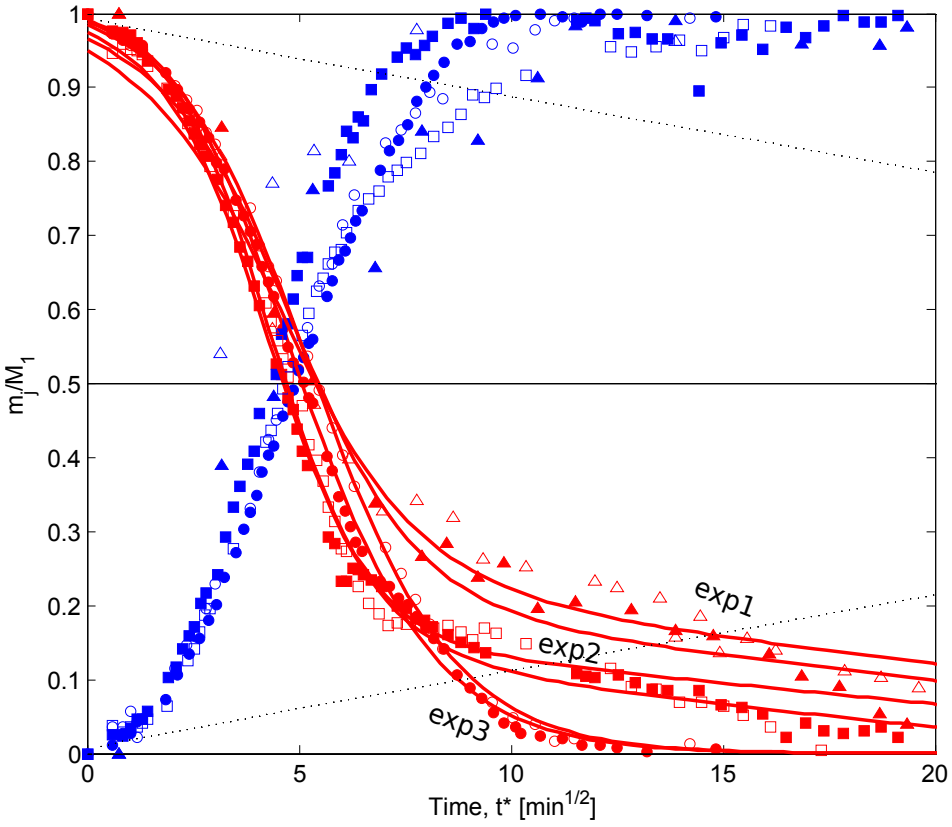

Figure 5.2: Relative mass of MEG dissolved in brine, m_j/M_1, as a function of the square root of time, $t^* = \sqrt{t}$ for experiments conducted with Exp1 (triangle symbol), Exp2 (square symbol) and Exp3 (circle symbol). Two independent sets of experiments are shown for each scenario (filled and empty symbols). Colours refer to observations on the top (red) and bottom (blue) sections of the bowl. In each plot, the two sets of dotted curves represent a purely diffusive scenario (straight lines, Eq. 2.7) and modified logistic functions fitted to the experimental data (equations and parameters given in Appendix).

5.4 Experiment 4-7

The analysis now focuses on Exp4-7 where multiple tools are used to understand the impact of the layer heterogeneity better.

5.4.1 Macroscopic Properties

Exp 4-7 experiments represent a systematic increase in the Impedance for a constant background permeability of 1.09 $\times 10^{-10}$ m^2. The Impedance is increased by using two different permeabilities of the barrier layer 7.59 $\times 10^{-12}$ m^2 and 4.75 $\times 10^{-10}$ m^2 and by using two different thickness of either 1 cm or 2 cm.

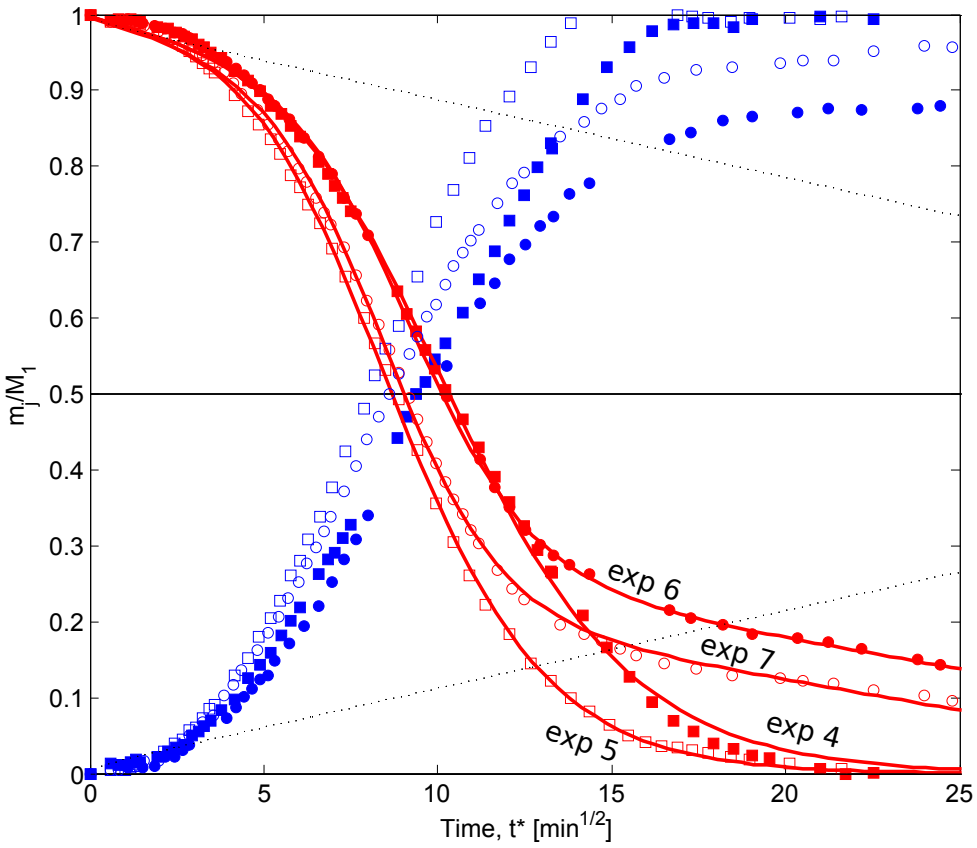

Figure 5.3: Relative mass of MEG dissolved in brine, m_j/M_1, as a function of the square root of time, $t^* = \sqrt{t}$ for experiments conducted with Exp4 (filled square symbol), Exp5 (empty square symbol) and Exp6 (filled circle symbol) Exp7 (empty circle symbol). Colours refer to observations on the top (red) and bottom (blue) sections of the bowl. In each plot, the two sets of dotted curves represent a purely diffusive scenario (straight lines, Eq. 2.7) and modified logistic functions fitted to the experimental data (equations and parameters given in Appendix).

The MEG fraction curves for the top (red) and bottom (blue) section are plotted in Figure 5.3 as a function of the square root of time for exp 4 (filled squares), exp 5 (empty squares), exp 6 (filled circles), exp 7 (empty circles). Interestingly two distinct trends appear on this graph, one which is similar to the homogeneous case with a regular sigmoid curve and the other presents with a long tailing at late times similar to exp 1 and 2. As

in the previous figure, the experiments with the lower Impedance (exp 4 & 5) follow a sigmoid trend similar to the homogeneous case and those with a higher Impedance (exp 6 & 7) exhibit a tailing behaviour at late times $t^* > 15min^{0.5}$. The increased Impedance causes compartmentalisation of the plume, saturation of the leading to a slower dissolution of the MEG; this will be discussed further in Section 5.4.2.

However, after the onset of convection, which occurs at a similar time for all 4 experiments, (16.8 ± 2, 15.1 ± 2, 20 ± 2 and 14.5 ± 3 min for exp 4-7) the curves diverge at two separate rates. Exp 5 & 7 appear to progress noticeably faster than exp 4 & 6 at intermediary times, $5 < t^* < 12\ min^{0.5}$. By comparing $\mathscr{D}_{\text{eff}}/\mathscr{D}$ as presented in Table 5.2 the coefficients do not follow the same trend. Exp 4 has a $\mathscr{D}_{\text{eff}}/\mathscr{D} = 91$ with an Impedance of 0.33. When the Impedance doubles (exp 5) then $\mathscr{D}_{\text{eff}}/\mathscr{D}$ increases by a factor of 1.35. But, when the Impedance is increased further to 2.08 and then doubled to 4.17 (exp 6 and 7) $\mathscr{D}_{\text{eff}}/\mathscr{D}$ there is a decrease of $\mathscr{D}_{\text{eff}}/\mathscr{D}$ by a factor of 0.92 . The commonality between exp 4 & 6 and 5 & 7 is not the permeability ratio but the height of the impermeable layer. What is more unusual is that exp 5 & 7 (the faster experiments) have, the thicker 2cm layer. The implication is that for a given permeability ratio, the thicker the layer, the faster convection takes place and would suggest that the nature of the underlying reservoir has an impact on the formation and evolution of the fingers.

Both Figure 5.2 and Figure 5.3 suggest that the speed of the convection dominated regime is not linearly correlated with Impedance. This behaviour has been shown for both the cases where Ω is increased by either increasing the permeability ratio (exp 1-3) or the thickness of the barrier layer (exp 4-5 and exp 6-7). We recognise here that one weakness of this work is that the dynamics underneath the layer. An alternative method that should be perused in the future is to separate the bottom domain further into sub-domains based on permeability. This would allow the solute to be tracked through the sub domains the residence time could be plotted as a function of permeability.

5.4.2 Two-Dimensional Reconstructions

Looking more closely at the finger structure further insights can be gleaned into the cause of the differing rates observed in the MEG fraction curves shown in Figure 5.3. Five central cross sections at similar times are presented in Figure 5.4 for each of the

experiments 4-7 so that the times chosen can be directly compared to Figure 5.3.

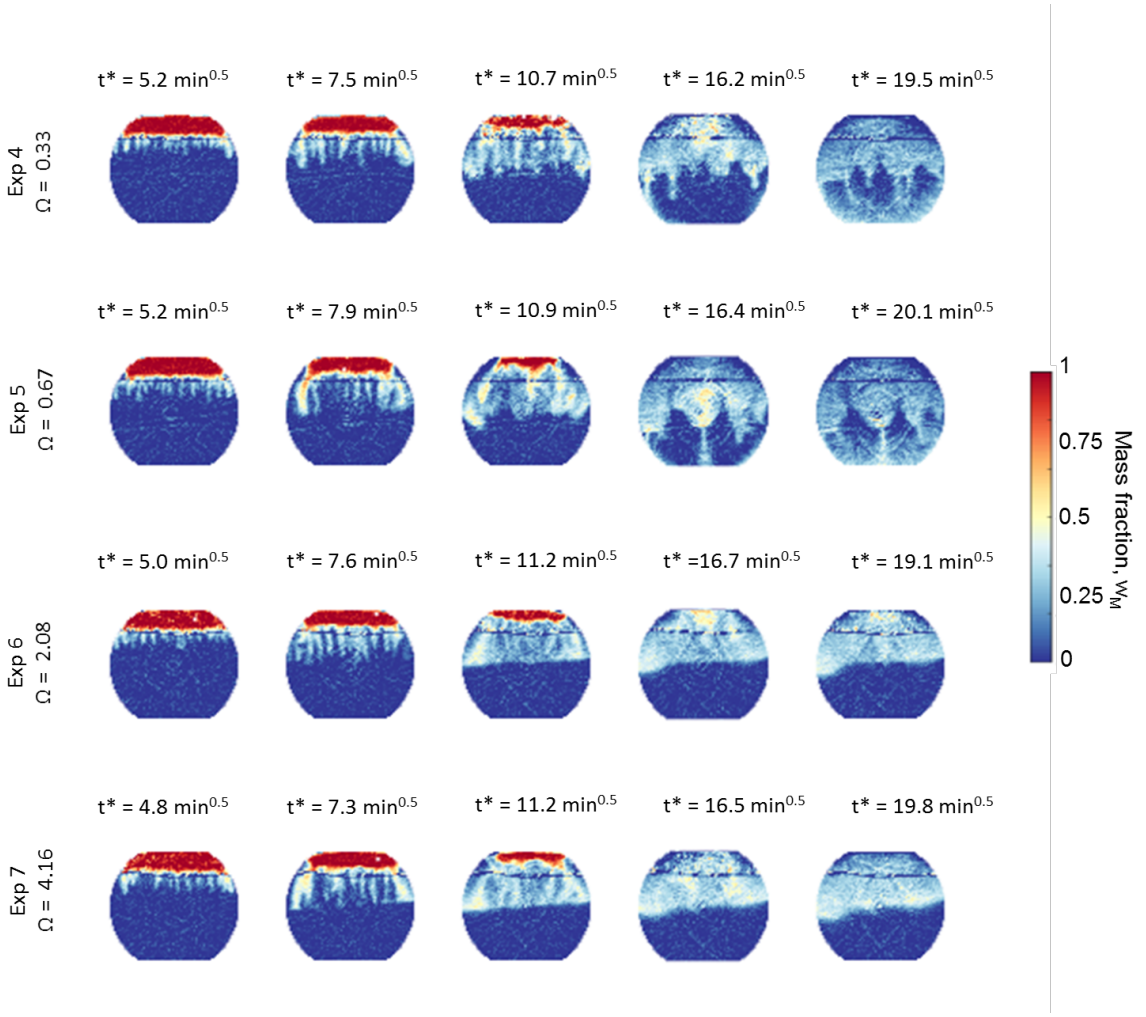

Figure 5.4: Two dimensional reconstructions of the central vertical slice. Each row represents one of exp 4-7 and time, $t^* = \sqrt{t}$, increases from left to right. Similar times have been selected for each experiment. Voxel dimensions are $(2.4 \times 2.4 \times 1)$ mm^3.

Column 1 represents the early time $t^* \approx 5min^{0.5}$ where the fingers have just formed. At this point the MEG fraction curves are still moving at a similar rate which is reflected in the reconstructions; a similar number of fingers have formed, and they have penetrated a similar depth into the bowl for each case. In the second column, $t^* \approx 7.5min^{0.5}$ the MEG fraction curves have now diverged and exp 5 & 7 are progressing more quickly than exp 4 & 6. From the reconstructions, this can be explained by the apparent finger width and penetrated depth. First comparing exp 4 & 5, the fingers in exp 5 have (in this cross-section) fewer fatter fingers compared to exp 4 where the fingers are still uniformly sized and distributed. Next comparing exp 6 & 7, the solute plume has already come into contact with the layer in exp 7 and is beginning to pool and merge at the interface, in, exp 6, however, the fingers are still distinct and have not reached the barrier. In general,

there are strong similarities in the finger structure between exp 4 & 6 whereas exp 5 & 7 present unique evolutions of the plume. This result suggests that there is more than one mechanism for increasing the rate of dissolution. It also suggests that as the rate of dissolution is determined before the fingers 'touch' the layer and the resistance of the packing impacts the global flow structures and not only the local flow field.

Column 3 represents a time $t^* \approx 11min^{0.5}$ which is just before the tailing behaviour is observed in the Figure 5.3 for exp 6 & 7. The region above the barrier is becoming saturated with MEG and the fingers pool and merge, but there is still some MEG in the initial reservoir. The opposing behaviour is observed in exp 4 & 5 where the individual fingers are still visible. However, the penetration depth of the plume is similar for all cases and in none of the cases have the fingers broken through the layer. Therefore it can be said that the process is faster in exp 5 & 7 as more MEG must have dissolved from the initial layer.

In the fourth column the flow has interacted with the barrier for all cases and at some points broken though. At $t^* = 16.5min^{0.5}$ in exp 5, a few dominant fingers have developed and are focusing the flow as described in the literature [74] as compared to exp 4 where more fingers are less ordered. At late times $t^* > 20min^{0.5}$ the finger structures persist for the lower Impedance cases but the concentration has been smeared out, and there is some evidence of pooling of MEG at the bottom of the bowl. For the cases with a higher Impedance, there is an accumulation of MEG above the barrier layer which is consistent with figure 5.3 as the rate slows significantly and there is a long tailing observed.

Although this reconstruction help to understand the observed macroscopic behaviours, the analysis is largely qualitative. Further investigation via simulations would give a greater insight into this behaviour through analysis of the velocity fields and by considering a greater range of Ω. This trend will be discussed in more detail in Chapter 7.

5.4.3 Horizontally Averaged Concentration Profiles

In Figure 5.5 are presented the vertical profiles of the mass fraction of solute, w, at various times for exp 4-7 which have an Impedance of 0.33, 0.67, 2.08 and 4.16. Similar to Chapter 3 the profiles represent the average of all voxels in each 2.5 mm-thick horizontal cross-section of the bowl and are shown as a function of the square root of time. In

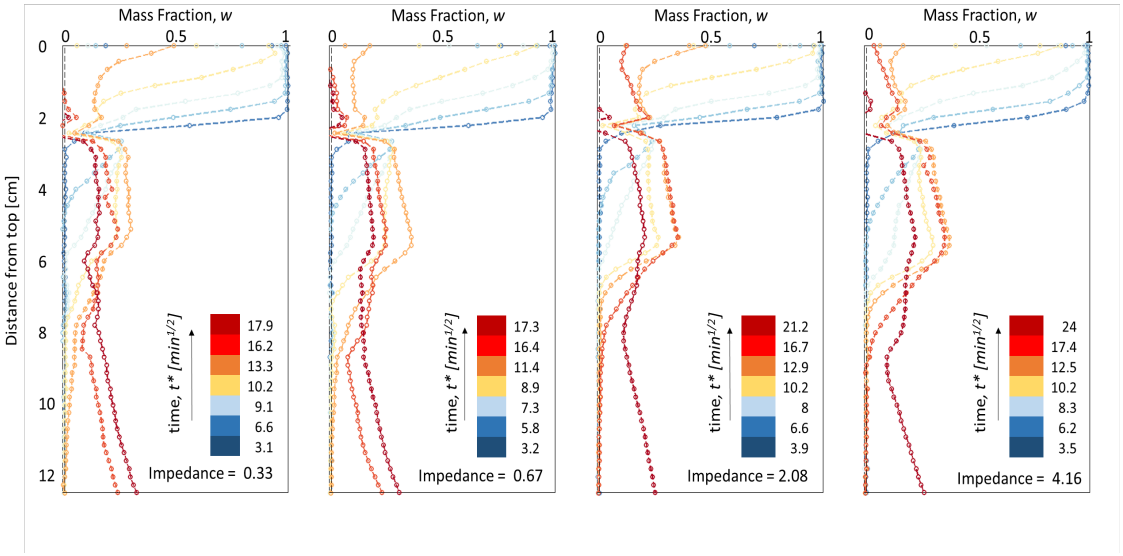

Figure 5.5: Horizontally-averaged profiles of the MEG mass fraction, w, as a function of the distance from the top of the bowl, z. Results are shown for the four experiments with different Ω (from left to right: $\Omega = 0.33$, 0.67, 2.08 and 4.16). For each scenario, profiles are shown at similar values of the square root of time, $t^* = \sqrt{t}$.

general, the time evolution of the plume is similar for each of the cases. First and as also observed in the homogeneous case (Chapter 3) it is observed for each case that the MEG/brine interface recedes gradually. At early times (blue curves) material begins to build up below the interface in the region above the barrier layer which is approximately 2-6cm from the top. The effect of the layer causes a 'bump' in the concentration profile as the less permeable layer is preventing the movement of the plume.

At intermediate times (yellow and orange curves) for each experiment, the region above the barrier contains a fairly high concentration of MEG. However examining the trends in more detail the 'bump' has a higher maximum concentration for $\Omega > 2$ where $w \approx 0.4$ compared to $\Omega < 2$ where $w \approx 0.3$. This observation is a result of the solute accumulated in the top region where the fingers merge and pool as the plume has yet to pass through the layer. Another feature of the region above the barrier is that the concentration is not uniform. There is a gentle increase in the mass fraction between the 2.5 to 6cm from the top, and this slope is more pronounced in exp 5 & 7 where the Impedance is 0.67 and 4.16 which is a result of a quicker recession of the MEG layer which is also apparent in column 3 of Figure 5.4. The reasoning follows that the fraction of MEG is higher because more MEG has dissolved. The question remains, what is the mechanism causing the MEG to dissolve more quickly?

At late times (red curves), the pure MEG solution has completely dissolved, and the 'bump' in the profile is beginning to smooth out. Interestingly, the region below the barrier does not evenly fill with solute, but instead, the same behaviour observed in the homogeneous case is replicated where the solute plume accumulates at the bottom of the bowl.

Although the general trends are similar for each of the cases when the timings are considered the same trend is observed as in Figure 5.3 where the experiments with the thicker layer progress more quickly. It is clear from these profiles that the region above the layer is becoming saturated with MEG faster for a thicker layer compared to a thinner layer.

5.5 Dissolution Rate and Effect of Impedance

Using the fitted curves shown in Figure 5.2 and Figure 5.3 the average dissolution rate is calculated and plotted for exp 1-7. The rate for the first set (exp 1-3, dotted lines) is higher than the rate for the second set (exp 4-7, solid lines) because overall the Rayleigh number is larger as shown in Table 5.1 and the rate is proportional to Ra. Otherwise, for all cases the shape of the curves are similar, there is an initial period where the trends follow the diffusive limit and then there is an increase resulting in a peak in the rate before a sharp decrease. In Table 5.3 the onset of the convection, t_c, the maximum rate, $r_{\max}$ and the time of the maximum rate $t(r_{\max})$ are collated. In both data sets the trend in the maximum rate does not follow the Impedance and instead for both cases there is an oscillation in $r_{\max}$ with an increase in Impedance.

Looking first at exp 4-7, we notice that when the permeability ratio is kept the same but the Impedance is doubled by increasing the thickness of the layer there is a systematic increase in the time of the maximum rate, $t(r_{\max})$. So, between the Impedance of 0.33 and 0.67 and between the Impedance of 2.08 and 4.16 the maximum rate increases by 30% and $t(r_{\max})$ $\approx$15 min is earlier. However, consistently for all four experiments, the time to reach maximum dissolution rates is about 3.5 times larger than the time required for the onset of convection, i.e. $t(r_{\max}) \approx 3.5t_c$; this suggests that the onset time of convection and the time of the maximum rate are properties of the system size.

Between exp 3 and exp 2, the thickness of the layer is kept the same but the permeability

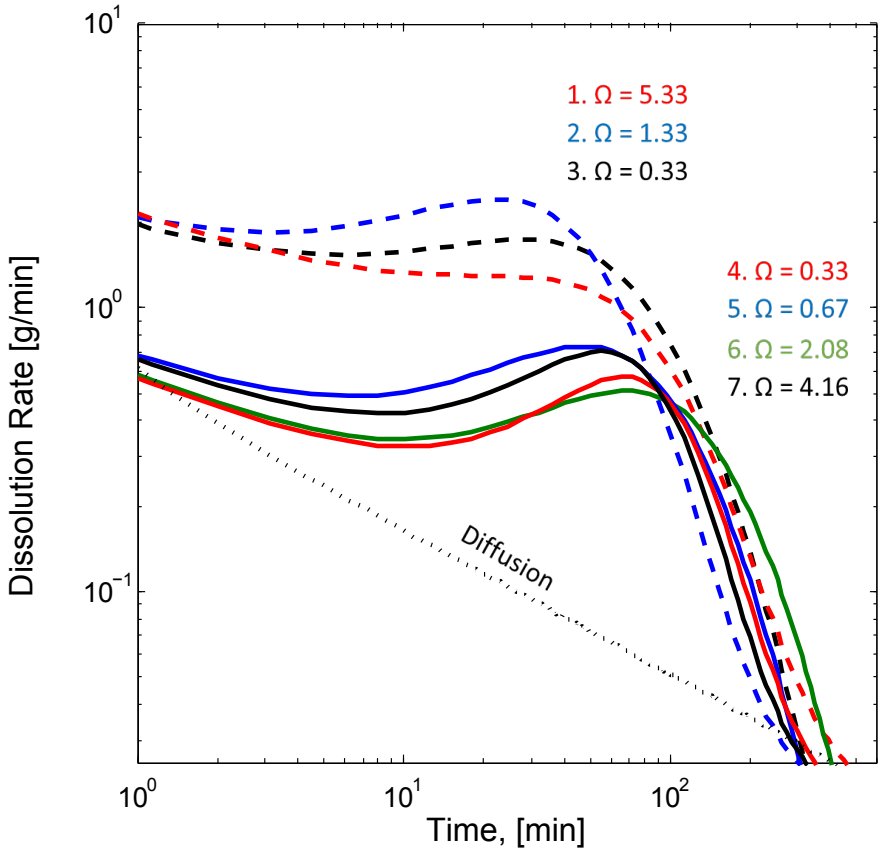

Figure 5.6: Average rate of dissolution as a function of time for the exp 1-3 (dashed , 1.red, 2.blue and 3.black) and exp 4-7(solid 4.red, 5.blue, 6.green and 7.black) obtained upon differentiating the modified logistic function fitted to the experimental data (Figure 5.2 and Figure 5.3), while the dotted black line is the numerical solution of the purely diffusive scenario (Chapter 1).

ratio is increased from $k/k_L = 4$ for exp 3 to $k/k_L = 16$ for exp 2. Interestingly the effect on the maximum is the same as for exp 4-7; there is an increase of 30%. It can be concluded that the effect of the permeability ratio and the thickness of the barrier layer on the rate and the movement of the plume is not necessarily the same. As an extension, the Impedance may not accurately capture these effects as it treats both quantities with equal weight.

Using the same method as presented in Chapter 3 the Sherwood number can be calculated from the peak of the dissolution rate curve compared to the diffusive rate at the same point. According to equation 3.2 a length scale is required over which the maximum rate has been acquired. However, here, a less permeable layer has been introduced and this length scale has been reduced from the height of the bottom domain to the height of the region above the barrier for those cases where the MEG fraction curve presents late time tailing behaviour.

Table 5.3: Summary of the length scale, H_B, used to calculate the Sherwood number for each experiment and the corresponding Sherwood number for the homogeneous case, Sh_0.

Exp No	t_c [min]	$t(r_{\max})$ [min]	$r_{\max}$ [g/min]	H_B [cm]	Sh	Sh_0
1a	0.8 ± 5	12.5	0.63 ± 0.10	4	16 ± 7	367
1b	1.04 ± 4	36.1	1.31 ± 0.08	4	58 ± 10	367
2a	2.8 ± 1	24.5	2.41 ± 0.02	4	94 ± 2	245
2b	2.6 ± 1	21.1	2.48 ± 0.03	4	88 ± 3	245
3a	3.1 ± 2	28.1	1.73 ± 0.03	10	176 ± 3	245
3b	2.8 ± 1	21.1	1.99 ± 0.02	10	182 ± 2	245
4	16.8 ± 2	66.1	0.52 ± 0.02	10	82 ± 8	96
5	15.1 ± 2	50.0	0.74 ± 0.02	10	100 ± 3	96
6	20.0 ± 2	66.1	0.57 ± 0.01	4	37 ± 2	96
7	14.5 ± 3	55.1	0.71 ± 0.02	4	42 ± 3	96

Therefore a length of 4 cm instead of 10cm is used for exp 1, 2, 6 and 7. Sh for each experiment is detailed in Table 5.3 along with the corresponding Sh_0 the Sherwood number for the homogeneous case. Sh_0 is estimated using the relationship between the Rayleigh number and Sherwood number, $Sh = 0.025Ra$ for $Ra < 5000$ as established in Chapter 3. The Ra_0 calculation assumes a homogeneous packing of permeability, k where the length scale is either $H_B = 10$cm. For exp 4 and 5, however, the $Sh_0 = 96$ is used directly from the homogeneous experiments.

Here the focus is on the $Sh - \Omega$ comparison and in the next Chapter, there will be a comparison of all experiments with Ra. Figure 5.7 plots Sherwood number (left) and the normalised Sh/Sh_0 (right) against Ω, two colours are used to indicate the experimental set, exp 1-3 (blue) or exp 4-7 (orange). Looking at the $Sh - \Omega$ plot first, there is clear trend where as Impedance increases Sh decreases. The trend in the Ra number is also indicated on this plot and as expected Ra follows the Sh trend by decreasing with Impedance. We highlight the $\Omega = 0.33$ cases where there is a difference of 100 between the blue and orange points. By looking at Ra it can be seen that Sh is proportionally higher for the higher Ra case ($Sh \approx 180$, blue) compared to the case which has a Ra three times lower ($Sh \approx 80$, orange). At the opposite end of the spectrum at $\Omega \approx 5$ the Rayleigh number is 2452 ($Sh \approx 40$, blue) and 736 ($Sh \approx 42$, orange) but the Sh is similar. So, Figure 5.7(left) suggests that at low Impedance, Ra has more effect on the rate of dissolution than at high Impedance.

In Figure 5.7 (right) we plot the normalised Sherwood number to compare the deviation resulting from the introduction of the layer. At $\Omega < 0.5$ the Sh is about 80% of the homogeneous value for both the blue and orange points. There is a peak observed in the data at $\Omega = 0.67$ where the mass rate is now higher in the system with a resistive layer compared to the homogeneous case. For, $\Omega > 1$, Sh is 40% of the value of the homogeneous case, this is consistent with prior work with also suggests that there will be a gradual decrease in Sh/Sh_0 after the peak of $\Omega = 0.5$ [88].

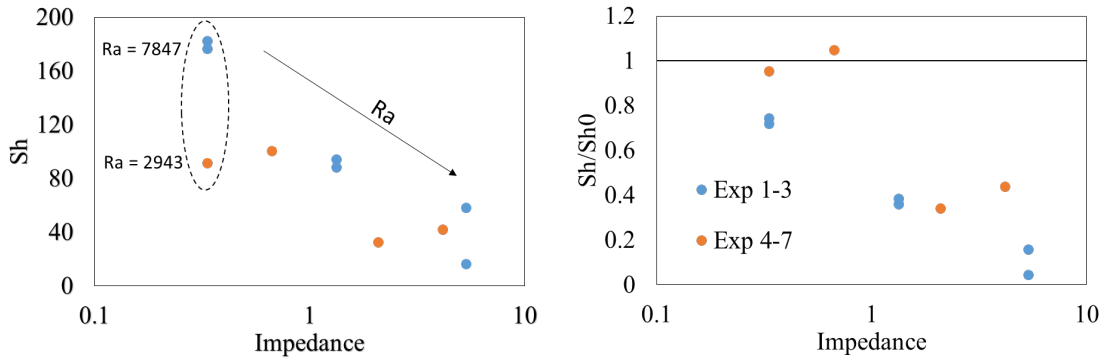

Figure 5.7: Left: Sherwood and right: the normalised Sh plotted against the corresponding Impedance for the two data sets exp 1-3 (blue) and exp 4-7(orange). The details of each point can be found in Table 5.3.

However, it is important to recognise here that there are some significant differences between the simulated work and the practical possibilities of the experimental set up described here. Firstly, the simulations used periodic boundaries conditions on the top and bottom of the geometry to which they apply a constant heat flux. Experimentally this is, of course, not possible and instead a closed system is used where MEG is only present on the top boundary. Also in the simulations quantities such as the flux are taken at statistical steady state, experimentally we do not observe such a state and instead take a maxima. Other differences may also exist in the underlying assumptions and simplifications of the model. However, the simulation work takes a fresh look at a classic problem and uses a logical metric, Ω, to quantify the system. Also this metric, to our knowledge, has not been applied to the problem of solute mass transport in a three dimensional system. The one anomalous point is Exp7, from the reconstruction and the concentration profiles it is clear that the fingers are indeed growing the moving faster than the other cases. Further work, with either repeated experiments or simulations, will shed light on this unexpected result. The final points suggest that Sh/Sh_0 does decrease if the Impedance is sufficiently large.

5.6 Summary

Initially, this work set out with two goals; 1. to investigate the flow structures that arise in the presence of a simple barrier heterogeneity and determine how these structures influence the mass rate and 2. to see if this results in a trend similar to that reported in the heat transfer literature.

With that in mind, this Chapter presents an experimental study on dissolution-driven convection imaged by X-ray CT in a uniform porous medium with the addition of a single angled layer of lower permeability where MEG-water was used as a model fluid pair. Two experimental sets were presented with differing bulk/background permeabilities. The ratio between the permeability of the bulk and the layer was varied as was the thickness of the layer in a manner so that $0.1 < \Omega < 8$ could be investigated. For each experiment macroscopic measures of mixing such as change of mass over time and horizontally averaged concentration profiles were investigated, culminating in an assessment of the relative rate across the Ω range. The tomograms provided unique insights into the emergence and evolution of the plumes which are ultimately responsible for the macroscopic properties.

The results of this analysis is not straight forward, however. The increases and decreases in the flux at lower Impedance can be explained by understanding the flow structures that emerge as the experiment progress. The idea of flow focusing or flow ordering is a viable explanation for an increase in the flux at $\Omega < 2$ compared to the homogeneous case. But little evidence from the reconstructions can explain why the flux increases when $\Omega > 2$. In the literature, it was stated in the concluding remarks that the no linearity of flux with Impedance 'remains puzzling' [74] and instead of solving or confirming the puzzle this study has added a level to complexity. Previously, the relationship between the height of the layer and the flux was negatively correlated (i.e. as the height increases the flux decreases) but in this case the results hint at the possibility that this is not the case. It is not possible to make a definitive conclusion and further work is needed to fully understand this relationship and the flow dynamics which underpin this process.

Chapter 6

Effect of Permeability Heterogeneity: Discontinuous Heterogeneity

6.1 Introduction

The following Chapter investigates the effect of discontinuous heterogeneities akin to those found in natural reservoirs. In the literature, two types of heterogeneity have been studied most widely both experimentally and numerically and those are barrier heterogeneity where the width and spacing of the impermeable barriers were varied or anisotropic heterogeneity [11]. The general consensus on the effect of heterogeneity is that the most important factor is the effective vertical permeability, in short, if the barrier space is larger or the barriers are further apart this increases the effective vertical permeability and in turn, the dissolution rate increases, similarly for a constant horizontal permeability if the effective vertical permeability increases the dissolution rate also increases.

Studies previously published on convective mixing in the presence of permeability heterogeneity have been mostly 2D numerical studies [92, 63, 65, 62, 60, 67] and the few experimental studies which visualise flow have also been in 2D [54, 70, 68]. Therefore, this work aimed to filled a gap in the literature but providing the first three dimensional study.

So, for the design of the experiments we investigate two discontinuous angles, as shown on the left of Figure 6.1. Two experiments were performed for this case where the permeability ratio between the background,k, and the layer, k_L, (k/k_L) was set to be either 4 or 25. Then a Patchy configuration was used where 3 layers of horizontal circular patches of

Table 6.1: Summary of permeabilities used in each experiment for the layer, k_L and the bulk k with the corresponding volume fraction of lower permeability and Ra.

Name	k_L $[m^2]$	k $[m^2]$	V_L/V_B $[m^3]$	Ra
2 layers $k/k_L = 25$	7.59×10^{-12}	1.9×10^{-10}	0.19	3007
2 layers $k/k_L = 4$	4.75×10^{-11}	1.9×10^{-10}	0.17	3209
Patchy	7.59×10^{-12}	1.9×10^{-10}	0.21	2937
Random	4.75×10^{-11}	1.9×10^{-10}	0.25	2989

lower permeability were introduced into the packing, here $k/k_L = 25$ and a sketch is shown on the right of figure Figure 6.1. The location of the patches is offset in each layer with the idea that the flow would be forced to meander around the barriers and create a similar flow dynamic as observed in the literature [54, 68].

The final configuration is a Random mixture of smaller and larger beads in a ratio of 1:3 by volume. The beads used for this experiment were chosen so that the attenuation of the two bead sizes were different enough that they could be identified in the raw image and a rough permeability map could be estimated. This result will be discussed further in Section 6.3. For all these experiments the 'background' bead was 0.5 mm with an average permeability of 1.9×10^{-10} m^2, thus allowing direct comparison to the homogeneous case. Table 6.1 presents the permeability of the background, k and the layers, k_L for each experiment also the volume fraction of the lower permeability zones and the corresponding Ra.

Ra is calculated based on an estimate of the average permeability k_{avg} as derived from a linear combination of the volume fractions of the beads in the layer, V_L and the bulk, V_B and the corresponding permeabilities for the layer and the bulk according to Equation 6.1.

$$k_{avg} = k_L(V_L/V_B) + (1 - (V_L/V_B))k \tag{6.1}$$

Also, the beads used for the MEGKI layer were exclusively 0.5 mm. And, MEG59 was used for all these cases, and the same protocol which has been described throughout this thesis was used to set up and perform these experiments.

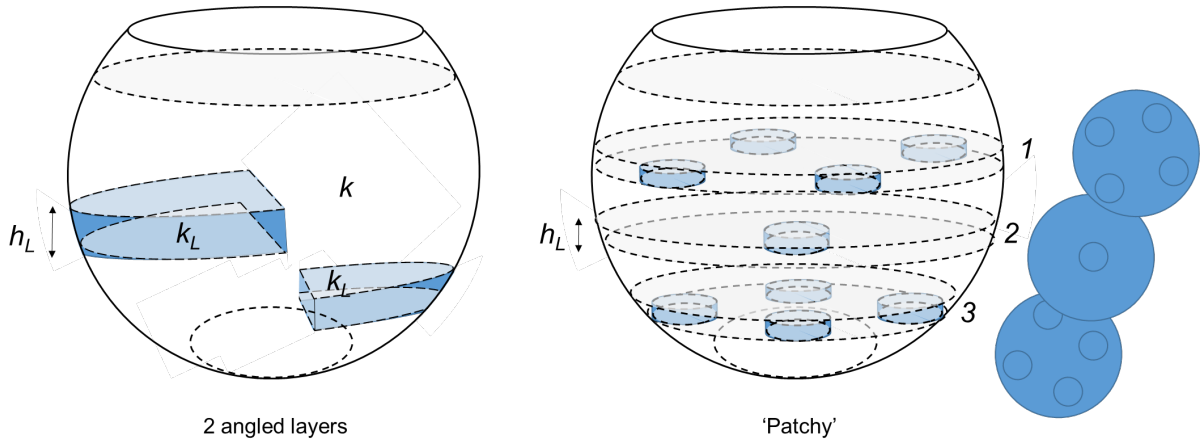

Figure 6.1: Drawing of the experimental geometry with the addition of (left) two angled layers of lower permeability with a layer thickness, $h_L = 1$. (right) is the Patchy configuration where 9 circular patches of lower permeability are introduced. The bowl is packed with soda glass ballotini of differing sizes resulting in different permeabilities of the regions as specified in Table 6.1

6.2 Macroscopic Properties and Reconstructions

6.2.1 MEG Fraction

The analysis begins with a break down of the macroscopic behaviour of the experiments over time. The MEG fraction is calculated and plotted as a function of the square root of time in Figure 6.2 for the discontinuous angled cases with $k/k_L = 25$ (circle symbol), $k/k_L = 4$ (squares), Patchy (triangles) and the Random (inverted triangles). As before the red and blue colouring denotes the top section (red) and bottom section (blue) where the solid line represents the modified logistic fit to the experimental data. Also on this graph is shown the homogeneous case for comparison (+ symbols and dashed line). In Table 6.2 the initial mass of MEG and brine in each experiment is given along with the volume of the top and bottom section and the corresponding error. For all cases, these values are fairly similar showing a good consistency between experiments and the techniques employed to carry them out.

As expected the homogeneous case progress the fastest and represents the upper limit for the dissolution rate. The lower bound is the Random configuration where the flow is slowed considerably. The lateral spread of the fingers due to a decrease in the vertical permeability can explain this as a result of anisotropic conditions. This idea will be explored more thoroughly in the next sections with the reconstructions of the fingers and the development of the finger structures. Looking more at the shape of the curves, unlike

Table 6.2: Summary of experiments reported in this Chapter. The parameters listed in the table have been estimated upon following the procedure described in Chapter 2. M_1 and M_2 are the mass of solution 1 (MEG) and 2 (brine) with estimated uncertainty, σ_{M}; V_{T} and V_{B} are the volumes of the top and bottom sections of the bowl and $\widehat{w}_{\mathrm{B}}(t_{\mathrm{f}})$ is the mass fraction of solute in the bottom section of the bowl at the end of the experiment. For each experiment, $H_{\mathrm{T}} = 3$cm and $H_{\mathrm{B}} = 12$cm.

	M_1 [g]	M_2 [g]	σ_{M} [g]	V_{T} [ml]	V_{B} [ml]	$\widehat{w}_{\mathrm{B}}(t_{\mathrm{f}})$
2 layers $k/k_L = 25$	134.8	823.1	2.57	363.1	2198	0.164
2 layers $k/k_L = 4$	133.32	824.63	2.16	358.86	2203	0.162
Patchy	144.1	813.8	2.07	387.8	2174	0.177
Random	135.1	822.93	2.77	363.0	2198	0.164

Table 6.3: Macroscopic measures of convective mixing extracted from the experiments carried out in this study. Effective diffusion coefficient achieved in the convective regime ($\mathscr{D}_{\mathrm{eff}}$), onset time of convection (t_{c}) and time of convective shutdown (t_{s}). The molecular (bulk) diffusion coefficient takes the value $\mathscr{D} = 1 \times 10^{-5}$ cm^2/s. The parameters and their uncertainties have been obtained using standard relationships for weighted linear regression [83].

	$\mathscr{D}_{\mathrm{eff}}/\mathscr{D}$	t_{c} [min]	t_{s} [min]
2 layers $k/k_L = 25$	45 ± 2	14 ± 3	350 ± 25
2 layers $k/k_L = 4$	52 ± 3	14 ± 4	287 ± 28
Patchy	71 ± 3	19 ± 2	261 ± 11
Random	43 ± 2	30 ± 4	386 ± 22

in Chapter 5, the change of mass follows a similar sigmoid pattern as the homogeneous case because the high permeability zones are always connected, so the transition of MEG is not compartmentalised like in the single layer case.

As shown previously in this Thesis, the early time behaviours ($t^* < 5\ min^{0.5}$) of experiments which use the same fluid pair and bulk permeability (including the homogeneous case) exhibit a convergence in the trend. The onset of convection is determined primarily by the density difference and permeability at the diffusive scale which is similar for all cases. The onset time for each experiment is given in Table 6.3 and from this, it can be observed that there is a good agreement for both the 2 layered cases and the Patchy case as the fluid pair and permeability at the diffusive scale is constant. The onset of the Random case is slightly later because the mixing of the beads results in a lower permeability packing.

Considering now all but the random case between $t^*0 - 8\ min^{0.5}$ all three curves very similar. These results suggest that the onset and initial rate are independent of the heterogeneity configurations (excluding the random case). This is consistent with reports from the literature where only once the plume interacts with the barriers is there a

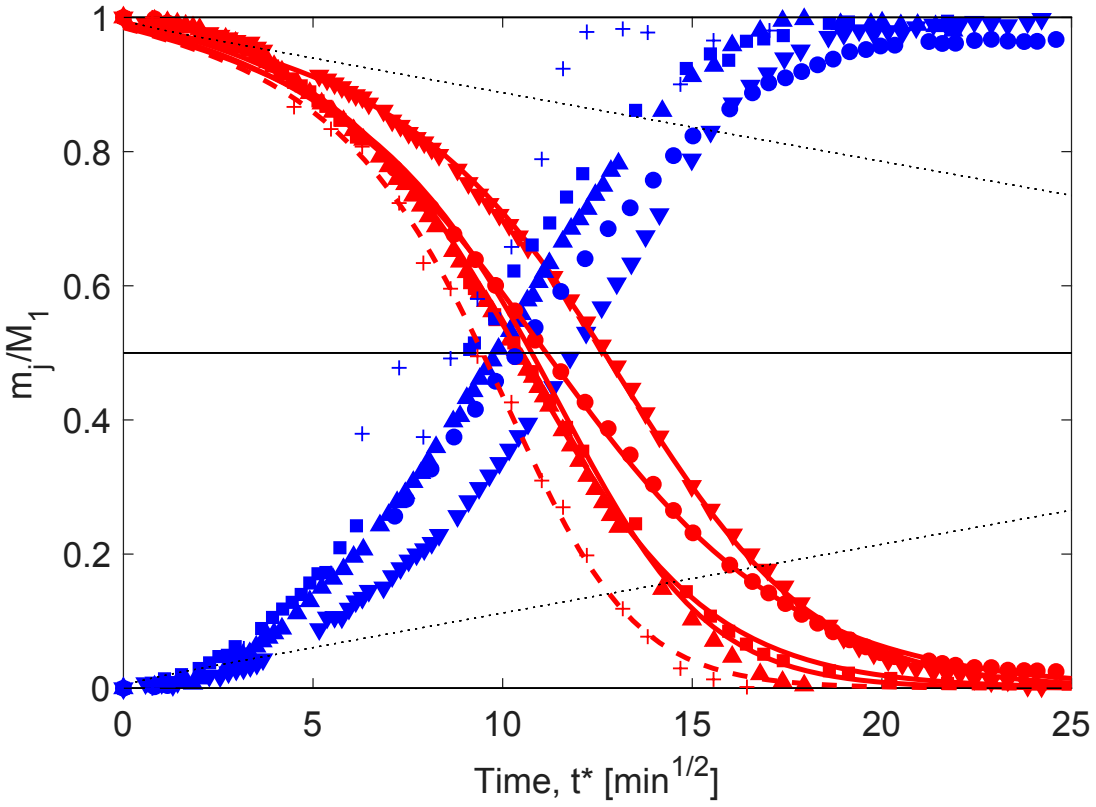

Figure 6.2: Relative mass of MEG dissolved in brine, m_j/M_1, as a function of the square root of time, $t^* = \sqrt{t}$ for experiments conducted with $k/k_L = 25$ (circle symbol), $k/k_L = 4$ (square symbol), Patchy (triangle symbol) and Random (inverted triangle symbol) and homogeneous MEG59 (cross symbol). Colours refer to observations on the top (red) and bottom (blue) sections of the bowl. In each plot, the two sets of dotted curves represent a purely diffusive scenario (straight lines, Eq. 2.7) and modified logistic functions fitted to the experimental data.

divergence from the homogeneous case [60, 67]. After onset the trend in the MEG fraction curve for 2 layers $k/k_L = 25$ diverges from the 2 layer $k/k_L = 4$, and the Patchy cases as the rate slows, and it takes ≈70 min longer for shut down, details given in Table 6.3. However, the Patchy system with a permeability ratio $k/k_L = 25$ continue to closely follows the trend of the 2 layer $k/k_L = 4$. In the literature it has been shown that the vertical permeability independent of how it is increases will have a strong effect on the flux [60, 67, 63, 68]. So for the Patchy the barrier spacing is greater even though the barriers themselves are less permeable as opposed to the $k/k_L = 4$ case where the spacing is small but the barrier is more permeable so the effective vertical permeability is similar. Further work would be needed to understand the exact relationship fully.

6.2.2 Vertical Reconstructions

Figure 6.3 presents the reconstructions of each experiment, most strikingly the flow and evolution of the fingers are considerably different in each of the cases. Here 5 vertical cross sections are shown at different locations through the geometry simultaneously for two different times for each of the four cases.

Looking at each case one by one, first the 2 layers of $k/k_L = 4$ (top right Figure 6.3). Initially, the fingers form uniformly before they interact with the layer and at $t^* = 11.7\ min^{0.5}$ there are still many well-defined fingers, at the later time the layers trap some MEG but in some locations, the fingers have broken through the layers. In this case the plume does not deform around the less permeable layers but instead breaks through at the edges. The flow is not consistent through the geometry as there are regions with many fingers and regions where there is still fresh brine.

In the 2 layers $k/k_L = 25$ (top left), the fingers pool on the first layer very early, and once the fingers come in contact with the layer ($t^* = 12.8\ min^{0.5}$), they are prevented from further downward movement. At $t^* = 23.3\ min^{0.5}$, we observed the plume has saturated about half the bowl, but there is now an upwelling of the less dense brine as shown in the middle cross section at the opening between the layers. This flow structure is likely to be the cause of the slow down of the process as it appears fresh brine impedes the flow of the MEG through the opening. Therefore the barrier spacing is critical, here the layers are close together and causing a bottleneck in the flow behaviour. If the layers are more spread out, like in the Patchy case, there is a completely different behaviour.

In the Patchy case (bottom left) at $t^* = 10.6\ min^{0.5}$ the plume has come in contact with the layers and accumulates on the top of the barriers and in some cases flowing over and around the obstructions. By $t^* = 10.6\ min^{0.5}$ the pooling has resulted in the plume spilling over and saturating most of the domain, but there is also evidence of secondary convective cells and fingers forming on the underneath of some of the patches. This structure is similar to the real mudstone layers in the Sleipner reservoir and could be an indication of the behaviour in the subsurface. This was also suggested in a numerical work [92] on this topic which explored how the presence of discontinuous shale lenses accelerated the convection process and showed that the average breakthrough time of CO_2 at the formation bottom decreases with increasing length of shale lenses.

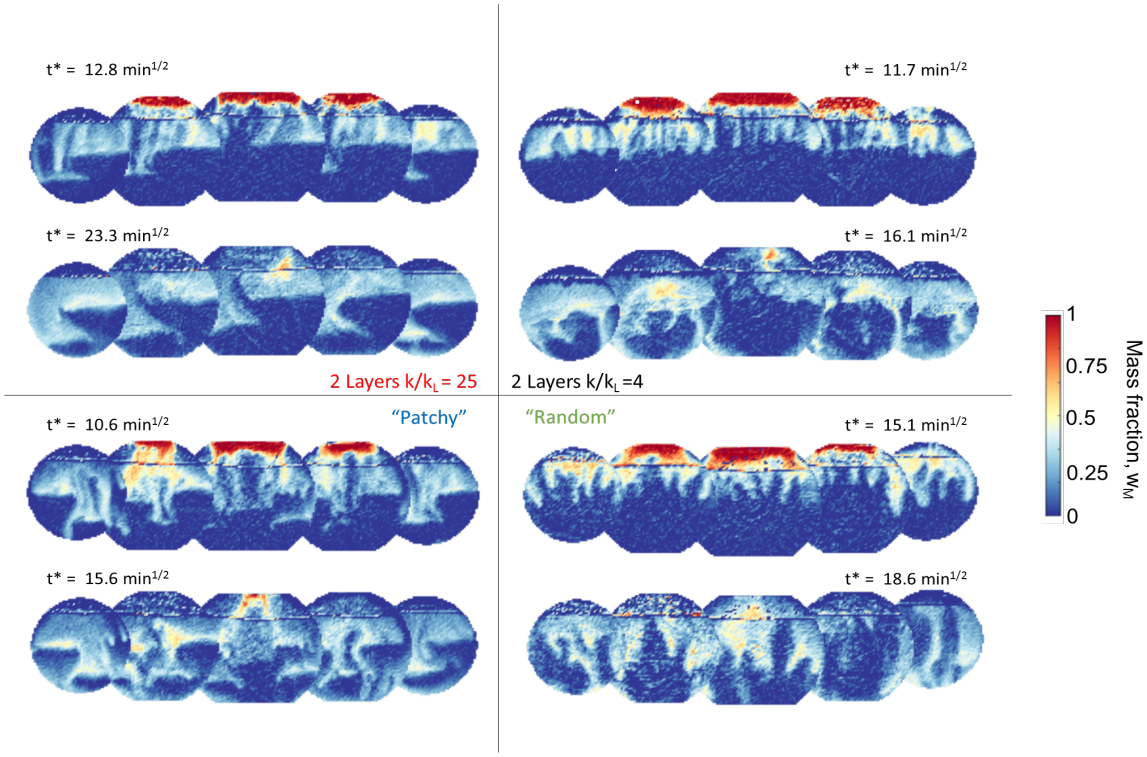

Figure 6.3: Two dimensional reconstruction of each of 2 layer $k/k_L = 25$ (top left), 2 layer $k/k_L = 4$ (top right), Patchy(bottom left) and Random (bottom left) in terms of MEG fraction, $w_i(t)$. Two times are displayed for each experiment where $t^* = \sqrt{t}$ and 5 cross sections are shown overlapping for each time. Voxel dimensions are $(2.4 \times 2.4 \times 1)$ mm^3

The Random case (bottom right) shows that the fingers move and propagate throughout the bowl similar to the homogeneous case but the fingers are more irregular shaped and they exhibit more lateral spreading. Here, dispersion has time to smear out the concentration profiles within the fingers making them appear less well defined. A consistent behaviour with the literature results of anisotropic behaviour which show that when the permeability in the vertical direction is lower than in the horizontal directions the fingers become wider and propagate more slowly. The relative speed of the mixing can be seen in the MEG fraction curves Figure 6.2 between the homogeneous case and the Random where the Random case proceeds more slowly than the homogeneous case.

6.2.3 Horizontally Averaged Concentration Profiles

In Figure 6.4 are presented vertical profiles of the mass fraction of solute, w, at various times and for each case from left to right 2 layer $k/k_L = 25$, 2 layer $k/k_L = 4$, Patchy and

Random. The profiles have been computed using CT numbers in Eq. 2.4 that represent the average of all voxels in each 2.3 mm-thick horizontal section of the bowl. To facilitate comparison between the MEG fraction profiles and the reconstructions the profiles are shown in terms of the square root of time, t^*.

The concentration profiles show some general similarity. When considering the MEG layer for all case, it recedes in a similar fashion with the slow depletion of the layer with the progression of time. The differences lie in the distribution of the solute in the bottom section. From an engineering point of view is essential to understand not only how the MEG/CO_2 is dissolved but also how well it is mixing into the underlying brine. These profiles give a good indication of how this mixing is taking place.

For the 2 layer $k/k_L = 25$, 2 layer $k/k_L = 4$ and the Patchy case the permeability of the layers has a visible impact on the flow. At early times (blue curves) the MEG slowly builds up under the initial interface for each of the cases. As seen in the reconstructions there is an accumulation of MEG at 2-5 cm from the top and then again at 8-10 cm. This trend gives way to an undulating profile (yellow and orange) as the plume interacts with the heterogeneities. The bumps are eventually smoothed out (red curves) but notable for the case where the permeability ratio is lower the final profile is less smooth and retains bumps between 8-12 cm from the top. If this is compared to the reconstructions, it can be observed that some of the MEG remain constrained above the layers with preferential flow paths forming in specific plumes around the layers. The result is some areas containing more pure brine as the heavy MEG sinks to the bottom.

Similar flow structures are observed in the Patchy configuration which is mirrored in the concentration profiles. In general, it can be said that the presence of barrier heterogeneity disrupts the smooth dilution of the plume as it moves downwards and results in areas of the bowl which remain unmixed. However, some build up of material is observed at around 6 cm from the top which is consistent with the laying of the barriers; also this is observed at 9 cm from the top at of point of the lowest barriers.

The trends in the concentration profile of the Random packing is similar to the homogeneous case. The profile does not exhibit bumps or troughs during the experiment, and there is an accumulation of MEG at the bottom of the bowl at late times. Overall this indicates a smooth dilution of the plume for each time however the rate of dilution is slower compared to the homogeneous case.

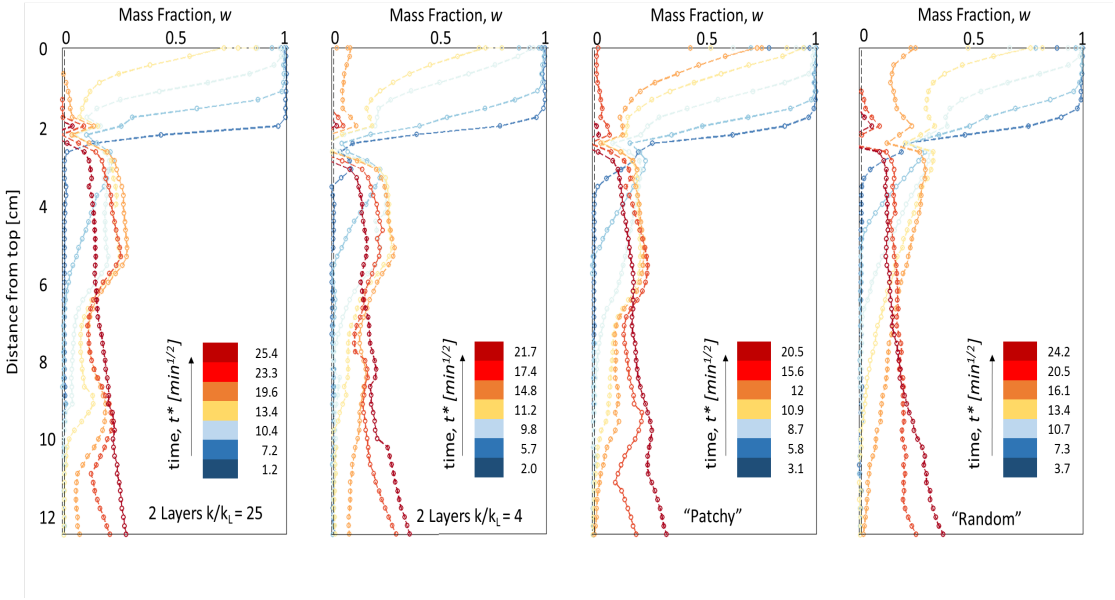

Figure 6.4: Horizontally-averaged profiles of the MEG mass fraction, w, as a function of the distance from the top of the bowl, z. Results are shown for experiments 4 experiments with discontinuous heterogeneity (from left to right: $k/k_L = 25$, $k/k_L = 4$, Patchy and Random). For each scenario, profiles are shown at similar values of the square root of time, $t^* = \sqrt{t}$.

6.3 Extracting a Permeability Map: Random Case

The Random case was designed so that the permeability field within the packing could be monitored independently from the concentration field. By using beads with significantly different attenuation the permeability and the concentration field could be decoupled. The 0.5mm beads (the size used for the homogeneous experiments) saturated in brine have an attenuation of 1170 HU, but the 0.25mm beads have an attenuation of 1630 HU as shown in Figure 6.5 where raw CT images from left to right the 2 layer$k/k_L = 25$, the 2 layer$k/k_L = 4$ Patchy and the Random each of the packing configurations are presented. It is clear from the reconstructions that the layers in the 2 layer$k/k_L = 4$ case are very prominent compared to the 2 layer $k/k_L = 25$ or the Patchy case which also has a ratio k/k_L =25 and contains the 0.1 mm beads as a barrier layer.

The Random packing reconstructions demonstrate that the beads are not perfectly mixed as there are regions of lower and higher attenuation. The blue regions contain more smaller beads than the red regions. The first step to converting the CT units to permeability is to look at the effect of particle mixing on the particle packing quality. One main assumption has been to use the Kozeny-Carman equation to calculate permeability, and this relies on an accurate understanding of porosity. The effect of differing particle diameter on

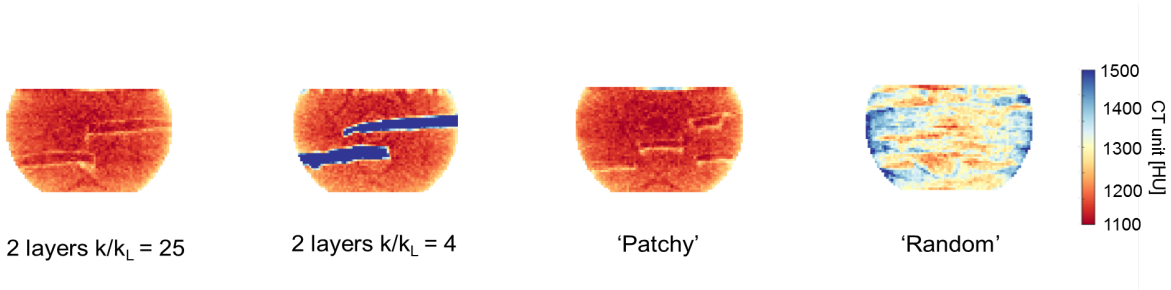

Figure 6.5: Two dimensional reconstructions at t_0 in terms of CT number of a central vertical section of left to right: 2 layer $k/k_L = 25$, 2 layer $k/k_L = 4$, Patchy and Random. Here the MEG layer has been cropped so that only the brine layer is displayed. Voxel dimensions are $(2.4 \times 2.4 \times 1)$ mm^3

bead size has been studied in the literature [93]. When the ratio of the diameter of the small beads, d_s to the larger beads d_l or $d_s/d_l > 0.6$ the effect on the porosity relative to the homogeneous porosity is less than 5%. For the Random case, this ratio is 0.5, and therefore porosity change will be neglected.

The second assumption is that there is a linear correlation between the volume fraction of beads in a voxel and its CT number. So, the CT number of each of the single size bead pack saturated in brine has been established, and the estimated permeability is calculated through kozeny-Carmen, thus, using a straight line a calibration curve can be constructed. Each voxel is then converted directly from the CT unit to permeability.

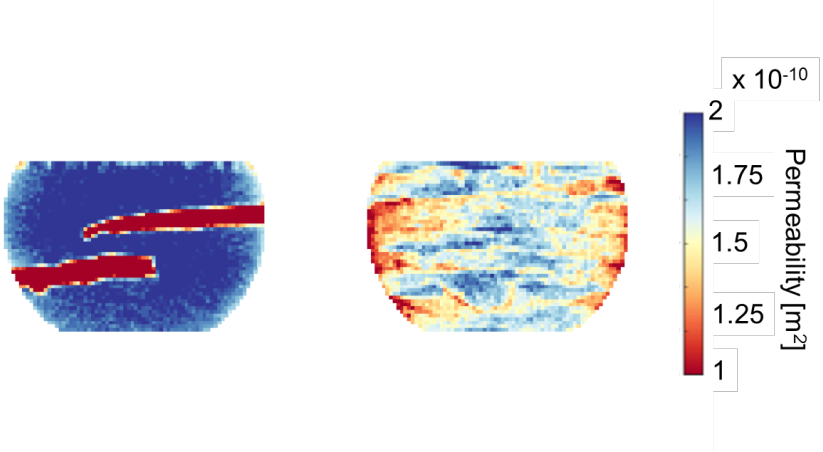

Figure 6.6: Permeability maps of the central vertical slice of (right) 2 layer $k/k_L = 4$, and (left) Random case. Voxel dimensions are $(2.4 \times 2.4 \times 1)$ mm^3

In Figure 6.6 the permeability map is compared for the 2 layer $k/k_L = 4$, and Random case. It can be seen that there areas of lower and higher permeability arranged in striations for the Random case compared to the 2 layered case where the permeability are well segregated. Next, the average permeability for each vertical and each horizontal slice was computed. In Figure 6.7 the results are presented. The blue curve shows the permeability

in each vertical cross-section. There are known beam hardening artefacts at the edges of a sample which may be causing the extremely low permeability at slice 0 and 170. Otherwise, the permeability is an average of $1.5 \times 10^{-10} m^2$. The horizontal slices show by the orange curve indicate an oscillation of the permeability in line with the strata-like observations in the reconstructions.

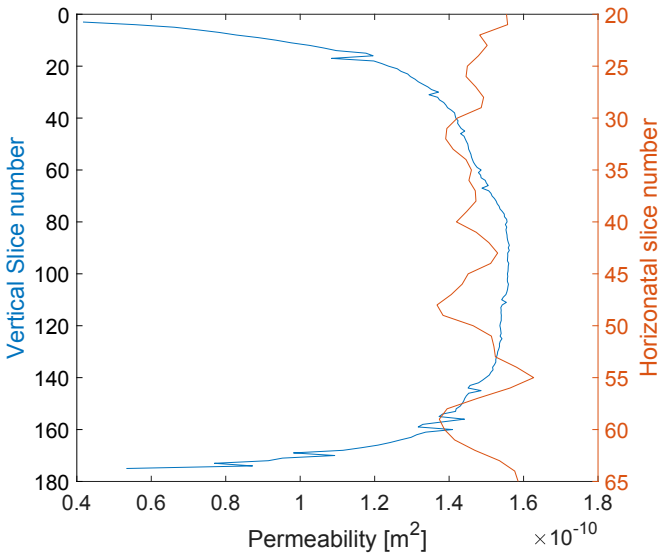

Figure 6.7: Average permeability for each vertical (blue) and each horizontal (orange) slice.

An interesting question is whether there is a correlation between the permeability of a voxel and the concentration in that voxel. By examining the concentration field on a voxel-by-voxel basis, it can be determined if the plume preferentially flowed in the lower or higher permeability zones. In Figure 6.8 concentration vs permeability is mapped for every voxel in the bottom section of a central vertical cross-section for three times, in the beginning, middle and end of the experiment. As mentioned previously, the data on a voxel-by-voxel basis is noisy, and this is why most of the other analysis is done on averaged properties. However, it is possible to get a basic understanding of the relationship between permeability and concentration from Figure 6.8, and it is clear that there is little correlation. Initially at $t^* = 0.58 min^{0.5}$ the cloud of data points is shaped like a mushroom with a distribution around $w = 0$ as only brine is present at this early time in the bottom section of the bowl. In the second graph, the average concentration is increasing at about half the MEG has dissolved into the brine and the point cloud has

shifted towards the higher permeabilities. However the range very large and suggests the data is uncorrelated. Finally at $t^* = 22.4min^{0.5}$ presented the point cloud is evenly distributed around the permeability range and has shifted to the right compared to the initial time as the average concentration at the end is $w \approx 0.2$.

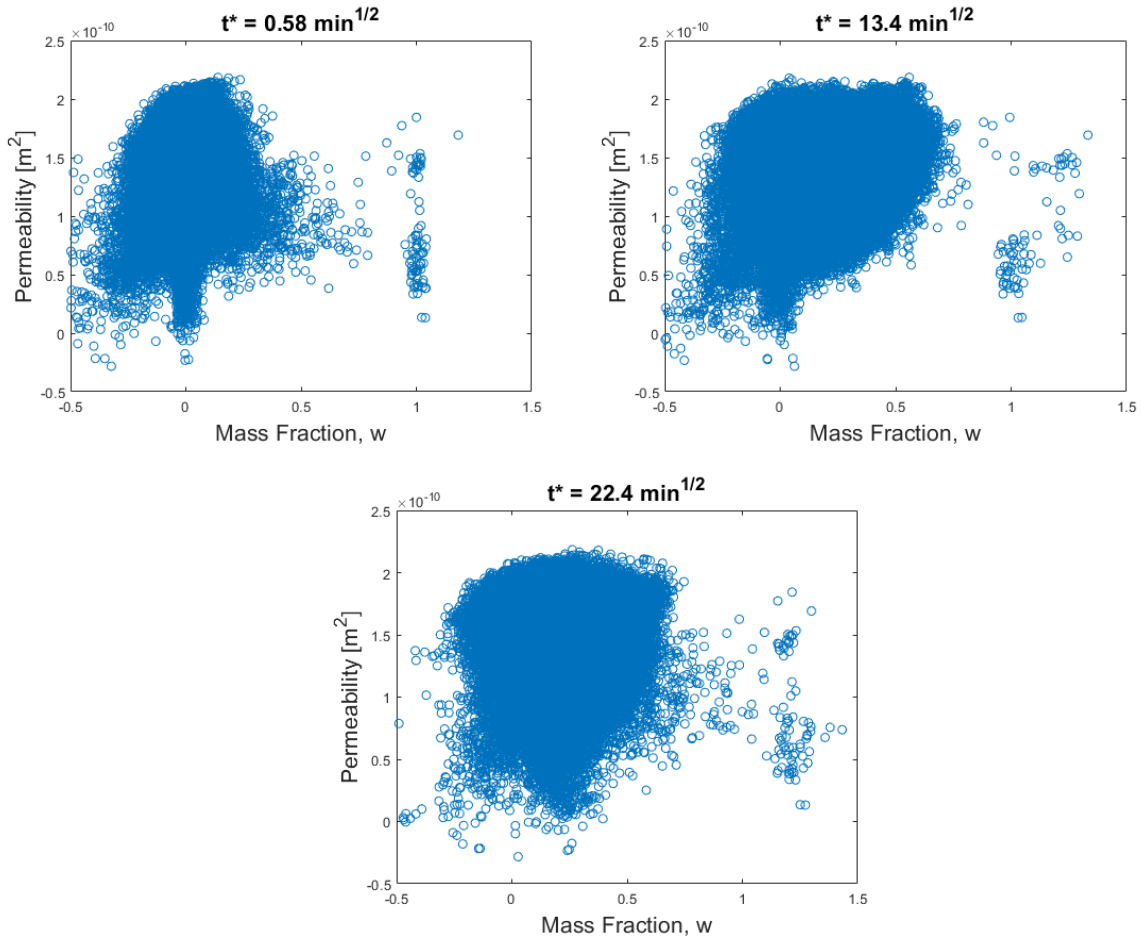

Figure 6.8: Voxel by voxel representation of the permeability against MEG fraction within the central vertical slice shown in Figure 6.5 for the Random packing at three different times.

However, where the heterogeneity does seem to play a role is in the location of the onset for convection. In horizontal (and to a less extent in the vertical) cross sections it can be seen in Figure 6.9 that the fingers form first in areas of higher permeability. In the vertical cross-sections, it is clear that those early flow pathways establish the flow for the remainder of the process and the underlying heterogeneity only acts to smear out the fingers but does not severely alter the flow as observed in the Patchy case. However, this is just one data set, and these findings may not be representative of the flow in other mixed bead systems. The primary outcome then is that it shows that it is possible to

extract a permeability field from the attenuation.

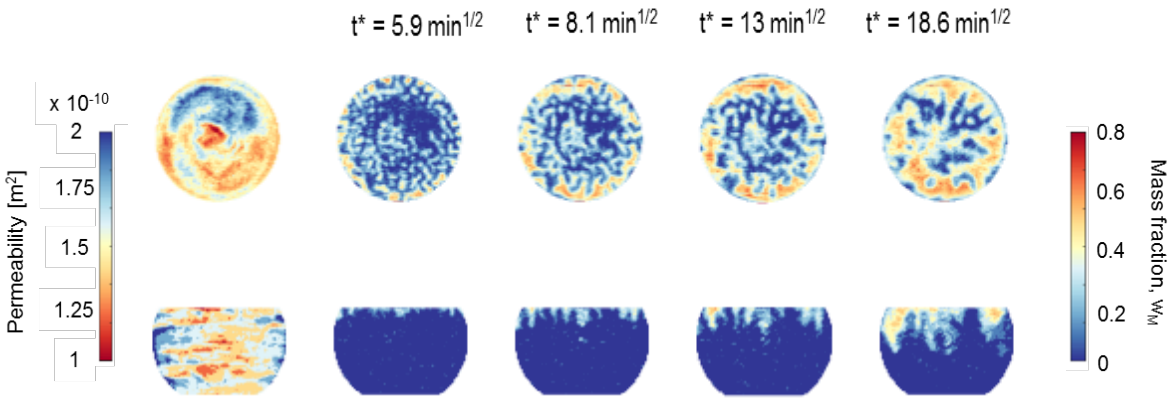

Figure 6.9: Horizontal two dimensional reconstructions at 2.5cm below the initial interface in terms of permeability (left) and in terms of MEG fraction for four increase times where $t^* = \sqrt{t}$. Voxel dimensions are $(2.4 \times 2.4 \times 1)$ mm^3 and the images are presented as contour lines of either permeability or constant MEG mass fraction, $w_i(t)$

6.4 Dissolution Rate and $Sh - Ra$ Comparison

As in previous Chapters, the dissolution rate is calculated using the differential of the fit to the experiential data shown in Figure 6.2. As Chapter 3 outlines many realisations of the fitted curve are differentiated then averaged to produced the curves shown in Figure 6.10 for the 4 experiments 2 layer $k/k_L = 25$ (red), 2 layer $k/k_L = 4$ (black), Patchy (blue) and Random (green) described in this Chapter along with the homogeneous MEG59 case for comparison (dashed black). The purely diffusive curve is also plotted (solid black).

The shape of the flux curves are similar for all cases, and initially, they follow a trend congruent with the diffusion model before they gradually diverge at the onset of convection and reaching a peak. The height and timing of this peak are unique for each case. As expected the homogeneous case is the fastest and has the largest maximum flux where $r_{\max} = 0.61 \pm 0.11$ g/min (MEG59 at 74 min) of all the experiments reported in this Chapter. The introduction of heterogeneity has a two-fold impact on the rate. In general with the addition of heterogeneity it is observed that the curves reach a) a lower maximum flux and b) at later times as estimated as $r_{\max} = 0.39 \pm 0.02$ g/min (2 layer $k/k_L = 25$, at 84 min), $r_{\max} = 0.50 \pm 0.03$ g/min (2 layer $k/k_L = 4$ at 91 min), $r_{\max} = 0.48 \pm 0.02$ g/min (Patchy at 105 min) and for the Random case $r_{\max} = 0.35 \pm 0.02$ g/min at 190 min which is

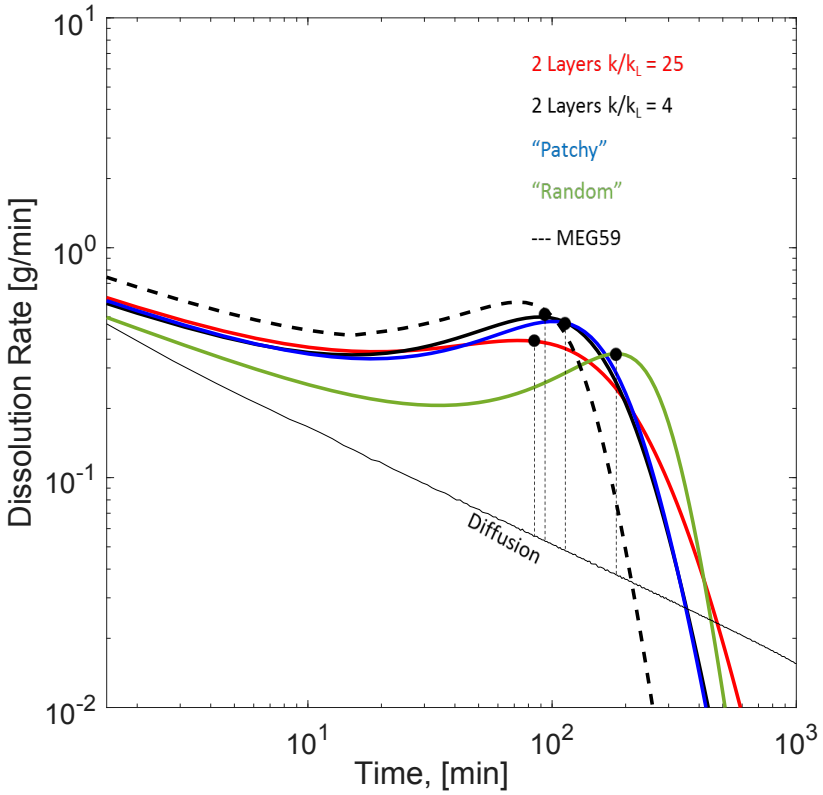

Figure 6.10: Average rate of dissolution as a function of time for the $k/k_L = 25$ (red), $k/k_L = 4$ (black), Patchy (blue) and Random(green) and homogeneous MEG59 (dashed black) obtained upon differentiating the modified logistic function fitted to the experimental data (Figure 6.2), while the dotted black line is the numerical solution of the purely diffusive scenario (Chapter 2) The cross symbols are the rate of dissolution at the time of the onset of convection (estimated from Figure 6.2), while the circles represent the time at which the maximum rate of dissolution is attained.

approximately 100 min slower than the other cases. The timing of the maximum rate and $r_{\max}$ itself is very similar to the homogeneous MEG55 case presented in Chapter 3 where $r_{\max} = 0.37 \pm 0.06$ g/min at 186 min. However, for the Random, 2 layered and Patchy configurations the time of the maximum flux is consistently six times larger than the time for the onset of convection, i.e. $t(r_{\max}) \approx 6t_c$. For the homogeneous cases, $t(r_{\max}) \approx 4t_c$ indicating that the presence of heterogeneity in these specific cases in increasing the time taken after the onset of convection to reach a maximum flux compared to the homogeneous case.

Interestingly if the result from Chapter 5 is also compared where $t(r_{\max}) \approx 3.5t_c$, it suggests that the presence of discontinuous heterogeneity has the most significant effect on the time between onset and maximum flux. The continuous barrier layer had timing similar too and within the error of the homogeneous case but the discontinuous case is

systematically increasing this time. In most reservoir settings the types of heterogeneity will be discontinuous, so this is an important metric to understand them and predict the total dissolution of CO_2.

Another comparison is to quantify by how much the presence of heterogeneity decreases the maximum flux. Comparing the absolute value of the maximum flux, the presence of heterogeneity decreases the flux by 35% for 2 layer $k/k_L = 25$, 18% for 2 layer $k/k_L = 4$, 22% for Patchy and 43% for the Random case. However, a better comparison would be the relative enhancement by convection ($r_{\max}/r_{\mathscr{D}}$) and the decrease in this enhancement compared to the homogeneous case is $\approx 20\%$ for 2 layer $k/k_L = 4$, Patchy and Random and $\approx 40\%$ for 2 layer $k/k_L = 25$. Therefore, all through the presence of heterogeneity is decreasing the absolute value of the maximum flux the relative increase compared to the diffusive case is still significant.

The relative increase can also be compared via the Sherwood number by scaling the enhancement by a length scale. Here $l_{\mathrm{H}} = 10$ cm $\approx H_{\mathrm{B}}$ is the characteristic length scale of convective mixing, while $l_{\mathscr{D}} \approx 1 - 2$ cm is the corresponding value associated with the diffusive process. The Sherwood number is calculated and plotted against Ra in Figure 6.11 for experiments reported in this Chapter(blue circles) alongside the data collected from the single-layered case (orange and purple circles) as presented in Chapter 5 and the homogeneous experiments(black circles) as presented in Chapter 3. A linear trend emerges between the Sh and Ra where $Sh = 0.0236Ra$ which is extremely close to the relationship derived solely from the homogeneous experiments where $Sh = 0.025Ra$. This scaling is an extremely encouraging and novel result, here is presented many independently run experiments that have culminated in a trend that is very close to the theoretical linear result and so proves the validity of the experimental procedure.

Looking more closely at each experimental data, the majority of the points are for $Ra = 2000 - 4000$ and within this range there is also a broad range of Sherwood, $Sh = 50 - 100$, for the experiments presented in this Chapter (blue points) the points are clustered about $Sh = 80$ which is similar to the purple points from the single-layered case with the same bulk permeability. Notably, these show that for a given Ra the Sh is higher for examples with permeability heterogeneity than the corresponding homogeneous case. However, those homogeneous points are calculated based on experiments with different fluid pairs and, as discussed previously the density profile has been reported to

influence the mixing behaviour [40]. Interestingly, none of the heterogeneous tests which were conducted with MEG59, fall outside the upper limit of the *Sh* range given by the homogeneous experiment which used MEG59.

The points which fall outside of the $Ra = 2000 - 4000$ zone indicate that the linear trend may extends over the entire range of *Ra*, thus the maximum rate of dissolution is related to by the average vertical permeability. This has also been reported in the literature in studies with barrier heterogeneity where the width and spacing of the barriers were varied [68, 67].

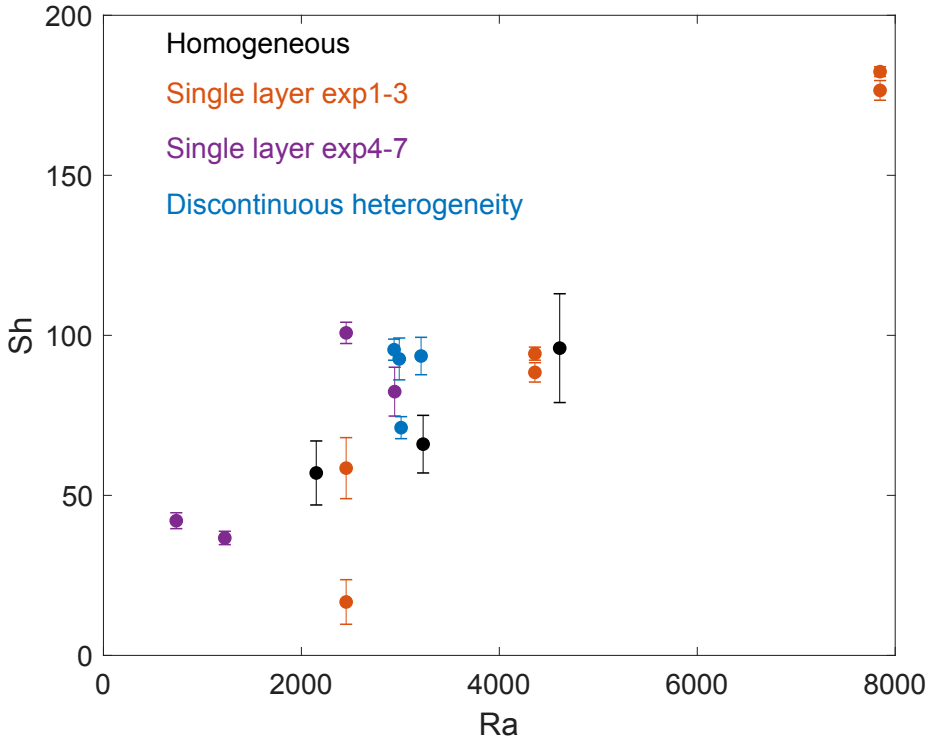

Figure 6.11: Convective mass flux plotted in terms of Sherwood number, *Sh* calculated by the scaled ratio of the maximum dissolution rates (Eq. 3.2) as a function of the Rayleigh number, *Ra*. Results have been compiled for four experimental sets, and the homogeneous experiments(black circles) as presented in Chapter 3, the single layered case (orange and purple circles) as presented in Chapter 5 and the results reported in this Chapter (blue circles)

6.5 Summary

In this Chapter, a series of increasingly complex discontinuous heterogeneities have been studied to assess the impact on density-driven convection via an X-ray CT imaging

protocol. Three configurations of heterogeneity were considered; 2 disconnected angled layers, chequerboard-style patches of lower permeability and a random uncorrelated heterogeneous packing. For each case, the macroscopic measures of mixing such as the average concentration profile and dissolution rate were presented. Reconstructions revealed concentration structures unique to each configuration, pooling, merging and secondary fingers were observed along with an increase in lateral mixing in some cases. A permeability map was obtained for the Random case which revealed that the flow of MEG or brine did not have a preferential flow path determined by the permeability, but it was observed that fingers formed more frequently in areas of higher permeability.

Surprisingly, the trend for experiments with different configurations and differing permeability ratios had almost identical trends in the dissolution rate. The reconstructions hint at an explanation that this trend is a result of the spacing between the barriers. If the spacing is large, the plume is more connection, and this results in a higher flux as, for example, in the Patchy case there is sufficient space surrounding the layers for the fingers to meander through. But if the spacing is small, then the flow becomes restricted, and this slows down the overall behaviour as shown in the 2 layer $k/k_L = 25$. A third behaviour was observed where the layer was permeable enough to allow the plume to break through the layer at various points instead of material pooling at the interface. The similarities observed in the trend between the 2 layer $k/k_L = 4$ and the Patchy case seems to be a result of different mechanisms culminating in the same effect. The final conclusion of this work was to analysis of all the experiments conducted in this Chapter and Chapter 3 & 5 with a comprehensive $Sh - Ra$ plot. This plot supports the scaling initially determined in Chapter 3 as here it is found to be $Sh = 0.0236Ra$.

Chapter 7

2D Modelling Study of Convective Dissolution using COMSOL

7.1 Introduction

So far the results presented in this thesis have been exclusively experimental. Eventually, the aim was to develop a simplified rapid model that could guide experimental development and extend the range of parameters that could be explored in the experiments. In particular, and as described in Chapter 5 and 6, natural rock heterogeneity will be a key factor in the formation and propagation of the fingering phenomena. In this Chapter, we present a modelling approach using a commercially available software, COMSOL, to investigate the influence of simple heterogeneities similar those implemented in Chapter 5 and 6 in a 2D geometry with the measured fluid properties of the MEG-water system.

As outlined in Chapter 1, numerous numerical works have focused on the phenomenon of convective dissolution with a focus on the initial onset of instability or the onset of convection, but only few with the goal of evaluating mixing [30, 58, 8, 25, 94]. These authors use a range of methods from direct numerical simulation, linear stability analysis with finite volume or finite element schemes in a 2D and 3D homogeneous or heterogeneous systems. However, only one study [21] uses the same fluid pair as is used in the experiments presented in this Thesis. To fill this gap, a new model was developed which is computationally efficient and easily modified to include small and large scale heterogeneities. The initial conditions are consistent with the experimental set up and the model accurately represents

the receding interface as observed in the experiments.

7.2 The Model

7.2.1 Governing Equations

In this Chapter, a 2D version of a model originally developed by Jiajun Cen as part of his PhD project was modified to investigate the effects of permeability heterogeneity. The finite element COMSOL Multiphysics model employs the real measured fluid properties of the MEG-water system as described in Chapter 2. A sketch of the system is shown in Figure 7.1 where the height of the initial MEG reservoir, H_T, is 0.015 m and the height of the bottom domain, H_B initially filled with water is 0.085 m so, the total height of the system is 0.1 m and the width, W, is 0.0 5m. The simulation was built using two physics modules, transport of concentrated species (tcs) and laminar flow through porous media (spf) which are coupled using the reacting flow module.

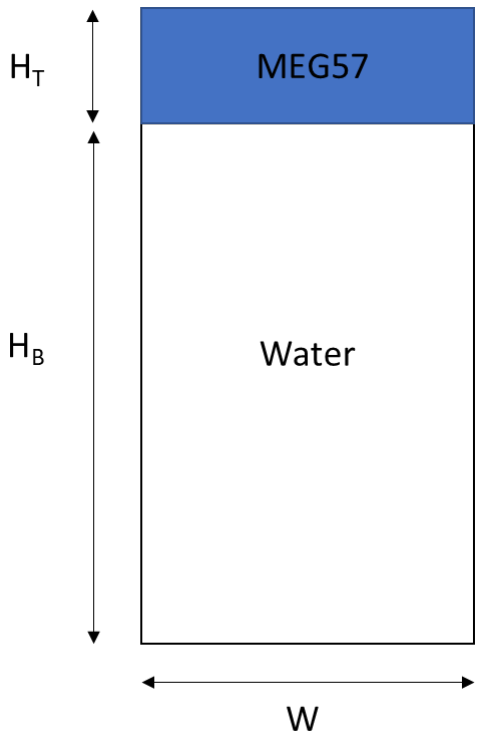

Figure 7.1: Sketch of the 2D geometry used in the COMSOL simulations indicating the width, W and height of the initial top domain, H_T, containing pure MEG57 and the bottom domain, H_B, containing pure water with a height.

Incompressible fluid flow in a porous medium can be described using the conservation of momentum equation:

$$\phi\frac{\partial p}{\partial t} + \nabla.(\rho\mathbf{u}) = 0 \tag{7.1}$$

and Darcy's law as described in Chapter 1 1.2. In the results presented in this Chapter only isotropic porous media are considered thus a single value for permeability is used. Finally, the transport of solutes is described using the conservation of mass equation:

$$\phi\frac{\partial \rho x_i}{\partial t} + \nabla.(\boldsymbol{j_i}) + \mathbf{u}.\nabla.(\rho x_i) = 0 \tag{7.2}$$

The local density ρ multiplied by the local mass fraction x_i gives the local concentration of species i is defined as: $C_i(x; t) = \rho(x_i)x_i(x, t)$. $\mathbf{j}_i$ in Equation 7.2 is the flux vector of species i.

The tcs module employs a mixture-averaged diffusion model which essentially solves Equation 7.2 with $\mathbf{j}_i = -\phi D_i \nabla \rho x_i$ which when the Mixture averaged diffusion model is applied results in Equation 7.3.

$$\boldsymbol{j_i} = -\phi D_i \nabla \rho x_i + D_i \rho x_i \frac{\nabla M_n}{M_n} \tag{7.3}$$

where

$$M_n = \sum_i (\frac{x_i}{M_i})^{-1} \tag{7.4}$$

Here, D_i is the diffusion coefficient and for simplicity it is assumed this is the same for both fluids and M_i is the molar weight of species i. In the spf module, the porous media option is enabled, the flow is defined as incompressible and volume forces are applied also hydrodynamic dispersion is neglected here. At t = 0 the top domain has a mass fraction of 1 and the bottom domain a MEG fraction of 0. All boundaries have a no-flux and no-slip condition.

7.2.2 Perturbation Field, Meshing and other Solver Settings

To initiate the development of density fingering, the concentration field at the initial MEG-water interface must be perturbed numerically. The usual method is to use a

concentration perturbation [11], but here we use a spatial perturbation; this is achieved by creating a parametric curve for the 2D case. The amplitude of this spatial disturbance, A_m is kept constant and is reported in Table 7.1. This parameter has been tuned to avoid any influence on the ultimate wavelength of the finger formation. Thus, the model has been constructed in such as way that it allows for the formation of the density fingers without numerically manipulating the concentration field.

The meshing has triangular elements where the maximum and minimum element size, the element growth rate, curvature factor and meshing resolution of the narrow region is controlled. At the boundaries, the fine elements and corner refinements are applied. Then, the MUMPS direct solver is used and is fully coupled. Also, dependent variables such as mass fraction and fluid velocity are evaluated with a strict time stepping method where the relative tolerance is 0.01 with a maximum of 0.5 min.

Two additional factors have to be accounted for in the model (i) the top boundary is somewhat deformable to compensate for the slight volumetric change due to the monotonic mixing curve and (ii) COMSOL uses an artificially rapid numerical diffusion to help stability in the convective transport solver and this results in a spurious maximum in the early time flux. This can be minimised by incrementally increasing gravity at the start of the simulation. Further details of this, and all other aspects of the model can be found the the thesis of Jiajun Cen.

7.3 Homogeneous Case

To systematically analyses the effect of heterogeneity, it is useful to first evaluate the homogeneous case to establish a baseline. An isotropic permeability field is implemented where the absolute permeability is correlated to specific particle size via the Kozeny Carmen equation as outlined in Chapter 2. For direct comparison, the particle size is within the range which is possible experimentally, i.e. 0.2 - 2 mm and are detailed in Table 7.2. Otherwise the domain size, fluid pair and perturbation are kept the same as detailed in Section 7.2. The purely diffusive case is also simulated.

By varying the permeability we are by extension examining the Ra range of 400 - 40,000 which is also outlined in Table 7.2. The terms used in the Ra calculated are given in Table 7.1.

Table 7.1: Key input parameters.

Parameter	Symbol	Value	Units
Domain			
Length	L	0.05	m
Height	H	0.1	m
Height of initial MEG layer	H_T	0.85H	m
Amplitude of spatial disturbance	A_m	0.4	mm
Porosity	ϕ	0.36	-
Permeability	k	see Table 7.2	m^2
Sphericity of the bead packing	Φ	1	
Bead diameter	d_p	0.2-2	mm
Gravitational acceleration constant	g	9.81	m/s^2
Ambient conditions			
Pressure	P_0	1	atm
Temperature	T_0	293.15	K
Fluid Properties			
Molar weight of MEG	M_{MEG}	50.95	g/mol
Molar weight of water	M_{MEG}	18.02	g/mol
Initial mass fraction of MEG	x_{MEG}(t=0)	1	-
Viscosity of water	μ_2	1.058	mPas.s
Maximum Density Difference	$\Delta\rho$	6.5	g/cm^3
Diffusion Coefficient	$\mathscr{D}$	1.2x10^9	m^2/s
Meshing			
Max. element size	-	3	mm
Min. element size	-	$2A_m$	mm
Max. element growth rate	-	1.3	-
Curvature factor	-	0.7	-
Resolution of narrow regions	-	0.6	-

The results are presented directly as the dissolution rate which was calculated in a similar manner to the experiments as the rate of accumulation of MEG in the bottom domain over time, but unlike in the experiments, this can be calculated directly from the simulation. Then a new metric is introduced the dilution index,E, which is an important measure of mixing as it evaluates the volume of the domain, V, when subdivided into discrete elements occupied with a particular solute [95], the equation is as follows:

$$E = \Delta V \exp[-\Sigma P_k \ln(P_k)] \tag{7.5}$$

Table 7.2: List of bead diameters, dp, used in this study with the corresponding permeability, k, and Rayleigh number, *Ra*.

dp [mm]	k [m^2]	*Ra*
0.2	4.75×10^{-11}	563
0.3	9.30×10^{-11}	1103
0.4	1.54×10^{-10}	1824
0.5	1.90×10^{-10}	2251
0.75	4.27×10^{-10}	5065
1	7.59×10^{-10}	9005
2	3.04×10^{-9}	36020

P_k is the ratio of mass in an element divided by the total mass, P_k can be understood as a probability that a bin contains solute. It is useful to normalise the dilution index by the maximum dilution index, E_{Max} which is simply the volume of the domain. By normalising this by the volume of the domain, E_{Max}, the percentage of the volume which is occupied by solute can be determined. The E factor and is a theoretical upper bound to which everything will be scaled. So, as t $\rightarrow$ inf then $E/E_{Max} \rightarrow 1$ indicates the domain is completely mixed. In these simulations t = 0 then $E/E_{Max} = 0.15$ which is the fraction of the domain initially occupied by MEG.

As before qualitative and semi-qualitative analysis will be performed using the discrete-time images which COMSOL provides.

7.3.1 Results

In Figure 7.2 is shown the dissolution rate as a function of time for the 8 cases run with a homogeneous permeability equivalent to a bead pack with a particle diameter of 0.2-2 mm with the addition of the purely diffusive case. As expected the simulation with the largest bead size (2 mm, red) has the highest rate at the earliest time, and the overall rate is slower and lower as the bead size is decreased (red to blue). Interestingly, each curve has a unique trajectory. Therefore performing experiments and simulations in the relevant *Ra* range to the application is essential.

In this study, the range of *Ra* is controlled through the permeability, k, and thus the bead size of the packing, dp. If the porous medium is highly resistive to fluid flow with a permeability that is low enough (0.2 mm case), the spatial perturbation introduced at the

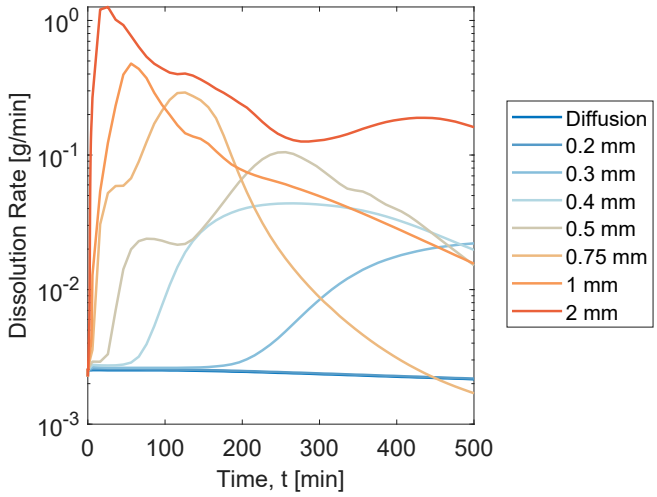

Figure 7.2: Dissolution rate as a function of time for each of the homogeneous simulations with permeabilities equivalent to random bead pack of particles with diameter 0.2 - 2 mm. The purely diffusive case is also presented for comparison.

initial fluid-fluid interface will be dampened. In Figure 7.2 it is observed that the 0.2 mm case closely resembles diffusion and indicates that here the interface remains stable and gradually descends to the bottom of the domain without the onset of convection. The other two blue curves, 0.3 mm and 0.4 mm, initially follow the diffusive scenario before diverging at the onset of convection with gradually increasing rates of dissolution. In the 0.4 mm case the onset of convection is 106 min faster than 0.3 mm case. Thereafter, in the more permeable simulation, the ensuing rate of dissolution is more rapid.

By also comparing the mass fraction images over time we can visualise the transition from a purely diffusive regime to the convective regime. In Figure 7.3, the first row of images represents the evolution of the fingers for the 0.4 mm case. From 4-26 min we see diffusion smearing out the front, then perturbations grow and becoming more evident as convection takes over. This behaviour can be tracked in the rate curve as by 166 min an almost constant rate period has been reached which characterises the growth regime of the fingers. The appearance of a constant rate period at low Ra and not high Ra is contrary to results reported previously [56, 11] and this suggests that it is not a constant rate but instead a wide maximum.

Looking at the rate curves for the 0.5 mm case, in Figure 7.2, this also briefly follows the diffusive curve but diverges after only 26 min after that we observe two distinct peaks in the trend, the second showing a clear maximum in the rate at 256 min. After which there

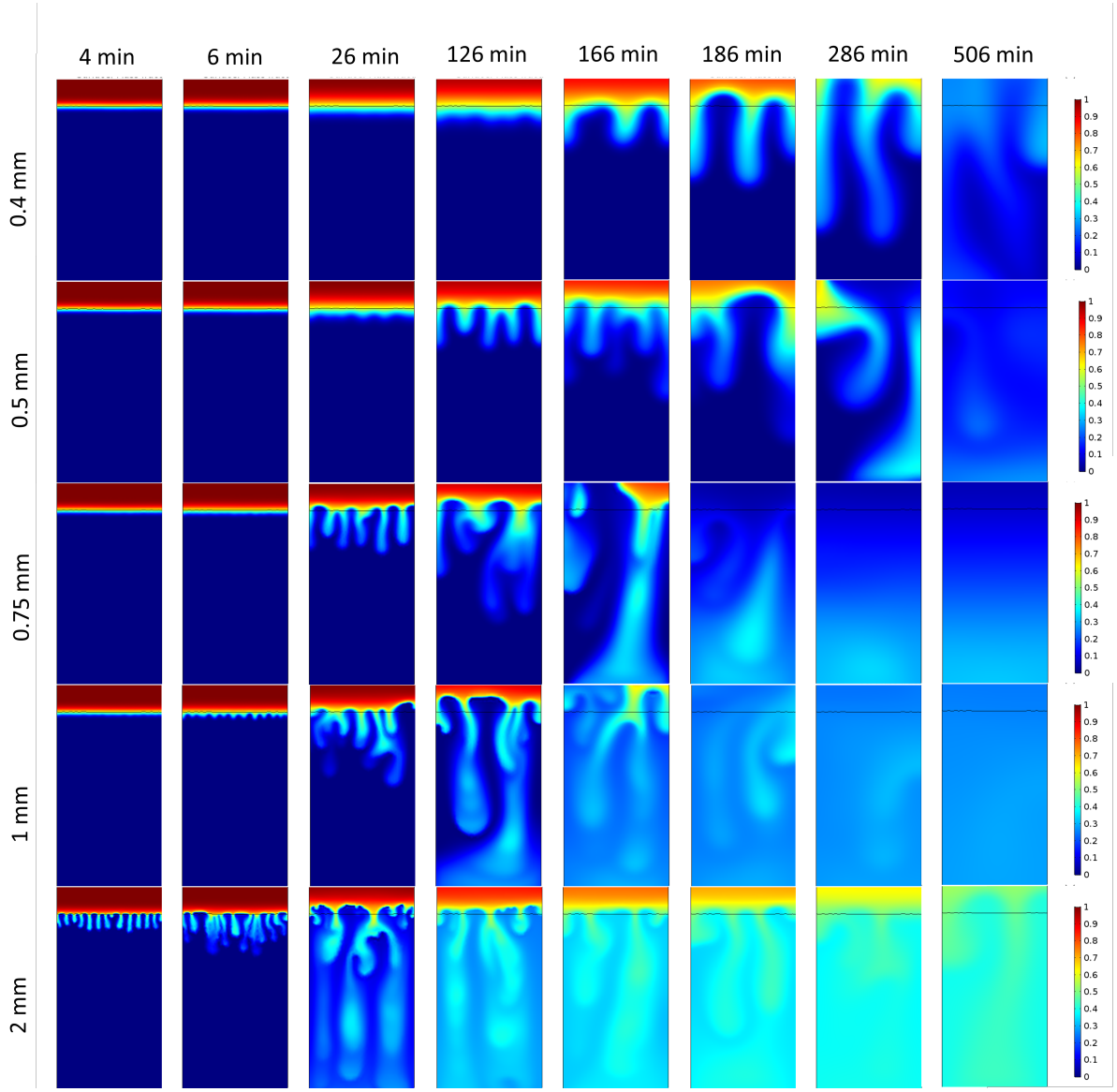

Figure 7.3: Discreet images for 8 times during the simulation in terms of mass fraction for simulations with a permeability equivalent to a packing of beads with particle size 0.4, 0.5, 0.75, 1 and 2 mm.

a few smaller bumps as the rate falls steadily. From Figure 7.3 it is not completely clear why there is a double peak, but it can be speculated that the first peak corresponds to the onset of convection and the second is related to the subsequent break up of the MEG layer into two separate plumes. Between 186 and 286 min, the MEG layer is split into two sections by the upwelling of fresh water. The plume on the right-hand side has slipped down the wall and has pooled at the bottom. The left-hand plume is surrounded by water from three sides thus increasing the rate of dissolution. The unique mixing pattern could explain the second and later increase in the rate of dissolution.

The 0.75 mm case is set apart from the other particle sizes as the rate curve goes through

a maximum and then quickly and immediately drops off. This rapid decrease in the rate indicates that the shutdown occurs much faster in this case than in any of the other cases. From the mass fractions plots, we see that the plume pools at the bottom of the domain quickly which is the cause of the shutdown of convection and creates a segregated situation where mixing is incomplete. This behaviour is also observed in the experiments which are performed at similar Ra (~ 5000).

The 1 and 2 mm results are initially very similar, albeit the 2 mm cases progresses faster, the rate of dissolution peaks sharply before gradually decreasing. We observe many small fingers form in Figure 7.3 after which the plume quickly fills the entire domain. For these two cases, we also find that the fingertips branch-off from the main finger body and travels more rapidly to the bottom of the domain. However, after 256 min there is a divergence in the trend of the rate curve, the 1 mm case continues to decrease as convection shuts down, but in the 2 mm case, there is a secondary increase in the rate. The double peak can be explained by understanding the underlying physics of the MEG-water mixing curve. In the 2 mm case convection happens so fast the bottom domain is quickly filled with MEG, and the average mass fraction is ≈ 0.4. However, the top layer now has an average mass fraction ≈ 0.7. Due to the non-linearity in the mixing curve, the bottom domain is now on average more dense than the top domain, and a stable situation has been reached. Only after 300 min does convection begin again after the proper density contrast has been re-established.

7.3.2 Discussion of Mixing Potential

In general, the higher Ra, the more quickly the density fingers travel to the bottom of the domain. However, a higher Ra does not necessarily mean better mixing across the whole domain. The normalised dilution index quantifies the mixing state and the curve for each of the 8 cases is presented in Figure 7.4 as a function of time coloured from blue to red for increasing particle diameter.

Interestingly the 0.5 mm case reaches a higher index of dilution before the 0.75 mm case, and this is because for the higher permeability case the plume is moving so fast that it pools, unmixed at the bottom of the domain. This behaviour explains the apparent plateau in the dilution index as only with time will this accumulated MEG spread across

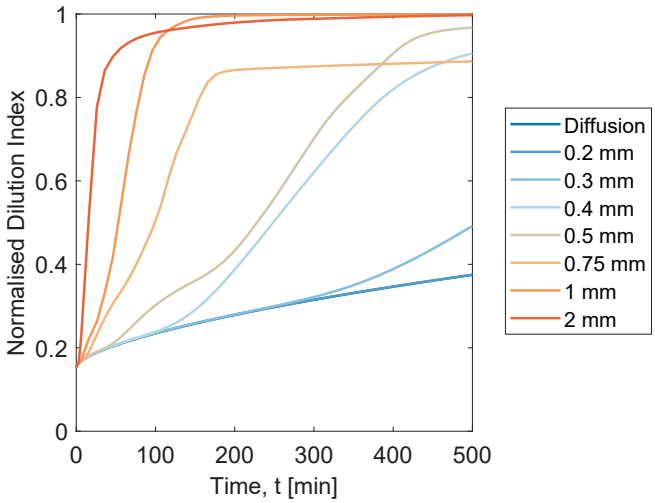

Figure 7.4: Normalised dilution index as a function of time for each of the homogeneous simulations with permeabilities equivalent to random bead pack of particles with diameter 0.2 - 2 mm. The purely diffusive case is also presented for comparison.

the whole domain through diffusion. The 0.5 and 1 mm cases result (although at different rates) have an index close to 1 and an almost uniform concentration across the whole domain, as observed in Figure 7.3.

To summarise, a parametric sweep has been conducted to evaluate the finger structure and quantify the mixing behaviours across a range of Ra. The dissolution rate and dilution index were evaluated to and it was found that mixing potential is not linear correlated with increasing Ra.

7.3.3 Scaling Behaviour

The final analysis performed on this data set is to compare the Sherwood to Rayleigh numbers. We extract the Sh in the same manner as described for the experiments where the maximum rate is compared to the diffusive rate. The resultant Sh is plotted against Ra and presented in Figure 7.5. Here is shown the Ra range 0 - 10,000. In that range there are six simulations equivalent to $d_p = 0.2$ -1 mm and a linear trend emerges that can be described by $Sh = 0.022Ra$. From the experimental data, a very similar scaling emerges where $Sh = 0.025Ra$. This similarity is a particularly important result as for the first time 2D simulations and 3D experiments that have been conducted in the same Ra range with the accurate fluid pair behaviour are yielding almost identical scaling behaviours.

The similar scaling behaviour observed between the simulations and experiments somewhat

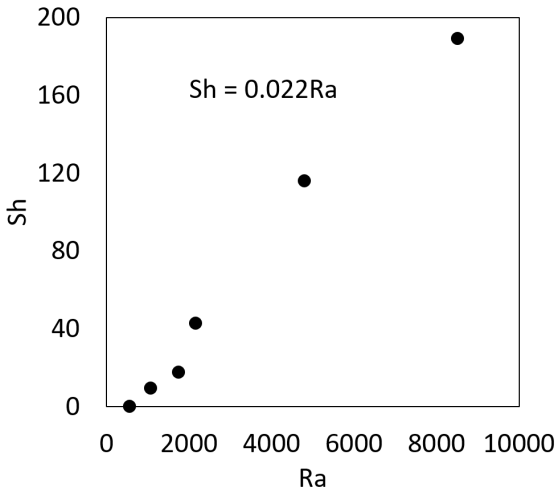

Figure 7.5: Sherwood-Rayleigh plot for the homogeneous simulations in the range of *Ra* 0 - 10,000 with the equation for the linear trend that can describe this data.

contradicts the earlier argument that the process in 3D is different from that in 2D. However, in the experiments the substantial error bars precludes detailed comparison of the linear relationship and interestingly the *Sh* reported in the experiments is significantly larger for the overlapping *Ra* range in the simulations. So it could be coincidental that the scaling converges but it is definitely a comparison worth exploring further.

7.4 Single Layer: Horizontal vs Angled

A simple form of heterogeneity is a single layer of lower or higher permeability, similar to the study performed in Chapter 5 the Impedance as shown in Equation 5.1 is used to quantify the effect of the permeability and the thickness of the layer. To achieve this goal, the same simple 2D model is used as in the previous section but with the addition of a barrier heterogeneity. In particular, a comparison is made between a horizontal layer and an angled layer of 5° for different thicknesses of the layer. In the previous section, experiments with a similar packing configuration were performed. Here the simulations aim to expand the Impedance range that can be investigated while examining the effects of layer thickness. As such the background permeability used is the same as in the experiments and equivalent to a bead pack with an average particle diameter of 0.5 mm.

A layer is implemented into the model with a thickness of a) 0.005 m, b) 0.01 m or c) 0.015 m as presented in Figure 7.6. It should be noted that like with the experiments

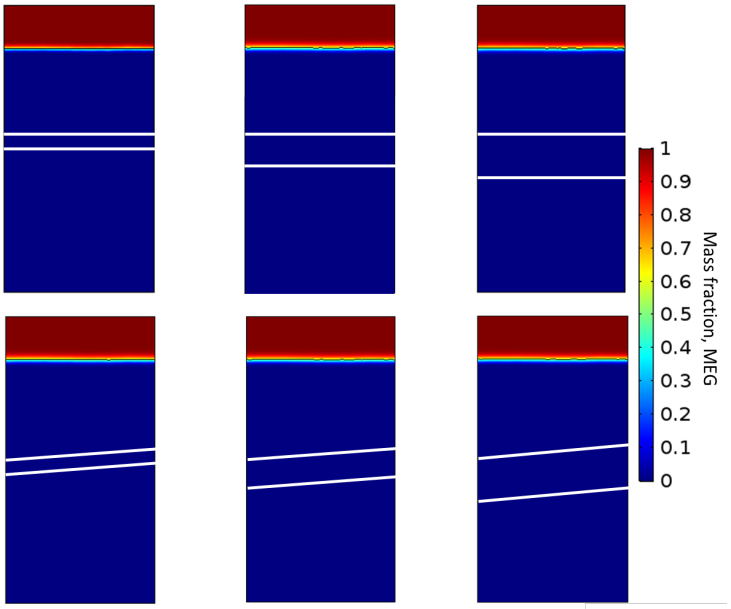

Figure 7.6: Images from the initial time where the fluid are segregated for the three thicknesses of the system with a horizontal(top) and angled(bottom) layer. The layer is highlighted in white.

the distance between the initial MEG-water interface and the barrier is kept constant meaning the area under the layer reduces as the layer thickness increases. Also in each case the Impedance and the thickness are specified, so the permeability of the layer is the variable. Table 7.3 outlines the Impedance of the system along with the corresponding thickness of the layer and permeabilities.

Table 7.3: Details of the permeability of the layer for each permutation of Impedance and thickness. All but 5 of the cases have lower permeabilities compared to the bulk (1.90×10^{-10} m^2), and those with a higher permeability are highlighted in bold.

	Permeability [m^2]	Layer Thickness [m] 0.005	0.01	0.015
Impedance	0.01	$\mathbf{1.11}\times10^{-9}$	$\mathbf{2.22}\times10^{-9}$	$\mathbf{3.34}\times10^{-9}$
	0.1	1.11×10^{-10}	$\mathbf{2.22}\times10^{-10}$	$\mathbf{3.34}\times10^{-10}$
	0.3	3.71×10^{-11}	7.41×10^{-11}	1.11×10^{-10}
	0.5	2.22×10^{-11}	4.45×10^{-11}	6.67×10^{-11}
	1	1.11×10^{-11}	2.22×10^{-11}	3.34×10^{-11}
	2	5.56×10^{-12}	1.11×10^{-11}	1.67×10^{-11}
	5	2.22×10^{-12}	4.45×10^{-12}	6.67×10^{-12}
	10	1.11×10^{-12}	2.22×10^{-12}	3.34×10^{-12}

7.4.1 Results: Visualising Flow

By looking at the mass fraction plots over time and for various values of Ω it is possible to understand the impact on the flow patterns and ultimately understand more fully the trends observed in the dissolution rate and the dilution index.

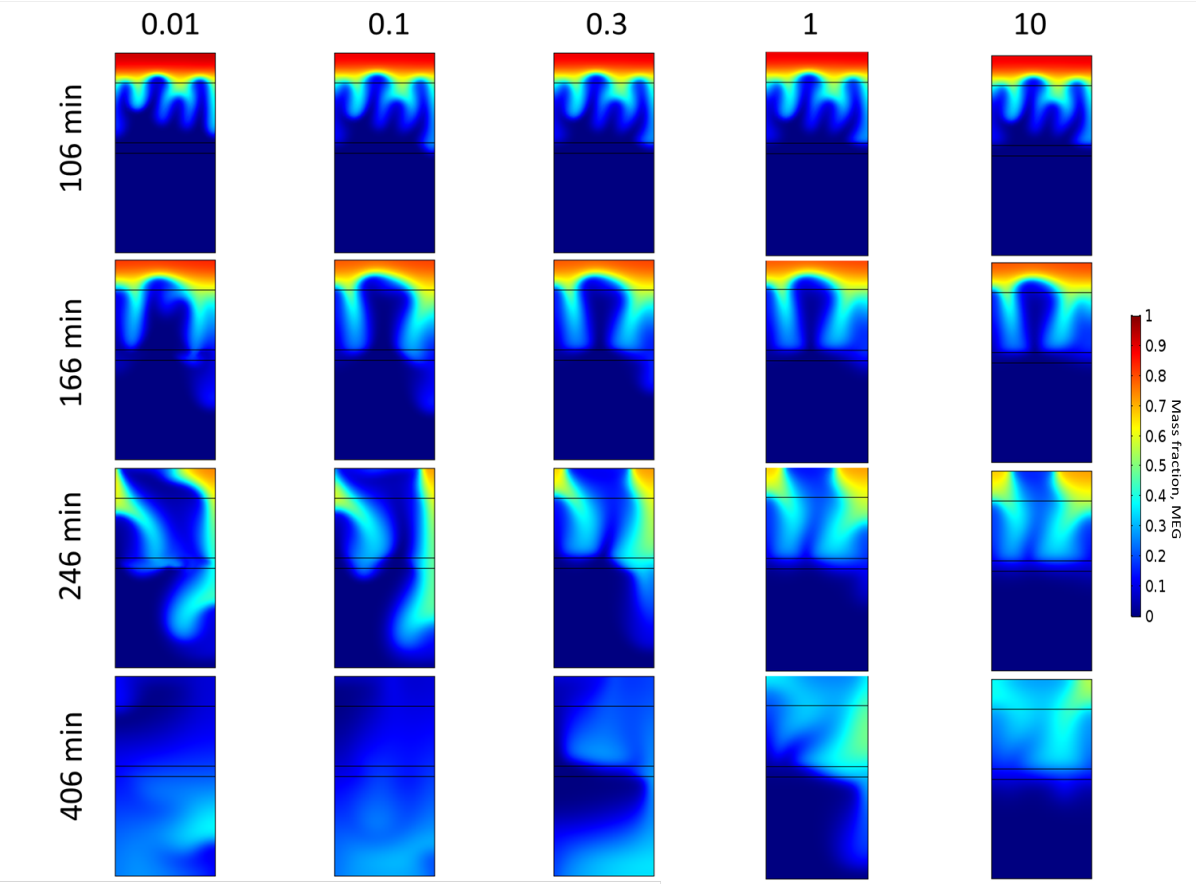

Figure 7.7: Discreet time images in terms of mass fraction for the simulations with a horizontal layer of thickness 0.005 m over the Impedance range 0.01 - 10.

Figure 7.7 shows discreet time representations of the fingering process for the system with a 0.005 m thick horizontal while results for an angled layer are shown in and Figure 7.8, both over the Impedance range Ω = 0.01 - 10. The differences in the plume evolution between the horizontal and the angled case are striking. For all values of Ω a single dominant plume develops for the angled layer case as opposed to two prong-like projections in the horizontal layer. Subtle differences in the initial growth of the fingers are evident at t = 106 min. Although the number of fingers and the placement of the fingers appear similar, the angle of the fingers is different; for the horizontal case they tend towards the left, and with an angled layer they tend towards the right which is the apex of the slope. It is also observed that directly above the apex more MEG has been dissolved in the angled

case than at the same point when there is a horizontal layer. The conformation of the finger structure at early times indicates that the onset of the instability and convection is independent of the Impedance.

However, there also many flow patterns which result from varying Impedance. At $\Omega = 0.01$ the permeability of the layer is higher than the bulk permeability for all three thicknesses. The effect of which is most readily observed in Figure 7.8 at 166 min; the plume contacts the layer and becomes thinner as it quickly passes through. Then at the edge of the more permeable bulk, the opposite is observed where the plume pools and spreads at the interface and becomes dispersed as it seeps into the more resistive bottom domain. Then

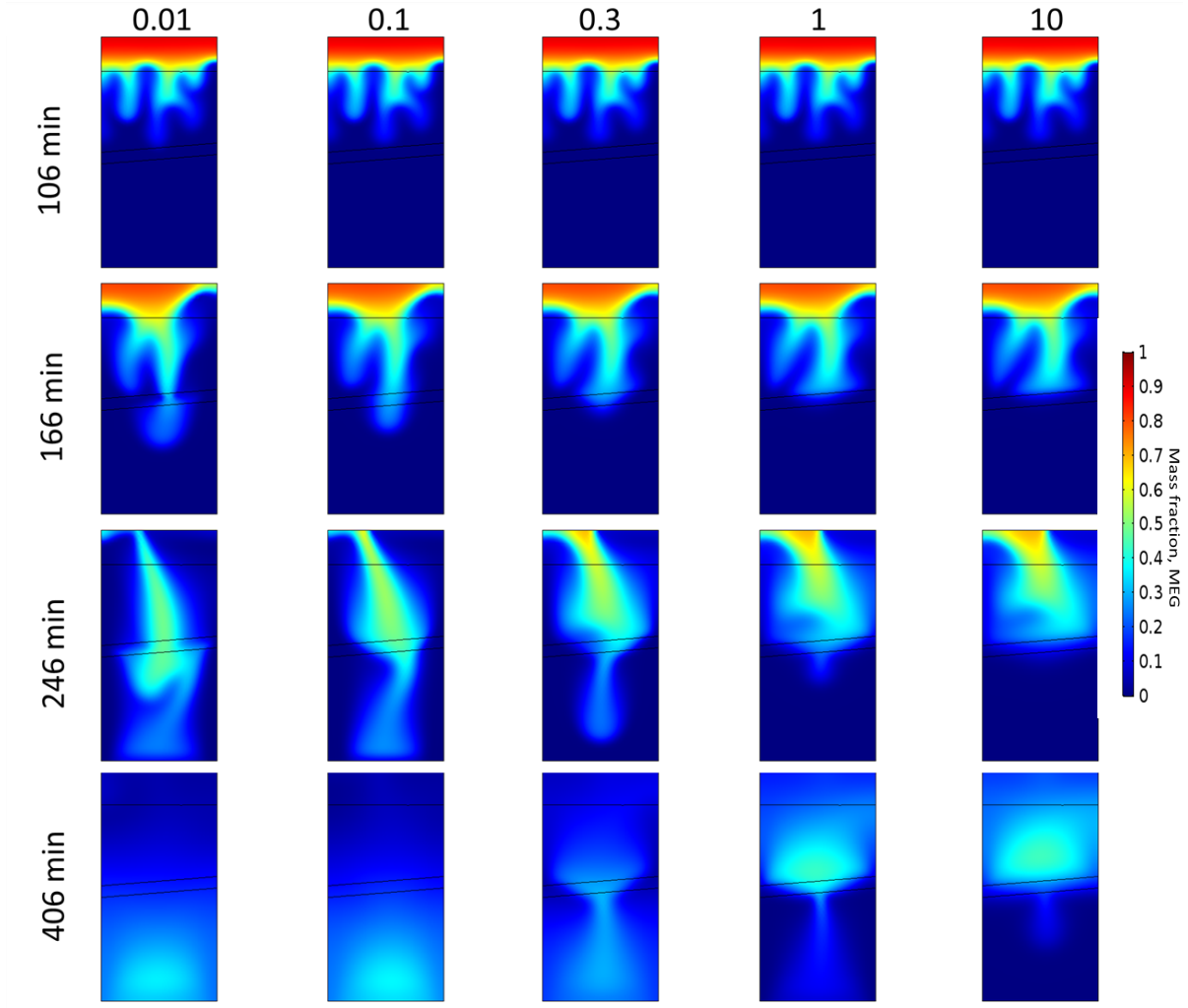

Figure 7.8: Discreet time images in terms of mass fraction for the simulations with an angled layer of thickness 0.005 m over the Impedance range 0.01 - 10.

as Impedance increases (Ω = 0.3-1) the resistance to flow is increased, and it is more difficult for the fingers to propagate through the entire domain until $\Omega > 1$ where the

layer is very resistive and the solute has only started to break through at 406 min. It should be noted that for each thickness an angle the finger structure is not a function of Impedance. Thus, whether one or two dominate fingers prevail the same pattern is seen across the Impedance range. In Figure 7.7 for example, one dominate plume is increasingly constrained as Impedance is increased indicating that the initial perturbation and conditions dictate the development of the plume at the interface. A generalised analysis has been discussed based on the images of the systems with a 0.005 m thick layer; however, these ideas can be translated to all data sets.

7.4.2 Results: Dissolution Rate and Dilution Index

It is possible to relate the behaviours seen in Figure 7.7 and Figure 7.8 to the dissolution rate and dilution index curves. 54 simulations were run, and the dissolution rate and the dilution index were calculated in line with the method outlined in Section 7.3. The curves are compiled and segregated based on the thickness of the layer for the horizontal case in Figure 7.9 and the angled case in Figure 7.10 where the dissolution rate is presented in the left column and the dilution index on the right. The curves are colour coded based on Impedance from blue ($\Omega = 0.01$) to red ($\Omega = 10$) with the addition of the homogeneous curve (black dashed) for comparison.

Between the system with a horizontal layer and an angled layer there are some similarities in the general shapes of both the dissolution rate curves and the dilution index curves; for the most part, the dissolution rate goes through a maximum which is systemically lower and later as the Impedance is increased. Likewise for the dilution index the shape of the curve generally follows a sigmoid pattern with the plateau of the curve being reached later and for a lower final value of E/E_{max} as Impedance increased. In each of these plots, the homogeneous case is also plotted with a black dashed line. It should be noted that due to a numerical error the simulation did not accurately capture the characteristics of the angled case for Impedance = 0.01; however, the curves are shown for completeness.

It is observed in Figure 7.9 that there is a peak in the dissolution rate at low Impedance (0.01-0.5) which becomes less pronounced as Impedance is increased. It can be also observed from the reconstructions that the flow is halted at the layer resulting in a lower maximum rate of dissolution and prolonging the time taken for the maximum to be

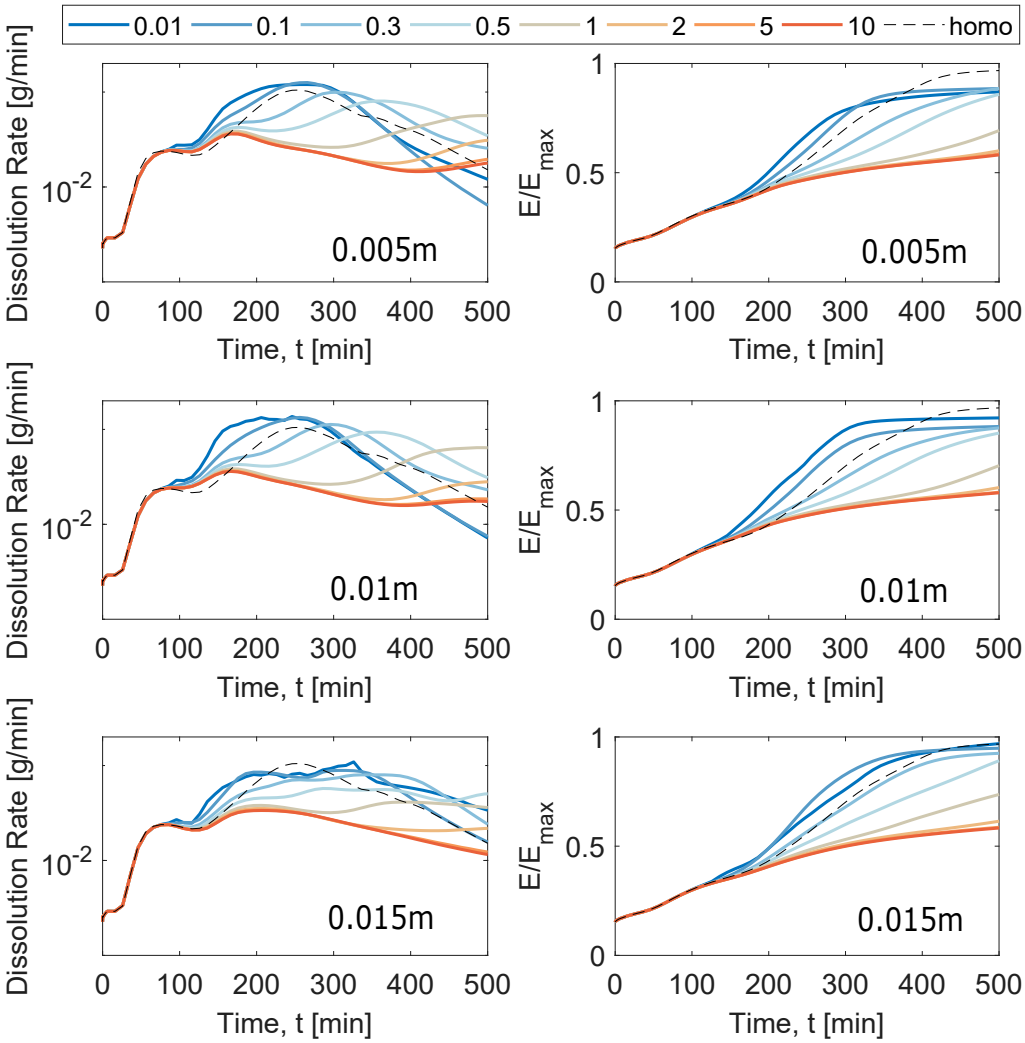

Figure 7.9: Complete set of results for the dissolution rate(left column) and normalised dilution index(right column) for simulated with a single horizontal layer of differing permeability corresponding to an Impedance on the system of 0.01(blue)-10(red). The results are grouped in terms of the thickness of the layer 0.005 m(top row) 0.01 m(middle row) and 0.015 m(bottom row). The homogeneous case is also presented for comparison(black dashed) in each graph.

reached. Similarly, the dilution index is substantially lower in the $\Omega > 1$ cases because solute has saturated only half the domain by 406 min. The only exception to this is in the 0.005 m angled case where it is observed that the dilution index for the low Impedance values results in a less well-mixed system than at higher values, this is a result of a fast-moving plume and the accumulation of heavy material at the bottom of the domain as observed in Figure 7.8.

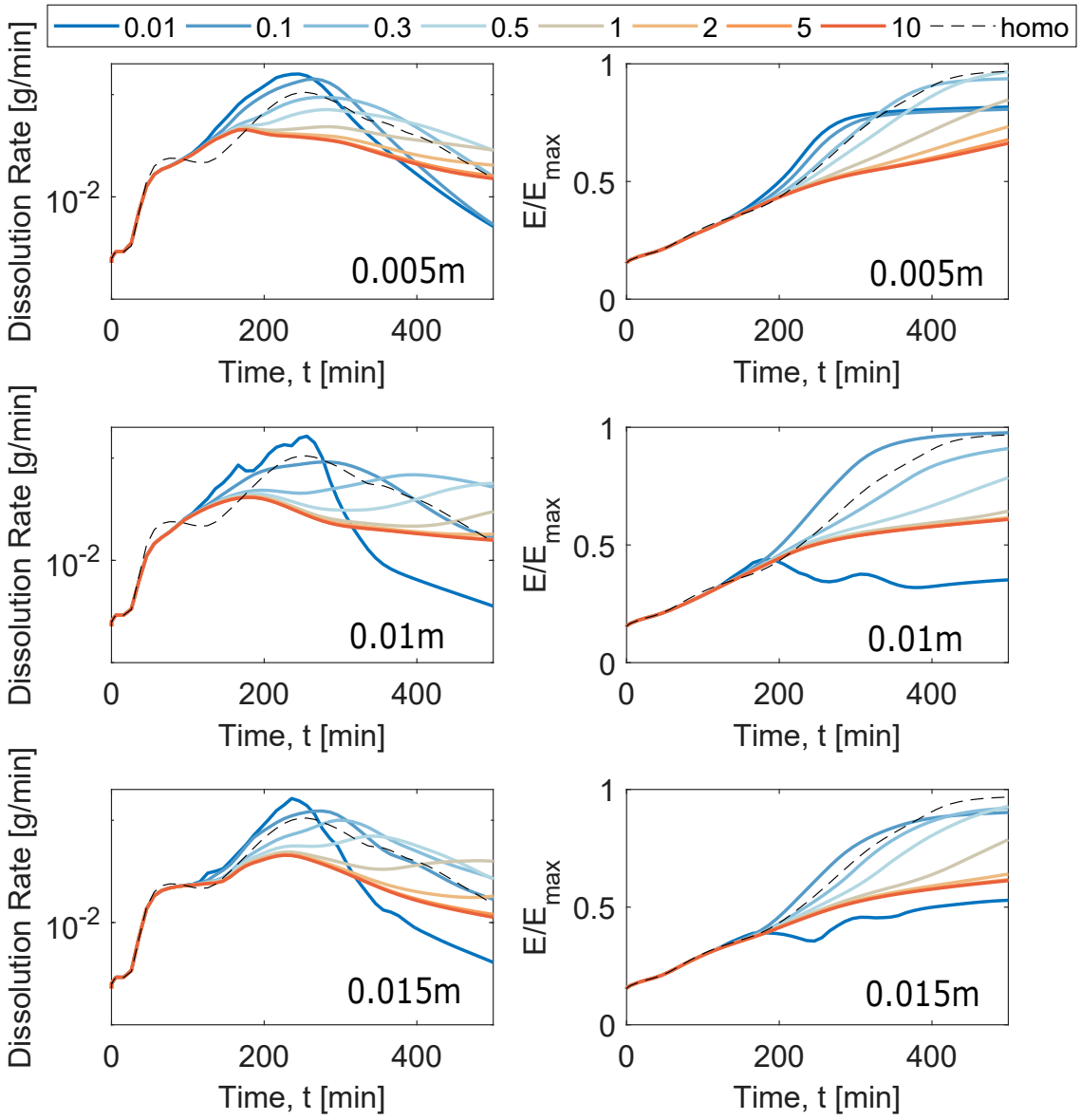

Figure 7.10: Complete set of results for the dissolution rate(left column) and normalised dilution index(right column) for simulated with a single angled layer of differing permeability corresponding to an Impedance on the system of 0.01(blue)-10(red). The results are grouped in terms of the thickness of the layer 0.005 m(top row) 0.01 m(middle row) and 0.015 m(bottom row). The homogeneous case is also presented for comparison(black dashed) in each graph.

Overall, therefore, it can be said that the trends for both the dissolution rate and dilution index for both cases are comparable to the homogeneous case and in general the purely homogeneous permeability field does not represent an upper bound for the process when lower permeability layers are introduced. These curves provide some insight into the general dynamic behaviours but given the number of data sets another metric is required to compare these cases. In the next section, this idea will be explored further by calculating and comparing the Sherwood number for each case.

7.4.3 Results: Sherwood vs Impedance

As in the previous Chapters, it is possible to quantify the effects of the increase in the rate by convection by calculating the Sherwood number. As before the maximum rate is compared to the diffusive rate at the same time step. *Sh* is plotted as a function of the Impedance in Figure 7.11left for the horizontal layer and right the angled layer and grouped by thickness 0.005 m (orange), 0.01 m (grey), 0.015 m (yellow) and the straight blue line indicates the homogeneous situation.

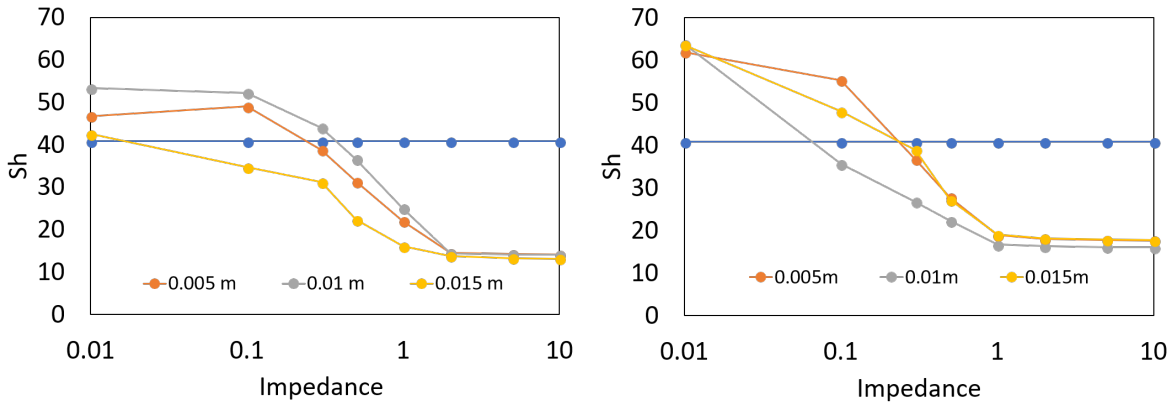

Figure 7.11: Sherwood as a function of Impedance for a system with a horizontal layer (left) and angled layer (right) where this thickness of the layer is 0.005 m(orange), 0.01 m (grey) and yellow (0.015 m) and the homogeneous case (blue) plotted for comparison.

In Figure 7.11 for all cases *Sh* is initially larger than the homogeneous case because the layer is more permeable than the bulk for $\Omega = 0.01$. By the reasoning that with an increase in the total vertical permeability there is an increase in the rate, it is not surprising that *Sh* is higher than the homogeneous case. Thereafter however the trends are not so straightforward.

There are several differences in the particular characteristics of the *Sh*-Ω curves for the angled and horizontal cases. For the latter, *Sh* is higher than homogeneous case initially at $\Omega = 0.01$ and remains relatively constant for the orange and grey curves for $\Omega = 0.1$. At which point *Sh* decreases proportionally with Impedance until $Sh = 15$ at $\Omega = 3$. In contrast, for the angled case there is no constant region at low Ω. Instead, *Sh* immediately decreases proportionally to the Impedance and the final constant region beings at $\Omega = 1$ which is a lower Impedance than in the horizontal case.

One interesting outcome of this study is that *Sh* is consistently higher for the angled layers compared to the horizontal layer. On average the Sherwood number is 1.1 times

larger for the angled layers for all thicknesses and across the Ω range. Together these two observations imply that although *Sh* is generally higher in the angled system compared to the horizontal, the rate is more easily arrested with a lower Impedance on the system. In the angled case a dense fluid pools at the boundary on the low side and this can force transport through, increasing the rate compared to the horizontal case. However, this may not reflect the behaviour in larger systems where the boundary is less important.

7.4.4 Discussion: Role of Finger Merging and Flow Focusing

By examining these curves and individual simulations more closely, it is possible to pick out particular differences that can be related to mixing patterns and finger structures. It may be expected that the systems with the thinner layers would have a higher *Sh* compared to those with a thicker layer. However, in this data set, there no consistent observation of this type. There are different trends in this order for the angled and horizontal cases respectively.

In the simulations with a horizontal layer, those with a 0.01 m thick layer have the lowest *Sh* compared to the 0.005 m and 0.015 m systems which are present with systematically lower curves but whose courses track independently of each other. The systems with an angled layer present with the opposite trend; the cases with a 0.01 m thick layer have the lowest *Sh*, and the 0.005 m and 0.015 m curves are almost identical. There is also a significant difference in *Sh* for the 0.015 m system depending on whether the layer is angled or horizontal.

To understand these trends we turn to the mass fraction-velocity plots, and in Figure 7.12 is a comparison of the finger structure for each system, angled (top) and which also include velocity arrows indicating the direction of flow by the arrowhead and the relative magnitude by the size of the arrow. All these images were taken at the time of or the closest to the time of the maximum rate of dissolution ($\approx$ 250 min) where $\Omega = 0.1$.

In Figure 7.12 it is clear that there is a range of finger structures and there is not a specific pattern related to either the angle of the layer or the thickness of the layer. In the angled system(top row) two distinct flow patterns emerge; a single dominant plume (0.005 m and 0.015 m) and a two-pronged plume(0.01 m). From the velocity arrows in the thickest angled system, it is clear that the flow is focused and is moving more rapidly in the plume.

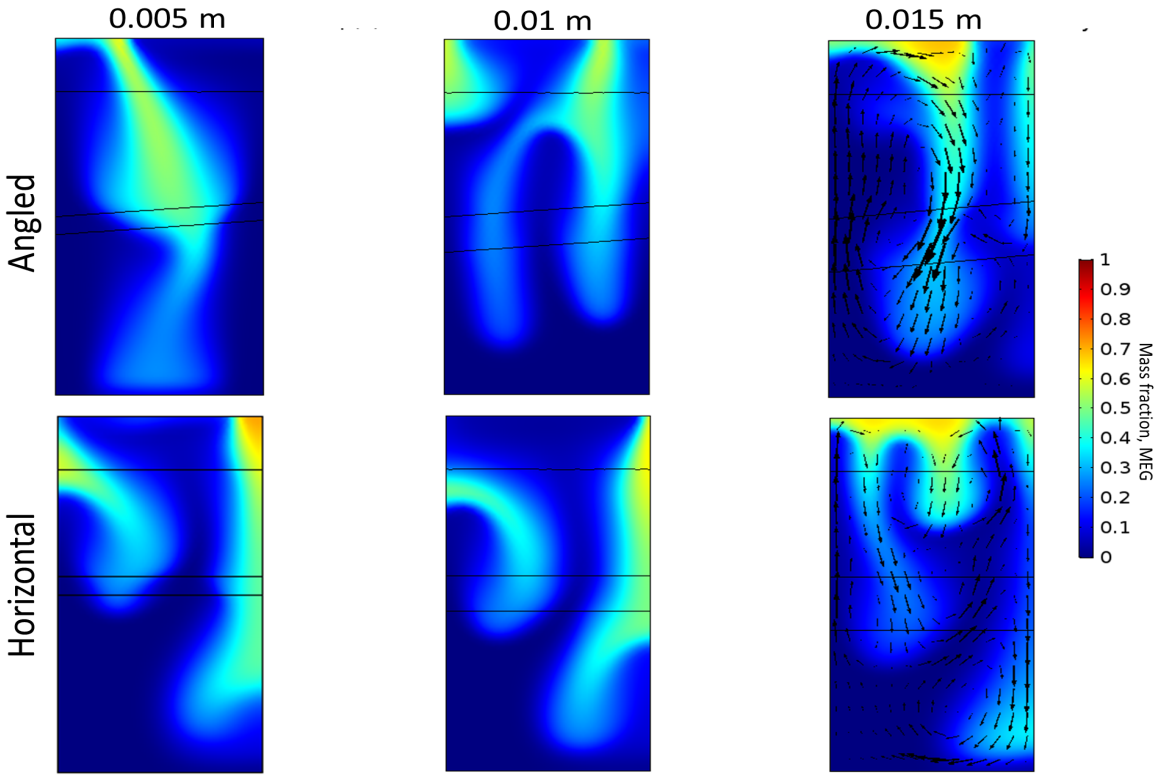

Figure 7.12: Single time (≈ 250 min) mass fraction image from each of the simulations where the Impedance on the system is 0.1. Where a layer of differing permeability is either angled(top row) or horizontal(bottom row) for each of the three layer thickness investigated 0.005 m(left), 0.01 m(middle) or 0.015 m(right) which has the addition of velocity arrow indicating the direction of the flow and the relative magnitude.

This structure causes a fast convection cell to emerge which has grown in this image to almost the height of the domain. A single plume is a good example of 'flow focusing' which has been suggested to increase the rate in systems with layered heterogeneity [74].

In the corresponding horizontal system, the flow dynamics are entirely different. No single finger has reached dominance and the velocity arrow indicate the flow is moving more slowly in these plumes compared to the dominate plume observed in the angled case. In addition to this, a secondary vortex has formed at the lower right corner with a central stagnant zone due to an early sunk package of solute. These flow behaviours can explain why *Sh* for the angled case for the 0.015 m layer is consistently larger than the horizontal equivalent; there is an optimal distribution of flow that leads to a higher rate.

The same but opposite reasoning can be applied to the systems with a 0.01 m thick layer. Here, the lighter water is focused into one fast up-welling which is pushing the solute down. As opposed to the angled case where a double prong structure is observed which divert the flow in two directions resulting in a slower moving plume and thus a lower

Sh. It was already shown in Figure 7.7 that the same fingering behaviour is prevailing across the Impedance range so flow focusing can explain the trends observed across the Impedance range.

But, a unique feature of the $\Omega = 0.1$ data set is that only the thinnest layer has a permeability lower than that of the bulk (see Table 7.3). The permeability contrast explains why in the horizontal system the 0.01 m case *Sh* is consistently higher than the 0.005 m despite the strong similarities in the plume patterns as overall the vertical permeability is lower for the thinner layer compared to the thicker layer.

Interestingly this arguments does not hold in the angled case as the 0.005 m case, which we know has a lower vertical permeability, presents with a largest *Sh*. There is also clear indication that the flow has a higher magnitude in the thick high perm zone of the 0.015 m case suggesting that flow is faster. However, the dissolution rate is determined by the accumulation of mass in the bottom domain so it is suggested that pooling is responsible for the higher rate of dissolution. It can be observed that more of the region above the layer is filled with solute in the case where there is a thin less permeable layer compared to the thick more permeable layer. In the latter, less MEG is depleted from the initial layer, less MEG is dissolved, and thus the rate is lower for the thicker layer.

In the previous Chapter, there was an unexpected result where *Sh* was increasing with Impedance particularly when the the layer thickness was increased. It was not clear from the reconstructions alone why mixing appeared to be progressing faster when the system should have been Impeding flow more. By considering the results of the 2D simulations we suggested that pooling is responsible for this observation. Looking again at the reconstructions in Chapter 5 there is an accumulation of the MEG above the layer. Lateral spreading of the plume at the layer interface may also be a contributing factor. This is largely speculation but what is certain is that these results indicate that there is more than one mechanism dictating the behaviours of convective mixing in layered systems.

7.4.5 Summary

The analysis of a single layer of lower or higher permeability in an otherwise homogeneous permeability field has yielded exciting and surprising results. The seemingly simple

addition of a layer has profound effects on the flow with mechanisms such as flow focusing and pooling or by disrupting the formation of optimal patterns of mixing. The literature indicates that the rate of dissolution will increase irrespective of how the vertical permeability is increased but this does not reflect the findings from this study. These results suggest that although, in general vertical permeability is important in predicting the rate of dissolution, how and were the plume organises itself is also a determining factor.

7.5 Multiple Layer Heterogeneity

Finally, in this Chapter the effect of a multiple discontinuous layering on convective dissolution is evaluated with a generic layered system where the permeability of the bulk compared to the layer is set to a ratio of 4, 8, 12, 16, 25 and 30. Shown in Figure 7.13 is a sketch of the geometry highlighting the patches with a white boarder.

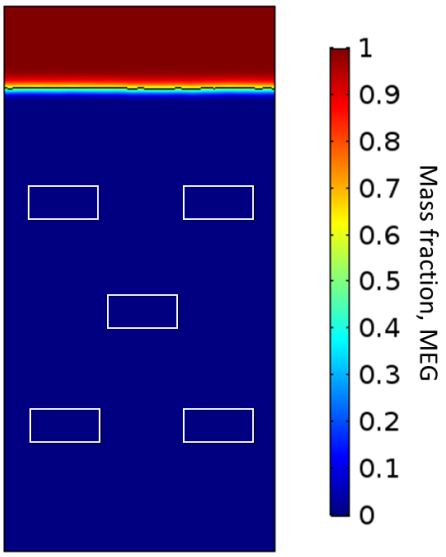

Figure 7.13: Images from the initial time where the fluid are segregated for the three thicknesses of the system with a horizontal(top) and angled(bottom) layer. The layers are highlighted in white.

7.5.1 Results

Again the dissolution rate is calculated for each of the cases and is shown in Figure 7.14 left as a function of time using the blue to red colour scale for increasing k_1/k_2 and the homogeneous case plotted(black dashed) for reference. Figure 7.14 right is plotted the

normalised dilution index as a function of time using the same colour coding.

The first observation is that these results are much more homologous than those for the single layer. The curves are identical until 206 minutes for the dissolution rate and 256 minutes for the dilution index. At this point, they diverge according to the permeability ratio. In general, as compared to the homogeneous case the curves track a similar pattern but at a lower rate or index.

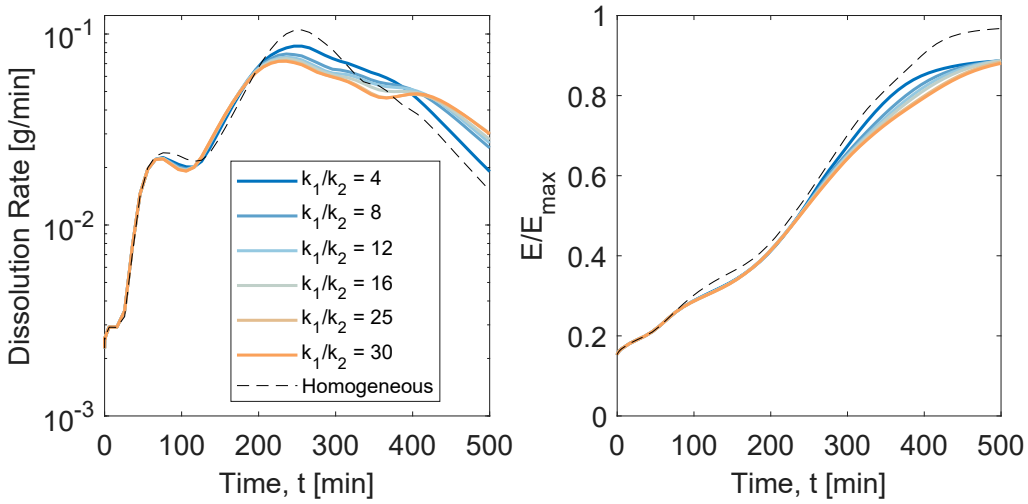

Figure 7.14: Left: Dissolution rate as a function of time for each scenario where the ratio between the permeability of the bulk, k_1 and the layer, k_2, equal to 4, 8, 12, 16, 25 and 30 coloured blue to red. Right: Normalised dilution index as a function of time for the same 6 cases denoted with the same colour coding as rate plot. The homogeneous case (black dashed line) is also plotted for comparison in each graph.

By looking at the mass fraction plots with velocity arrows, it is clear why we see this trend in the dissolution rate and dilution index. Figure 7.15 shows images of the most and least resistive layers at six times. In this figure, it can be observed that the flow structures are almost identical for the two cases. The differences lie in the local velocity of the fluid inside the low permeability patches. A prime example of this is at 226 min where the flow is moving downwards in one dominant plume but is diverted in both cases by the presence of a barrier, and the plume is forced to meander around the patch. Only where $k_1/k_2 = 4$ can tiny velocity arrows can be observed. With ratios of permeability higher than 4 the flow is so slow relative to the plume, there are no arrows visible. It can be surmised from these results that with a mostly connected pathway of higher permeability, the flow forms preferential channels which are independent of the permeability of the intervening barriers. This study replicates previously published results of flow around less permeable

patches where the patches represent non-mobile zones [69, 54].

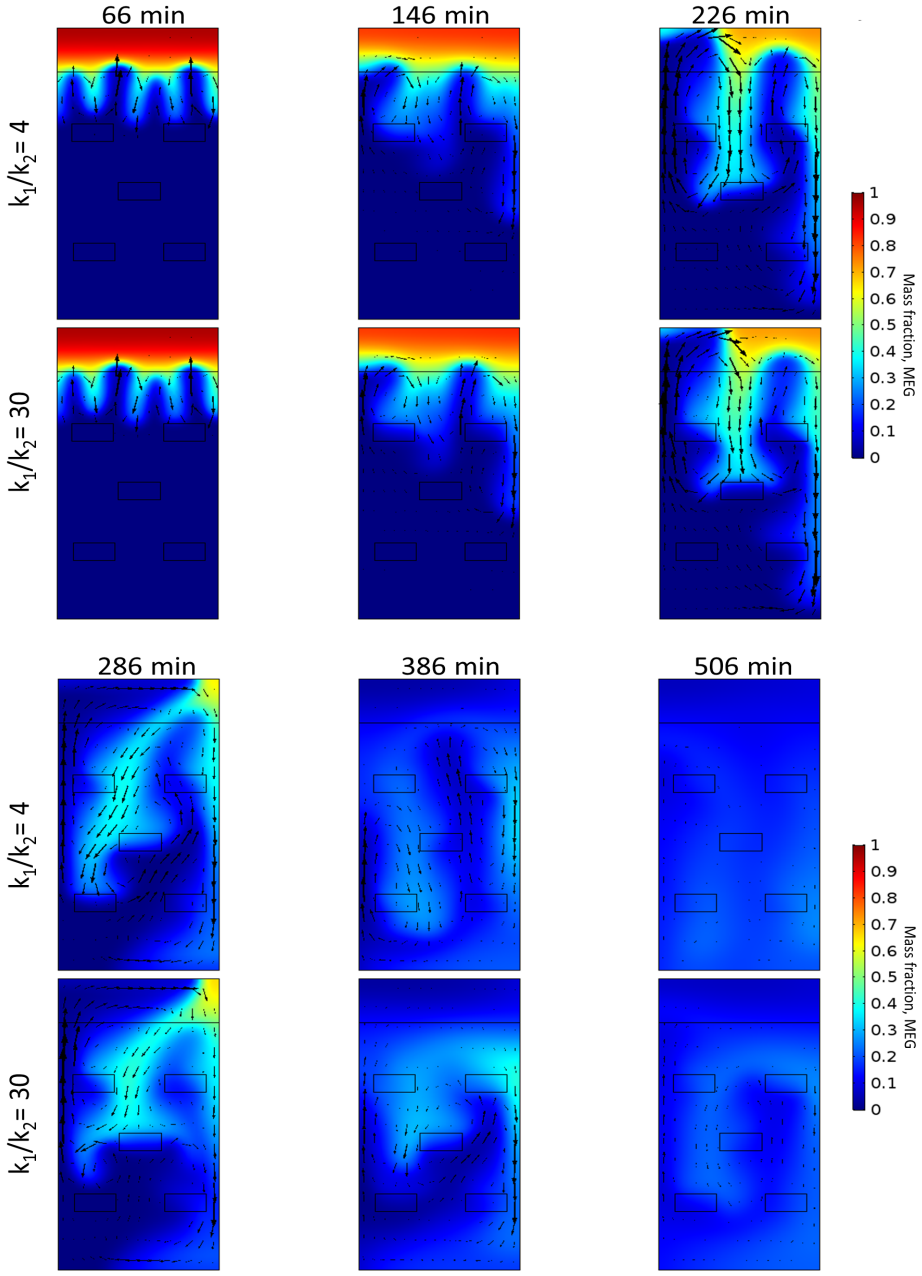

Figure 7.15: Comparison of the multi-layered systems where the ratio of the permeabilities between the bulk and the layer is 4 (top row) and 30 (bottom row) shown over 6 times in terms of mass fraction with velocity arrows.

7.6 Summary

In this Chapter, a simple 2D COMSOL simulation has been used to investigate the effect of permeability heterogeneity on the flow and mixing of MEG into water via the process of convective dissolution. The first section of the chapter focused on a homogeneous

case as to establish a baseline to build on for the following inclusion of permeability heterogeneity. In that study, the *Ra* number was varied by changing the permeability of the domain. To make comparisons to the experiments, we used the Kozeny-Carmen equation for calculating the permeability equivalent to a bead pack with particles of 0.2-2 mm in diameter.

Using mass fraction images from different times in the simulation it was possible to observe directly the flow pattern and mixing behaviours. It was observed that the larger the permeability, the larger the wavelength of fingers at formation, leading to a fast progression of convection and thus a faster shut down. Therefore, when the dissolution rate is plotted it was found that the rate is higher with a higher *Ra*; however, it did not automatically mean that the mixing was more efficient. By calculating the dilution index, it was evident that the when convection was very fast it ended is a less well-mixed system than when it was going more slowly, due to a heavy unmixed plume which sat at the bottom of the domain. Looking at the *Sh*-*Ra* relationship, a linear trend was observed that matched very well with the experiments.

Then a single layer of heterogeneity was introduced. The layer was either horizontal or had an angle of 5° with a thickness set at either 0.005 m, 0.01 m or 0.015 m. A relationship with Impedance, Ω (comparison of the hight of the layer and its permeability compared to the domain size) determined the permeability of the layer. Ω = 0.01 - 10 was investigated. For each of the 54 cases simulated, *Sh* was calculated and plotted. The trends for the horizontal vs the angled case differed in a variety of ways, namely that overall the Sherwood of the system with and angled layer, Sh_A was larger than the corresponding horizontal system, Sh_H, so that $Sh_A = 1.1Sh_H$. It is so far unclear exactly what is causing this increase however it is suggested that the angled promotes pooling of material at the low side increasing mass transport through the layer. Other differences in *Sh*-Ω trend are observed according to the differing thicknesses of the layer and these suggested, primarily, to be caused by flow focusing. And finally, it was evident that the compartmentalisation of the flow by continuous layers which impede flow has profound impacts as compared to a discontinuous layered case where the plume speed and overall rate of dissolution are mostly unaffected by the patches.

Chapter 8

Conclusions and Future Work

8.1 Conclusions

In this thesis, we have systematically investigated convective dissolution in a porous medium in the Rayleigh range of $\mathcal{O}(Ra) \sim 1000$ using X-ray CT imaging and numerical simulations.

In Chapter 3 we first presented some of the first observations of the mixing patterns of three-dimensional convective dissolution in an optically opaque, uniform porous medium with MEG-water as a model fluid pair. The experimental protocol as laid out in Chapter 2 enabled non-invasive imaging of the dynamic behaviour of density-driven convection at sufficient spatial($2 \times 2 \times 2$) mm^3 and temporal (70 s) resolution so that solute concentrations could be quantified and parameters such as the onset time, shutdown time and dissolution rate could be extracted.

It was observed that the onset time scaled with Ra^{-2} similar to scaling reported in the literature [11, 34]. It was found that the growth and evolution of the fingers could be described as a pseudo-diffusive regime expressed by an effective diffusion coefficient where the magnitude was two orders higher than pure diffusion.

As an extension of this work, the viscosity ratio was investigated by changing the fluid pair from MEG/water to BEG/water. The BEG has as viscosity 16 times larger than brine whereas the MEG is only 3 times larger. It was concluded that with a supposedly constant Ra (determined from the maximal density difference and the brine viscosity) the increase in the viscosity ratio between the top and bottom fluids delayed convection both in its

onset time and the shutdown time. However, the increased viscosity did not dramatically affect the overall enhancement of dissolution by convection. It was shown that the scaling relationship between the Sherwood and Rayleigh number was found $Sh = 0.021Ra$ for the MEG and BEG experiments together and $Sh = 0.025Ra$ for the MEG experiments alone. So, although the process was delayed, the Ra calculated based on the brine viscosity was still a suitable predictor for the maximum rate of dissolution.

In Chapter 4 the experimental geometry was varied to evaluate the effect of a changing or constant cross section. Three vessels were chosen, the bowl(used in Chapter 3), a cylinder and a cube where the same fluid pair and permeability were used for all three cases. The onset time of all three geometries was $\approx$ 20min but the shutdown time for the cube and cylinder was 100 min slower than in the bowl; this difference in shutdown time resulted in an effective diffusion coefficient half that observed in the bowl. The strong similarity in the macroscopic behaviours of the bowl, cylinder and the cube at early times indicates that it is the changing cross-section of the bowl that is enhancing convection after the onset which results in a larger $\mathscr{D}_{\text{eff}}/\mathscr{D}$ and reduced shutdown time.

In Chapter 4 an analysis was also undertaken to better understand the impact of the geometry on the pattern formation and evolution. By looking at a single horizontal cross-section, 2.5cm below the initial interface, the number of fingers was counted, and the average size of the fingers was reported. In both the cube and the bowl we initially observed many small fingers which merged and formed fewer larger fingers with time. The spatial correlation of the fingers was calculated from a spherical variogram model, and it was observed that the correlation length increases linearly with time and the maximum length was higher in the cube compared to the bowl.

In Chapter 5 and 6 the effect of increasingly complex permeability heterogeneity on convective mixing were investigated. In Chapter 5 a single continuous layer of lower permeability was introduced into the packing with a 5° incline and the thickness and permeability of that layer was varied. The overall Impedance, Ω on the system was determined as a function both the permeability ratio between the bulk and the layer and the ratio of layer thickness to total domain height. A range of Impedance was investigated spanning $\Omega = 0.1 - 8$.

Similar to the homogeneous case, the change of mass and horizontally averaged concentration profiles were plotted, and from these, it was observed that for $\Omega > 1$ com-

partmentalisation of the flow due to the barrier was observed. In the change of mass curves, a late time tailing was attributed to the build-up of mass above the layer and the subsequent slow migration of the fluid through the less permeable zone. Pooling behaviour was observed in the reconstructions and in the 1D concentration profiles where lingering bumps correlated to the location above the layer. For $\Omega < 1$ pooling was not as significant as the permeability of the layer was not sufficiently low to impede the flow of the fingers completely. In this case, instead, we observe the phenomenon of flow focusing and conclude that this results in a slight increase(5%) in the overall rate of dissolution compared to the homogeneous case.

In Chapter 6 we investigate more heterogeneity patterns with a series of increasingly complex discontinuous layers. The same X-ray CT imaging protocol was followed using the MEGKI-brine fluid pair. In this Chapter three types of heterogeneity were investigated; 2 disconnected angled layers, chequerboard-style patches of lower permeability and a random heterogeneous packing. The 3D finger structures were observed to be unique for each configuration with behaviours such as pooling, merging and secondary finger development being commonly observed. In addition, the macroscopic measures of mixing were presented; the onset time was found to be consistent with the onset times of the homogeneous case which indicate (as with the different geometries, and in fact the single-layered case) that the onset time is independent of the nature of the domain below the interface.

The rate of dissolution in a layered system was found to be highly dependent on the spatial distribution of the layer and the most importantly the distance between the layers. In the four experiments presented in Chapter 6 the volume percentage of packing occupied by the lower permeability layers was $\sim 20\%$. However, in the two case where the impermeability of the layering was equivalent the case with large spacing between the layers ('Patchy' case) resulted in a faster rate of dissolution and quicker shutdown time compared to the case with narrow spacing (2layer $k/k_L = 25$).

Furthermore, a $Sh - Ra$ plot was compiled and presented in Chapter 6 which brought together all of the experimental data from Chapter 3, 5 & 6. Interestingly, the scaling was found to be surprisingly similar to the original scaling presented in Chapter 3 ($Sh = 0.025Ra$), as it is found to be $Sh = 0.0236Ra$. In this thesis, the linearity of the $Ra < 5000$ regime with Sh has been observed in a homogeneous packing and with various

simple permeability heterogeneities, for four different fluid pairs.

In Chapter 7 the 2D COMSOL simulations provide insights into a greater range of Ra (200-10,000) than what was possible experimentally, however, unlike in the experimental case we varied the permeability instead of the fluid pair to investigate Ra. Here, we used the Kozeny-Carmen equation for calculating the permeability equivalent to a bead pack with a particle diameter of 0.2-2 mm. In general, the dissolution rate increased with Ra; the fingering process occurred faster with larger plumes and shorter shutdown times. However, it was observed that for $Ra > 5000$ the fast-moving plumes could result in a less well-mixed system than slow-moving plumes at lower Ra. Nevertheless, there was a linear relationship between the Sherwood and Rayleigh number which matched with the results of the 3D experiments.

We introduced a single angled layer into the 2D model to supplemented and extend our understanding of the effect of layered heterogeneity from the experiments. The Impedance, Ω, was varied between 0.01 and 10 for different thickness of a horizontal and angled (5°) layer, and in each case, the Sh was plotted as a function of Impedance. Flow focusing, or lack thereof, was the most important factor in determining the relatively higher or lower rate of dissolution observed for different layer thicknesses. It was also observed that between the angled and horizontal system the presence of an incline in the layer caused an increase in the rate of dissolution compared to the horizontal case so that $Sh_A = 1.1Sh_H$. But, it was also shown that the angled system was more sensitive to increasing Ω and likely to reach a minimum Sh at lower Ω.

Finally, in Chapter 7, we confirm the findings of Chapter 6 and concluded that in a situation with many evenly spaced barriers the rate of dissolution was unaffected by the strength of the permeability ratio between the bulk and the layer but instead by the spatial distribution of the layers.

The general conclusion of the thesis is that the process of convective dissolution is sensitive to changes in the initial conditions, the boundary conditions and to permeability heterogeneity. The onset times is, as expected, largely decoupled from these effects and only dependant on the immediate fluid properties and permeability. However, the subsequent rate and shut down of convection have a strong dependence on spatial parameters. Despite these factors, the $Ra - Sh$ scaling have been shown to be consistent.

8.2 Future Work

The application of carbon storage has been the most important motivator in this project. However, as yet, there is no direct observation convective dissolution at reservoir conditions in a sandstone or carbonate sample. The findings presented in the thesis provide positive indications that convective dissolution does occur at industrial relevant *Ra* and in the presence of permeability heterogeneity, however, all of the work presented in this thesis has used model fluids in bead packs. So it is clear the direction this project should take is to use the real rock-fluid system at reservoir conditions.

8.2.1 Convective Dissolution in a Rock Sample

It is important to verify if convective dissolution will take place in a real rock system with the presence of heterogeneity and chemical interaction. To achieve this goal, the experimental complexity should be increase stepwise. At first, the same experiments conducted in the bead pack should be done in a rock, i.e. with the analogue fluids MEGKI and brine and with the same imaging protocol. The foreseeable challenges would be in establishing the initial flat interface. It is suggested to modify the current methodology where a slurry of MEG and beads is poured on to brine-saturated packing of beads and used instead a brine - saturated rock core. After which a method could be developed whereby the MEG is injected into a core, and a pistol-like displacement is achieved.

Once the procedure of imaging convective dissolution in a rock has been established, it would be interesting to investigate a partially miscible liquid-liquid system such as an alkyl formate in water [96]. It has been suggested that use of fully miscible fluid pairs do not accurately describe the nature of the CO_2-brine as there are no surface tension effects. The result, therefore, is that the extrapolation of experimental results from miscible systems to immiscible systems is not straightforward and must be done with caution.

The next step would be to use gaseous CO_2 and brine, first at ambient and then reservoir conditions. An important consideration when designing a new two-phase experiment would, again, be setting up the initial condition. In the field, the initial condition of the CO_2 brine interface will heavily depend on the nature of the formation and the location of the injection site. Previously the interface has been dramatically simplified

especially in the modelling of convective dissolution which has been, by and large, simple 2D representations of a homogeneous, isotropic porous media where a.) the CO_2-brine interface is represented with constant concentration top boundary [18, 19, 20] or b.) a fixed volume of CO_2-brine model with a receding interface [21]. Experimentally, where CO_2-water has been used to investigate convective dissolution experimentally the CO_2 has been introduced as a free phase directly above the water in an empty Hele-Shaw cell [19, 55, 97].

The reality, of course, is a two-phase system interacting in a 3D porous medium. The gaseous CO_2 sits atop an aqueous boundary and between the two exists a capillary transition zone where the effects of capillarity and wettability dictate the distribution of the CO_2 and brine. Additionally, there are swelling effects of the brine as mass is added in the form of CO_2 and so an upward movement of the interface. The true nature of the interface, therefore, has been dramatically simplified for the ease of experimentation and simulation. Numerically, these complexities are being taken into account [22, 23, 24] and we suggest that experiments follow accordingly.

Another possibility is to mimic the conditions in the field and inject CO_2 from the bottom and allow the free phase to displace water and form a buoyant plume at the top of the setup. The difficulty with both these methods would be in using X-ray CT as the imaging protocol. The density difference between the CO_2-brine and brine would be very small and difficult to detect; an alternative would be to use PET, perhaps with a radiolabeled carbon^{11}.

8.2.2 Coupled Flow with Reaction

The final addition to fully represent the conditions in the subsurface is the inclusion of fluid-rock interactions. Many fundamental studies have been undertaken surrounding this topic of reaction with the application of CO_2 sequestration; thus, reliable estimates are available for the rate constants of calcite dissolution [98], for the CO_2-brine densities and viscosities at different temperatures and pressures [99], for the diffusion coefficients of CO_2 in brine [100] and, generally, of the CO_2-brine-mineral phase equilibria [101]. However, no definitive experimental work has been presented where density-driven convection following CO_2 dissolution in brine is coupled with the reactivity of the rock matrix that leads to

changes in its porous structure.

The influence of a change in porosity due to the dissolution of the rock on free convective is met with two opposing arguments; whether the reaction will dampen or promote convection compared to buoyancy-driven flow alone. In the first case, the dissolution of the carbonate matrix consumes the CO_2 which is argued to result in an insufficient density difference for the onset of the instability; thus onset is delayed [102]. These arguments suggest that as reaction rate increases convection will decrease as finger formation will be dampened [103, 104], therefore, assuming a fast reaction consumes buoyancy. It is assumed that once reacted the ions do not participate in convection. However, this seems unlikely unless a precipitation reaction occurs. The density increase from dissolved calcite has been calculated to be the same order of magnitude as that from the dissolved CO_2 [105, 106]. It seems logical this density increase will have a strong effect on convective mixing and not dampen the effects as speculated.

Otherwise, it is supposed that by coupling reactions and mixing, In areas of higher porosity preferential flow paths of higher velocity form result in a further enhancement of convection [72]. The argument for an enhancement of convection is as a result of a mixing-inducing reaction. It is assumed that before the onset of convection the CO_2 saturated brine will be at equilibrium with the rock as will the brine in the reservoir below. It is only in the mixing region between the two fluids that disequilibrium can occur [72]. Here, the reaction will create regions of higher porosity where the denser CO_2-brine solution will move, and the subsequent density differential will be greater and so promote convection.

Most importantly, it was proposed that these wormholes can enhance the fingering phenomena when the reaction is coupled with the buoyant convective flow in a fluid-saturated medium [105]. In a specific case study on the Songliao Basin of China, the vertical convective currents were found to be strengthened when vertical permeability was increased [107]; suggesting that when coupled the two processes can feed each other. Numerically, the formation of slender fingers with high amplitude has also been reported [108] that can be associated with 'chimneys' of enhanced porosity created along the vertical axis of the system. Interestingly, these have been proposed as a result of a change in the direction of convection currents observed due to secondary instabilities that arise from a variation of the equilibrium solubility.

At low Rayleigh numbers below even the critical Ra, the range in which many of reservoirs sit, the effect of the reaction–permeability feedback is shown to be destabilising whereas, at higher Rayleigh numbers, the precipitation and dissolution are stabilising [109]. As a result, many more reservoirs could be potential sites if reaction is taking into consideration.

8.3 Final Remarks

The future work described here has been largely application-driven, but it is, of course, vital theoretical work continues to expand our fundamental understanding of the convective process. The work presented in the thesis is by no means comprehensive, and there are many unresolved questions on this topic, but we hope that this work provides a foundation on which new exciting work will build.

Appendix A

A1 Permission to Reproduce

ELSEVIER LICENSE
TERMS AND CONDITIONS

Dec 26, 2018

This Agreement between imperial collge london -- rebecca LIYANAGE ("You") and Elsevier ("Elsevier") consists of your license details and the terms and conditions provided by Elsevier and Copyright Clearance Center.

License Number	4496351485245
License date	Dec 26, 2018
Licensed Content Publisher	Elsevier
Licensed Content Publication	International Journal of Greenhouse Gas Control
Licensed Content Title	Convective dissolution of CO2 in saline aquifers: Progress in modeling and experiments
Licensed Content Author	Hamid Emami-Meybodi,Hassan Hassanzadeh,Christopher P. Green,Jonathan Ennis-King
Licensed Content Date	Sep 1, 2015
Licensed Content Volume	40
Licensed Content Issue	n/a
Licensed Content Pages	29
Start Page	238
End Page	266
Type of Use	reuse in a thesis/dissertation
Portion	figures/tables/illustrations
Number of figures/tables/illustrations	1
Format	both print and electronic
Are you the author of this Elsevier article?	No
Will you be translating?	No
Original figure numbers	figure 1
Title of your thesis/dissertation	Convective Dissolution in Porous Media: Three-Dimensional Imaging Experiments and Numerical Simulations
Expected completion date	Jan 2019
Estimated size (number of pages)	190
Requestor Location	imperial college london exhibition Road london, sw71az United Kingdom Attn: imperial collge london
Publisher Tax ID	GB 494 6272 12
Total	0.00 GBP
Terms and Conditions	

A2 X-ray Imaging of Aqueous MEG and BEG Solutions and Density Curves

In this study, potassium iodide (KI) was used as dopant in the MEG solution (∼9wt.%) to enable precise imaging of the solute plume. In the derivation of the operating equation used to compute the solute concentration from the X-ray tomograms (Section 2.2) it was assumed that the CT number varies linearly with the weight fraction of KI in solution. This assumption is verified against independent measurements of the measured CT number of solutions of MEG (10wt.% KI) mixed with water, as shown in Figure A1. The following imaging parameters were applied: field-of-view (24×24) cm^2; energy level of radiation 120 eV; tube current 150 mA.

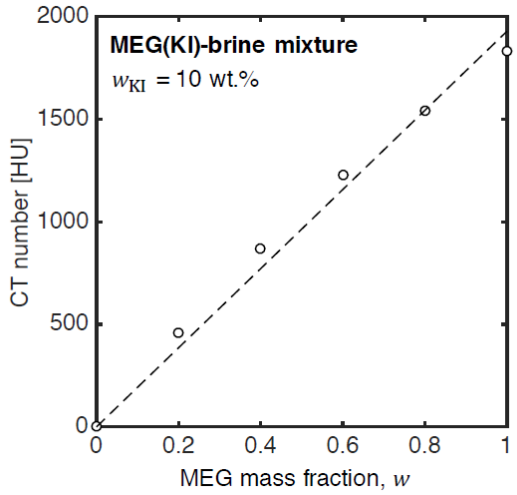

Figure A1: CT number as a function of the mass fraction of MEG in water. The MEG solution contains 10wt.% KI that is used as dopant in the experiments of convective mixing. The dashed line is a linear fit to the experimental values ($R^2 = 0.996$).

Throughout the experiment, the CT readings are converted into mass fraction of MEG or BEG in solution using Eq. 2.4. The density in each voxel is then computed from the parameterisation of the curves shown in Figure 2.2 as a function of the average mass fraction of the solute. The curves have been fitted using polynomials of the form, $\rho = a_0 + a_1 w + a_2 w^2 + a_3 w^3$, with parameters given in Table A1.

Table A1: Parameters of the fitted density curves shown in Figure 2.2 with functional form, $\rho = a_0 + a_1 w + a_2 w^2 + a_3 w^3$.

Solution	a_0	a_1	a_2	a_3
MEG55/brine	1.04	0.0131	0.0151	-0.0503
MEG57/brine	1.04	0.0179	0.0136	-0.0466
MEG59/brine	1.04	0.0306	-0.0086	-0.0300
BEG65/brine	1.06	0.0160	0.0402	-0.0763

A3 Linear Regression for a Straight Line Fit

A linear regime is observed in the MEG fraction curves when plotted as a function of the square root of time(Chapter 3,4,6). The general equation for a linear fit is $y = \mathrm{A}x + \mathrm{B}$ where gradient is used to calculate an effective diffusion coefficient, the x axis intercept is the shutdown time and the onset time can be estimated when $y = 1$.

The variance in the measurements is defined as σ_{M} [g] and the coefficients A and B and the associated uncertainties can be calculated through linear regression[83] using a weighting factor $w = 1/{\sigma_{\mathrm{M}}}^2$. It is assumed that uncertainty is associated only to the y variable (in this case, mass) and the uncertainty in the x (in this case, time) is negligible, therefore:

$$A = \frac{\sum wx^2 \sum wy - \sum wx \sum wxy}{\Delta} \tag{A-1}$$

$$B = \frac{\sum w \sum wxy - \sum wx \sum wy}{\Delta} \tag{A-2}$$

where

$$\Delta = \sum w \sum wx^2 - (\sum wx)^2 \tag{A-3}$$

and the uncertainties in A and B are:

$$\sigma_{\mathrm{A}} = \sqrt{\frac{\sum wx^2}{\Delta}} \tag{A-4}$$

$$\sigma_{\mathrm{B}} = \sqrt{\frac{\sum w}{\Delta}} \tag{A-5}$$

A4 Modified logistic function

A modified logistic function was used to to describe the temporal evolution of the dissolved mass, $m_j(t)$, in the bottom ($j = B$) and top ($j = T$) sections of the bowl. In particular, the logistic function has been modified so as to attain the correct limiting behaviour at early times, i.e.

$$\text{For } t \to 0 : \frac{m_B(t)}{M_1} = Kt^* \tag{A-6}$$

where $t* = \sqrt{t}$ and K is the slope of the straight line obtained from the numerical solution of the diffusion equation (see Section 2.4) when plotted as $m_B(t)/M_1$ vs. $\sqrt{t}$. In this study, $K = 0.0096$ min$^{-0.5}$. The modified logistic function reads therefore as follows:

$$\frac{m_B(t)}{M_1} = Kt^* + \frac{D - Kt^*}{\left[C + a_1 e^{(-a_2(t^* - a_4))}\right]^{1/a_3}} \tag{A-7}$$

where a_1, a_2, a_3, a_4 and C_1 and C_2 are fitting parameters obtained by matching Eq. A-7 to the experimental data and $m_T(t) = 1 - m_B(t)$. The values of the obtained parameters are summarised in Table A2.

Table A2: Parameters of the logistic function, Eq. A-7, fitted to measured relative amount of dissolved mass as a function of the square root of time. The experimental data are shown in Figure 3.1 together with the corresponding fitted curves.

	Solution	C_1	C_2	a_1	a_2	a_3	a_4
Chapter 3	MEG55/brine	1	1	1.4341	0.5617	1.4345	14.22
		1	1	1.3972	0.4683	1.2949	15.15
	MEG57/brine	1	1	0.0461	0.5242	1.4778	19.33
		1	1	1.3960	0.4915	1.5600	12.43
	MEG59/brine	1	1	1.1921	0.4984	1.0271	8.969
	BEG65 - 1	1	1	1.7093	0.3589	0.7965	12.689
	BEG65 - 2	1	1	1.8047	0.3333	0.7109	11.004
Ch. 4	Cube	1	1	1.8865	0.4369	1.5867	13.007
	Cylinder	1	1	1.9759	0.4013	1.1788	11.736
Chapter 5	Exp 1a*	4	2.6	1.3791	0.6703	1.1024	7.338
	Exp 1b*	4	2.6	1.4269	0.6952	1.1401	6.893
	Exp 2a*	2	2	1.7186	0.8334	0.7775	4.173
	Exp 2b*	2	2	2.1105	0.7464	0.8232	6.370
	Exp 3a	1	1	1.5827	0.5590	0.6098	3.824
	Exp 3b	1	1	2.5589	0.5235	0.3661	1.187
	Exp 4	1	1	1.4769	0.3341	0.4798	7.032
	Exp 5	1	1	1.3494	0.4006	0.4963	6.302
	Exp 6*	6	4	1.3952	0.5642	0.9960	11.842
	Exp 7*	6	4	1.5111	0.6034	1.0443	10.840
Chapter 6	2 layers $k/k_L = 4$	1	1	2.5374	0.2921	0.6636	9.169
	2 layers $k/k_L = 25$	1	1	1.4064	0.4072	0.8642	9.600
	'Patchy'	1	1	1.2559	0.4789	1.1673	10.841
	'Random'	1	1	1.9662	0.3991	1.1209	12.1964

Bibliography

[1] B. Gebhart and L. Pera, "The nature of vertical natural convection flows resulting from the combined buoyancy effects of thermal and mass diffusion," *International Journal of Heat and Mass Transfer*, vol. 14, no. 12, pp. 2025–2050, 1971.

[2] H.-J. Diersch and O. Kolditz, "Variable-density flow and transport in porous media: approaches and challenges," *Advances in Water Resources*, vol. 25, no. 8, pp. 899 – 944, 2002.

[3] D. Sharp, "An overview of rayleigh-taylor instability," *Physica D: Nonlinear Phenomena*, vol. 12, no. 1, pp. 3 – 18, 1984.

[4] E. R. Lapwood, "Convection of a fluid in a porous medium," *Mathematical Proceedings of the Cambridge Philosophical Society*, vol. 44, no. 4, p. 508–521, 1948.

[5] J. Otero, L. Dontcheva, H. Johnston, R. Worthing, A. Kurganov, G. Petrova, and C. R. Doering, "High-rayleigh-number convection in a fluid-saturated porous layer," *Journal of Fluid Mechanics*, vol. 500, p. 263–281, 2004.

[6] D. R. Hewitt, J. a. Neufeld, and J. R. Lister, "Ultimate regime of high Rayleigh number convection in a porous medium," *Physical Review Letters*, vol. 108, no. 22, pp. 551–586, 2012.

[7] A. Riaz, M. Hesse, H. A. Tchelepi, and F. M. Orr, "Onset of convection in a gravitationally unstable diffusive boundary layer in porous media," *Journal of Fluid Mechanics*, vol. 548, pp. 87–111, 2006.

[8] A. C. Slim, "Solutal-convection regimes in a two-dimensional porous medium," *Journal of Fluid Mechanics*, vol. 741, pp. 461–491, 2014.

[9] M. L. Szulczewski, M. a. Hesse, and R. Juanes, "Carbon dioxide dissolution in structural and stratigraphic traps," *Journal of Fluid Mechanics*, vol. 736, pp. 287–315, 2013.

[10] H. E. Huppert and J. a. Neufeld, "The Fluid Mechanics of Carbon Dioxide Sequestration," *Annual Review of Fluid Mechanics*, vol. 46, no. 1, pp. 255–272, 2014.

[11] H. Emami-Meybodi, H. Hassanzadeh, C. P. Green, and J. Ennis-King, "Convective dissolution of CO_2 in saline aquifers: Progress in modeling and experiments," *International Journal of Greenhouse Gas Control*, 2015.

[12] E. Lindeberg and D. Wessel-Berg, "Vertical convection in an aquifer column under a gas cap of CO_2," *Energy Conversion and Management*, vol. 38, pp. S229–S234, 1997.

[13] E. C. Efika, R. Hoballah, X. Li, E. F. May, M. Nania, Y. Sanchez-Vicente, and J. M. Trusler, "Saturated phase densities of (co_2+h_2o) at temperatures from (293 to 450)k and pressures up to 64mpa," *The Journal of Chemical Thermodynamics*, vol. 93, pp. 347 – 359, 2016.

[14] S. M. Benson and F. M. Orr, "Carbon dioxide capture and storage," *MRS Bulletin*, vol. 33, no. 4, p. 303–305, 2008.

[15] J. Ennis-King, I. Preston, and L. Paterson, "Onset of convection in anisotropic porous media subject to a rapid change in boundary conditions," *Physics of Fluids*, no. 8, 2005.

[16] K. J. Sathaye, M. A. Hesse, M. Cassidy, and D. F. Stockli, "Constraints on the magnitude and rate of co_2 dissolution at bravo dome natural gas field," *Proc Natl Acad Sci U S A*, vol. 111, 2014.

[17] M. L. Szulczewski, C. W. MacMinn, H. J. Herzog, and R. Juanes, "Lifetime of carbon capture and storage as a climate-change mitigation technology," *Proceedings of the National Academy of Sciences*, vol. 109, no. 14, pp. 5185–5189, 2012.

[18] H. Emami-Meybodi and H. Hassanzadeh, "Mixing induced by buoyancy-driven flows in porous media," *AlChE J.*, vol. 59, pp. 1378–1389, 2013.

[19] T. J. Kneafsey and K. Pruess, "Laboratory flow experiments for visualizing carbon dioxide-induced, density-driven brine convection," *Transport in Porous Media*, vol. 82, no. 1, pp. 123–139, 2010.

[20] Y. Xie, C. T. Simmons, A. D. Werner, and H.-J. G. Diersch, "Prediction and uncertainty of free convection phenomena in porous media," *Water Resources Research*, vol. 48, no. 2, 2012.

[21] J. A. Neufeld, M. A. Hesse, A. Riaz, M. A. Hallworth, H. A. Tchelepi, and H. E. Huppert, "Convective dissolution of carbon dioxide in saline aquifers," *Geophysical Research Letters*, vol. 37, no. 22, 2010.

[22] B. Meulenbroek, R. Farajzadeh, and H. Bruining, "The effect of interface movement and viscosity variation on the stability of a diffusive interface between aqueous and gaseous CO_2," *Physics of Fluids*, vol. 25, no. 7, 2013.

[23] M. T. Elenius, J. M. Nordbotten, and H. Kalisch, "Convective mixing influenced by the capillary transition zone," *Computational Geosciences*, vol. 18, pp. 417–431, Aug 2014.

[24] H. Emami-Meybodi, "Stability analysis of dissolution-driven convection in porous media," *Physics of Fluids*, vol. 29, no. 1, p. 014102, 2017.

[25] H. Hassanzadeh, M. Pooladi-Darvish, and D. W. Keith, "Scaling behavior of convective mixing, with application to geological storage of co_2," *AIChE Journal*, vol. 53, pp. 1121–1131, 5 2007.

[26] T. Ahmed, H. Nasrabadi, and A. Firoozabadi, "Complex flow and composition path in co_2 injection schemes from density effects," *Energy & Fuels*, vol. 26, no. 7, pp. 4590–4598, 2012.

[27] J. Both, S. Gasda, I. Aavatsmark, and R. Kaufmann, "Gravity-driven convective mixing of co_2 in oil," *Conference: The Third Sustainable Earth Sciences*, 10 2015.

[28] M. C. K. Kim, "Onset of buoyancy-driven convection in a variable viscosity liquid saturated in a porous medium," *Chemical Engineering Science*, vol. 113, pp. 77 – 87, 2014.

[29] R. M. Lansangan and J. L. Smith, "Density, and composition measurements of co_2/west texas oil systems," *Society of Petroleum Engineers*, vol. 8, no. 3, pp. 175–182, 1993.

[30] G. S. H. Pau, J. B. Bell, K. Pruess, A. S. Almgren, M. J. Lijewski, and K. Zhang, "High-resolution simulation and characterization of density-driven flow in CO_2 storage in saline aquifers," *Advances in Water Resources*, vol. 33, no. 4, pp. 443–455, 2010.

[31] S. Backhaus, K. Turitsyn, and R. E. Ecke, "Convective instability and mass transport of diffusion layers in a Hele-Shaw geometry," *Physical Review Letters*, vol. 106, no. 10, pp. 1–4, 2011.

[32] H. Hassanzadeh, M. Pooladi-Darvish, and D. W. Keith, "Modelling of convective mixing in CO_2 storage," *Journal of Canadian Petroleum Technology*, vol. 44, no. 10, pp. 43–50, 2005.

[33] N. Tilton, "Onset of transient natural convection in porous media due to porosity perturbations," *Journal of Fluid Mechanics*, vol. 838, p. 129–147, 2018.

[34] S. M. Jafari Raad and H. Hassanzadeh, "Onset of dissolution-driven instabilities in fluids with nonmonotonic density profile," *Phys. Rev. E*, vol. 92, p. 053023, Nov 2015.

[35] A. C. Slim and T. S. Ramakrishnan, "Onset and cessation of time-dependent, dissolution-driven convection in porous media," *Physics of Fluids*, vol. 22, no. 12, 2010.

[36] L. Howard, "Convection at high rayleigh number," *Int'l Congr. Applied Meehan*, vol. 11, pp. 1109–1115, 1964. cited By 1.

[37] P. Tsai, H. Riesing, and H. Stone, "Density-driven convection enhanced by an inclined boundary: implications for geological co_2 storage," *Phys. Rev. E*, vol. 87, p. 011003, 2013.

[38] J.-H. Ching, P. Chen, and P. A. Tsai, "Convective mixing in homogeneous porous media flow," *Phys. Rev. Fluids*, vol. 2, p. 014102, Jan 2017.

[39] Y. Nakanishi, A. Hyodo, L. Wang, and T. Suekane, "Experimental study of 3d rayleigh–taylor convection between miscible fluids in a porous medium," *Advances in Water Resources*, vol. 97, pp. 224 – 232, 2016.

[40] S. M. Jafari Raad, H. Emami-Meybodi, and H. Hassanzadeh, "On the choice of analogue fluids in co_2 convective dissolution experiments," *Water Resources Research*, vol. 52, no. 6, pp. 4458–4468, 2016.

[41] C. Yang and Y. Gu, "Accelerated mass transfer of CO_2 in reservoir brine due to density-driven natural convection at high pressures and elevated temperatures," *Industrial and Engineering Chemistry Research*, vol. 45, pp. 2430–2436, 2006.

[42] R. Farajzadeh, P. L. J. Zitha, and J. Bruining, "Enhanced mass transfer of co_2 into water: Experiment and modeling," *Industrial & Engineering Chemistry Research*, vol. 48, no. 13, pp. 6423–6431, 2009.

[43] R. Khosrokhavar, G. Elsinga, R. Farajzadeh, and H. Bruiningr, "Visualization and investigation of natural convection flow of co_2 in aqueous and oleic systems," *Journal of Petroleum Science and Engineering*, 2014.

[44] B. Arendt, D. Dittmar, and R. Eggers, "Interaction of interfacial convection and mass transfer effects in the system co_2–water," *International Journal of Heat and Mass Transfer*, vol. 47, no. 17, pp. 3649 – 3657, 2004.

[45] D. L. Newell, J. W. Carey, S. N. Backhaus, and P. Lichtner, "Experimental study of gravitational mixing of supercritical co_2," *International Journal of Greenhouse Gas Control*, vol. 71, pp. 62 – 73, 2018.

[46] Nazari-Moghaddam, Rasoul, Rostami, Behzad, Pourafshary, Peyman, and Y. Fallahzadeh, "Quantification of density-driven natural convection for dissolution mechanism in co_2 sequestration," *Transport in Porous Media*, vol. 92, pp. 439–456, 2011.

[47] Nazari-Moghaddam, Rasoul, Rostami, Behzad, Pourafshary, and Peyman, "Scaling analysis of the convective mixing in porous media for geological storage of co_2: An experimental approach," *Chemical Engineering Communications*, vol. 202, pp. 815–822, 2015.

[48] C. T. S Bories, "Échanges thermiques et tourbillons dans une couche poreuse horizontale," *La Houille Blanche*, vol. 3, pp. 237–245, 1969.

[49] C. R. B. Lister, "An explanation for the multivalued heat transport found experimentally for convection in a porous medium," *Journal of Fluid Mechanics*, vol. 214, pp. 287–320, 1990.

[50] L. Howle, R. P. Behringer, and J. Georgiadis, "Visualization of convective fluid flow in a porous medium," *Nature*, vol. 362, pp. 230–232, 1993.

[51] L. E. Howle, "Active control of rayleigh–bénard convection," *Physics of Fluids*, vol. 9, no. 7, pp. 1861–1863, 1997.

[52] M. D. Shattuck and J. G. R. P. Behringer, G. A. Johnson, "Onset and stability of convection in porous media: Visualization by magnetic resonance imaging," *Physical Reveiw Letters.*, vol. 75, pp. 1934 – 1937, 1995.

[53] C. W. MacMinn and R. Juanes, "Buoyant currents arrested by convective dissolution," *Geophysical Research Letters*, vol. 40, no. 10, pp. 2017–2022, 2013.

[54] E. Agartan, L. Trevisan, A. C. J., B. Q. Zhou, and T. Illangasekare, "Experimental study on effects of geologic heterogeneity in enhancing dissolution trapping of supercritical co_2," *Water Resour. Res*, vol. 51, 2015.

[55] C. Thomas, L. Lemaigre, A. Zalts, A. D'Onofrio, and A. D. Wit, "Experimental study of co_2 convective dissolution: The effect of color indicators," *International Journal of Greenhouse Gas Control*, vol. 42, pp. 525 – 533, 2015.

[56] A. C. Slim, M. M. Bandi, J. C. Miller, and L. Mahadevan, "Dissolution-driven convection in a hele–shaw cell," *Physics of Fluids*, vol. 25, 2013.

[57] R. E. Ecke and S. Backhaus, "Plume dynamics in hele-shaw porous media convection," *Philosophical Transactions of the Royal Society of London A: Mathematical, Physical and Engineering Sciences*, vol. 374, no. 2078, 2016.

[58] J. J. Hidalgo, J. Fe, L. Cueto-Felgueroso, and R. Juanes, "Scaling of convective mixing in porous media," *Phys. Rev. Lett.*, vol. 109, p. 264503, Dec 2012.

[59] V. Loodts, P. M. J. Trevelyan, L. Rongy, and A. De Wit, "Density profiles around $a+b \rightarrow c$ reaction-diffusion fronts in partially miscible systems: A general classification," *Phys. Rev. E*, vol. 94, p. 043115, Oct 2016.

[60] C. P. Green and J. Ennis-King, "Steady dissolution rate due to convective mixing in anisotropic porous media," *Advances in Water Resources*, vol. 73, pp. 65 – 73, 2014.

[61] S. Khataniar and E. J. Peters, "The effect of reservoir heterogeneity on the performance of unstable displacements," *Journal of Petroleum Science and Engineering*, vol. 7, no. 3, pp. 263 – 281, 1992.

[62] P. Cheng, M. Bestehorn, and A. Firoozabadi, "Effect of permeability anisotropy on buoyancy-driven flow for co_2 sequestration in saline aquifers," *Water Resources Research*, vol. 48, no. 9, 2012.

[63] R. Farajzadeh, P. Ranganathan, P. L. J. Zitha, and J. Bruining, "The effect of heterogeneity on the character of density-driven natural convection of CO_2 overlying a brine layer," *Advances in Water Resources*, vol. 34, no. 3, pp. 327–339, 2011.

[64] C. A. Aggelopoulos and C. D. Tsakiroglou, "Effects of micro-heterogeneity and hydrodynamic dispersion on the dissolution rate of carbon dioxide in water-saturated porous media," *International Journal of Greenhouse Gas Control*, vol. 10, pp. 341 – 350, 2012.

[65] P. Ranganathan, R. Farajzadeh, H. Bruining, and P. L. J. Zitha, "Numerical simulation of natural convection in heterogeneous porous media for co_2 geological storage," *Transport in Porous Media*, vol. 95, pp. 25–54, Oct 2012.

[66] X.-Z. Kong and M. O. Saar, "Numerical study of the effects of permeability heterogeneity on density-driven convective mixing during co_2 dissolution storage," *International Journal of Greenhouse Gas Control*, vol. 19, pp. 160 – 173, 2013.

[67] M. T. Elenius and S. E. Gasda, "Convective mixing in formations with horizontal barriers," *Advances in Water Resources*, vol. 62, pp. 499 – 510, 2013. Computational Methods in Geologic CO_2 Sequestration.

[68] A. Taheri, O. Torsæter, E. Lindeberg, N. Hadia, and D. Wessel-Berg, "Qualitative and quantitative experimental study of convective mixing process during storage

of co_2 in heterogeneous saline aquifers," *International Journal of Greenhouse Gas Control*, vol. 71, 03 2018.

[69] V. E. Post and C. Simmons, "Free convective controls on sequestration of salts into low-permeability strata: Insights from sand tank laboratory experiments and numerical modelling," *Hydrogeology Journal*, vol. 18, no. 1, pp. 39–54, 2010.

[70] E. Agartan, A. Cihan, T. H. Illangasekare, Q. Zhou, and J. T. Birkholzer, "Mixing and trapping of dissolved co_2 in deep geologic formations with shale layers," *Advances in Water Resources*, vol. 105, pp. 67 – 81, 2017.

[71] X. Fu, L. Cueto-Felgueroso, and R. Juanes, "Pattern formation and coarsening dynamics in three-dimensional convective mixing in porous media," *Philos Trans A Math Phys Eng Sci*, vol. 371, p. 20120355, 2013.

[72] X. Fu, L. Cueto-Felgueroso, D. Bolster, and R. Juanes, "Rock dissolution patterns and geochemical shutdown of CO_2 –brine–carbonate reactions during convective mixing in porous media," *Journal of Fluid Mechanics*, vol. 764, p. 296–315, 2015.

[73] M. R. Soltanian, M. A. Amooie, N. Gershenzon, Z. Dai, R. Ritzi, F. Xiong, D. Cole, and J. Moortgat, "Dissolution trapping of carbon dioxide in heterogeneous aquifers," *Environmental Science & Technology*, vol. 51, no. 13, pp. 7732–7741, 2017. PMID: 28598155.

[74] D. Hewitt, J. Neufeld, and J. Lister, "High rayleigh number convection in a three-dimensional porous medium," *Journal of Fluid Mech*, vol. 743, pp. 879–895, 2014.

[75] B. Knorr, Y. Xie, C. Stumpp, P. Maloszewski, and C. T. Simmons, "Representativeness of 2d models to simulate 3d unstable variable density flow in porous media," *Journal of Hydrology*, vol. 542, pp. 541 – 551, 2016.

[76] L. Wang, Y. nakanishi, A. Hyodo, and T. Suekane, "Three-dimensional structure of natural convection in a porous medium: Effect of dispersion on finger structure," *International Journal of Greenhouse Gas Control*, vol. 53, pp. 274–283, 2016.

[77] J. J. Hidalgo and J. Carrera, "Effect of dispersion on the onset of convection during co_2 sequestration," *Journal of Fluid Mechanics*, vol. 640, p. 441–452, 2009.

[78] G. Ternström, A. Sjöstrand, G. Aly, and . Jernqvist, "Mutual diffusion coefficients of water + ethylene glycol and water + glycerol mixtures," *Journal of Chemical & Engineering Data*, vol. 41, no. 4, pp. 876–879, 1996.

[79] R. Pini, S. Krevor, and S. Benson, "Capillary pressure and heterogeneity for the co_2/water system in sandstone rocks at reservoir conditions," *Advances in Water Resources*, vol. 38, pp. 48–59, 2012.

[80] V. Clausnitzer and J. Hopmans, "Determination of phase-volume fractions from tomographic measurements in two-phase systems," *Advances in Water Resources*, vol. 22, no. 6, pp. 577 – 584, 1999.

[81] and, "The penetration of a fluid into a porous medium or hele-shaw cell containing a more viscous liquid," *Proceedings of the Royal Society of London A: Mathematical, Physical and Engineering Sciences*, vol. 245, no. 1242, pp. 312–329, 1958.

[82] I. Bihi, M. Baudoin, J. E. Butler, C. Faille, and F. Zoueshtiagh, "Inverse saffman-taylor experiments with particles lead to capillarity driven fingering instabilities," *Phys. Rev. Lett.*, vol. 117, p. 034501, Jul 2016.

[83] J. Taylor, "An introduction to error analysis: The study of uncertainty in physical measurements," *University Science Book*, vol. 2nd edn., 1997.

[84] S. Chevalier, T. F. Faisal, Y. Bernabe, R. Juanes, and M. Sassi, "Numerical sensitivity analysis of density driven co2 convection with respect to different modeling and boundary conditions," *Heat and Mass Transfer*, vol. 51, no. 7, pp. 941–952, 2015.

[85] N. D.A and B. A., eds., *Convection in Porous Media*. Springer, 2006.

[86] Y. Katto and T. Masuoka, "Criterion for the onset of convective flow in a fluid in a porous medium," *International Journal of Heat and Mass Transfer*, vol. 10, no. 3, pp. 297 – 309, 1967.

[87] D. Chemical, "Propylene glycols - density values." https://dow-answer.custhelp.com/app/answers/detail/a_d/7471, 2017.

[88] D. R. Hewitt, J. A. Neufeld, and J. R. Lister, "Stability of columnar convection in a porous medium," *Journal of Fluid Mechanics*, vol. 737, p. 205–231, 2013.

[89] Statios, "Variogram calculation and interpretation." http://www.statios.com/resources/04-variogram.pdf, 2000.

[90] M. Bickle, A. Chadwick, H. E. Huppert, M. Hallworth, and S. Lyle, "Modelling carbon dioxide accumulation at sleipner: Implications for underground carbon storage," *Earth and Planetary Science Letters*, vol. 255, no. 1, pp. 164 – 176, 2007.

[91] F. C. Boait, N. J. White, M. J. Bickle, R. A. Chadwick, J. A. Neufeld, and H. E. Huppert, "Spatial and temporal evolution of injected co2 at the sleipner field, north sea," *Journal of Geophysical Research: Solid Earth*, vol. 117, 2012.

[92] C. P. Green and J. Ennis-King, "Effect of vertical heterogeneity on long-term migration of co_2 in saline formations," *Transport in Porous Media*, vol. 82, pp. 31–47, Mar 2010.

[93] R. P. Dias, J. A. Teixeira, M. G. Mota, and A. I. Yelshin, "Particulate binary mixtures dependence of packing porosity on particle size ratio," *Industrial & Engineering Chemistry Research*, vol. 43, no. 24, pp. 7912–7919, 2004.

[94] M. T. Elenius and K. Johannsen, "On the time scales of nonlinear instability in miscible displacement porous media flow," *Computational Geosciences*, vol. 16, no. 4, pp. 901–911, 2012.

[95] P. K. Kitanidis, "The concept of the dilution index," *Water Resources Research*, vol. 30, no. 7, pp. 2011–2026, 1994.

[96] M. A. Budroni, L. A. Riolfo, L. Lemaigre, F. Rossi, M. Rustici, and A. De Wit, "Chemical control of hydrodynamic instabilities in partially miscible two-layer systems," *The Journal of Physical Chemistry Letters*, vol. 5, no. 5, pp. 875–881, 2014.

[97] C. Thomas, S. Dehaeck, and A. D. Wit, "Convective dissolution of co2 in water and salt solutions," *International Journal of Greenhouse Gas Control*, vol. 72, pp. 105 – 116, 2018.

[98] C. Peng, J. P. Crawshaw, G. C. Maitland, and J. M. Trusler, "Kinetics of calcite dissolution in co_2-saturated water at temperatures between (323 and 373)k and pressures up to 13.8mpa," *Chemical Geology*, vol. 403, pp. 74 – 85, 2015.

[99] M. McBride-Wright, G. C. Maitland, and J. P. M. Trusler, "Viscosity and density of aqueous solutions of carbon dioxide at temperatures from (274 to 449) k and at pressures up to 100 mpa," *Journal of Chemical & Engineering Data*, vol. 60, no. 1, pp. 171–180, 2015.

[100] S. P. Cadogan, J. P. Hallett, G. C. Maitland, and J. P. M. Trusler, "Diffusion coefficients of carbon dioxide in brines measured using 13c pulsed-field gradient nuclear magnetic resonance," *Journal of Chemical & Engineering Data*, vol. 60, no. 1, pp. 181–184, 2015.

[101] B. Dubacq, M. J. Bickle, and K. A. Evans, "An activity model for phase equilibria in the h_2o–co_2–nacl system," *Geochimica et Cosmochimica Acta*, vol. 110, pp. 229 – 252, 2013.

[102] K. Ghesmat, H. Hassanzadeh, and J. Abedi, "The impact of geochemistry on convective mixing in a gravitationally unstable diffusive boundary layer in porous media: Co_2 storage in saline aquifers," *Journal of Fluid Mechanics*, vol. 673, p. 480–512, 2011.

[103] J. T. H. Andres and S. S. S. Cardoso, "Onset of convection in a porous medium in the presence of chemical reaction," *Physical Review E - Statistical, Nonlinear, and Soft Matter Physics*, vol. 83, no. 4, 2011.

[104] J. T. H. Andres and S. S. S. Cardoso, "Convection and reaction in a diffusive boundary layer in a porous medium: Nonlinear dynamics," *AIP: Chaos*, vol. 22, no. 3, 2012.

[105] C. Zhao, B. E. Hobbs, A. Ord, P. Hornby, and S. Peng, "Morphological evolution of three-dimensional chemical dissolution front in fluid-saturated porous media: a numerical simulation approach," *Geofluids*, vol. 8, no. 2, pp. 113–127, 2008.

[106] J. Ennis-King and L. Paterson, "Coupling of geochemical reactions and convective mixing in the long-term geological storage of carbon dioxide," *International Journal of Greenhouse Gas Control*, vol. 1, no. 1, pp. 86–93, 2007.

[107] W. Zhang, Y. Li, and A. N. Omambia, "Reactive transport modeling of effects of convective mixing on long-term CO_2 geological storage in deep saline formations," *International Journal of Greenhouse Gas Control*, vol. 5, no. 2, pp. 241–256, 2011.

[108] T. J. Ward, K. A. Cliffe, O. E. Jensen, and H. Power, "Dissolution-driven porous-medium convection in the presence of chemical reaction," *Journal of Fluid Mechanics*, vol. 747, p. 316–349, 2014.

[109] L. T. Ritchie and D. Pritchard, "Natural convection and the evolution of a reactive porous medium," *Journal of Fluid Mechanics*, vol. 673, p. 286–317, 2011.